Studies in Thin Film Flows

A thesis submitted to the University of Strathclyde
for the degree of Doctor of Philosophy
in the Faculty of Science

by

Iain Stewart McKinley
Department of Mathematics
University of Strathclyde
Glasgow
1999

Contents

List of Figures

List of Tables

Acknowledgements

Over the past four years there have been many people who have helped to make this thesis a reality.

In particular, I would like to thank my supervisor, Dr Stephen Wilson, whose boundless energy and enthusiasm helped to keep my motivation and my spirits high. I would also like to thank Dr Brian Duffy for his insightful comments on much of this work, and Prof. David Sloan for acting as my supervisor while Steve was on sabbatical leave during my third year.

Thanks to the University of Strathclyde for giving me the chance to be a Teaching Assistant and for letting me loose with lectures and tutorials that I thoroughly enjoyed.

Thanks also to all the Postgrads for a million laughs and memories, to my parents for their endless support and understanding, and to Claire for going through it all with me.

Abstract

Using the lubrication approximation to the Navier-Stokes equations we investigate the evolution and stability of a thin film of incompressible Newtonian fluid on a planar substrate subjected to a jet of air blowing normally to the substrate. For the simple model of the air jet we adopt, the initially axisymmetric problems we study are identical to those of a drop spreading on a turntable rotating at constant angular velocity (the simplest model for spin coating). We consider both drops without a dry patch (referred to as "non-annular") and drops with a dry patch at their centre (referred to as "annular"). First, both symmetric two-dimensional and axisymmetric three-dimensional drops are considered in the quasi-static limit of small capillary number. The evolution of both non-annular and annular drops and the stability of equilibrium solutions to small perturbations with zero wavenumber are determined. Using a specially developed finite-difference code we then investigate the linear stability of both an initially two-dimensional thin ridge of fluid and an initially axisymmetric thin drop of fluid to perturbations with non-zero wavenumber for the general case of non-quasi-static motion (non-zero capillary number). For the ridge we examine the cases when the jet acts at the centre of the ridge and when the jet acts off-centre. For the drop we examine both non-annular and annular drops. For each problem we examine both the special case of quasi-static motion analytically and the general case of non-zero capillary number numerically.

Chapter 1

Introduction

1.1 Background

Thin fluid films arise in many physical settings. For example, in geology they can appear as underwater gravity currents or as lava flows, while in biophysics they can appear as membranes, linings of mammalian lungs or as tear films in the eye. In engineering, thin-film coating arises in the manufacture of a vast number of different products, including paper of various surface textures, printed matter such as books, newspapers and magazines, magnetic storage media such as audio tapes, video tapes and computer discs, fibres and wires, photoresist coatings for the manufacture of microelectronics such as printed circuits and solar cells, medical products such as transdermic systems which release active substances into the skin from a thin patch, sand paper, adhesive tapes and many others. The importance of thin fluid films in these and many other physical situations has motivated considerable theoretical and experimental work on the spreading of a thin fluid film on a solid substrate (see, for example, the recent review articles by Oron, Davis & Bankoff [45] and Myers [44]). Much of this work involves examining the spreading of a fluid subject to an external force. Examples of such forces include gravitational, electrostatic, magnetic and centrifugal forces as well as a non-uniform pressure loading caused by a fluid overlying the thin film. In this thesis we shall consider two problems of this type, namely a thin drop of fluid on a uniformly rotating substrate (the simplest model for spin coating)

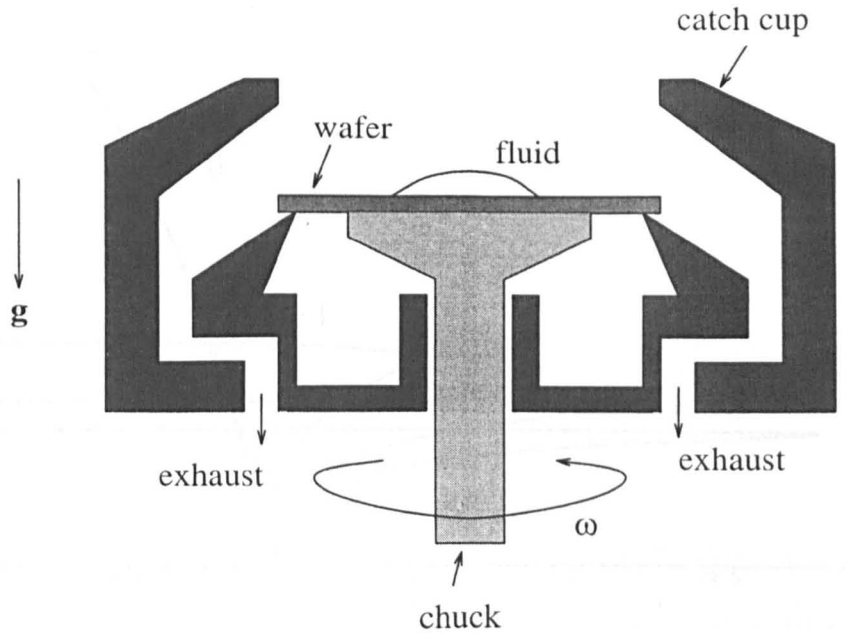

Figure 1.1: Schematic diagram of a typical spin-coating system.

or under the influence of a jet of air directed normally towards a stationary substrate.

Spin coating is a widely used industrial process in which a fluid film is spread by centrifugal force onto a rotating substrate. Its history dates back to the 1950s when it was used to deposit phosphor onto the curved glass surfaces of colour television tubes. Today, spin coating is used in the microelectronics industry as a means of depositing polymer resist layers for photolithographic processing of integrated circuits (photolithography is a process used in the manufacture of semiconductor devices and printed circuits in which a particular pattern is transferred from a photograph onto a substrate). Another important modern application of spin coating is the deposition of transparent or reflective inorganic colloidal surface coatings on laser optical components, such as highly reflecting mirrors. A typical spin-coating system is shown in Fig. 1.1. The fluid spreads over the wafer which rotates with angular velocity ω. The catch cup traps droplets that are flung from the wafer, preventing their unwanted release into the environment. An exhaust assists this, and prevents droplets from re-circulating

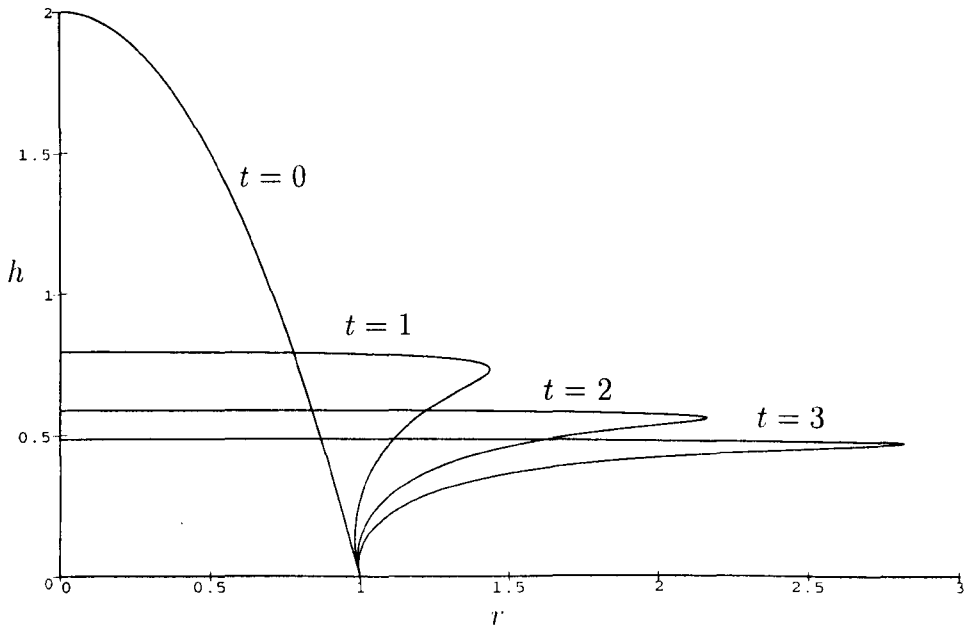

Figure 1.2: Evolution of a drop during spin coating as calculated by Emslie *et al.* [12], for $t = 0$, 1, 2 and 3.

and hitting the wafer which would spoil the coating. At high rotation speeds (typically 1000 to 10,000 rpm) such devices spin low-viscosity fluids to a thickness of a few microns down to a few nanometres.

One of the earliest theoretical analyses of spin coating was performed by Emslie, Bonner & Peck [12] who considered a thin axisymmetric drop of Newtonian fluid on a planar substrate rotating with constant angular velocity. They showed analytically that an initially non-uniform drop becomes increasingly uniform during spinning, and obtained an estimate for the time taken for the thickness of the drop to reduce to a prescribed value. Their solution can be written in the parametric form

$$r = r_0(h_0)\left(1 + \frac{4h_0^2 t}{3}\right)^{\frac{3}{4}}, \qquad h = h_0\left(1 + \frac{4h_0^2 t}{3}\right)^{-\frac{1}{2}}, \tag{1.1}$$

where r is the radius, h is the height, t is time and $r_0 = r_0(h_0)$ is the initial profile of the drop. Figure 1.2 shows the evolution of the parabolic initial profile $h_0(r_0) = 2(1 - r_0^2)$ for $t = 0$, 1, 2 and 3, calculated using Eq. (1.1). Many subsequent authors have extended this pioneering work. Acrivos, Shah & Pe-

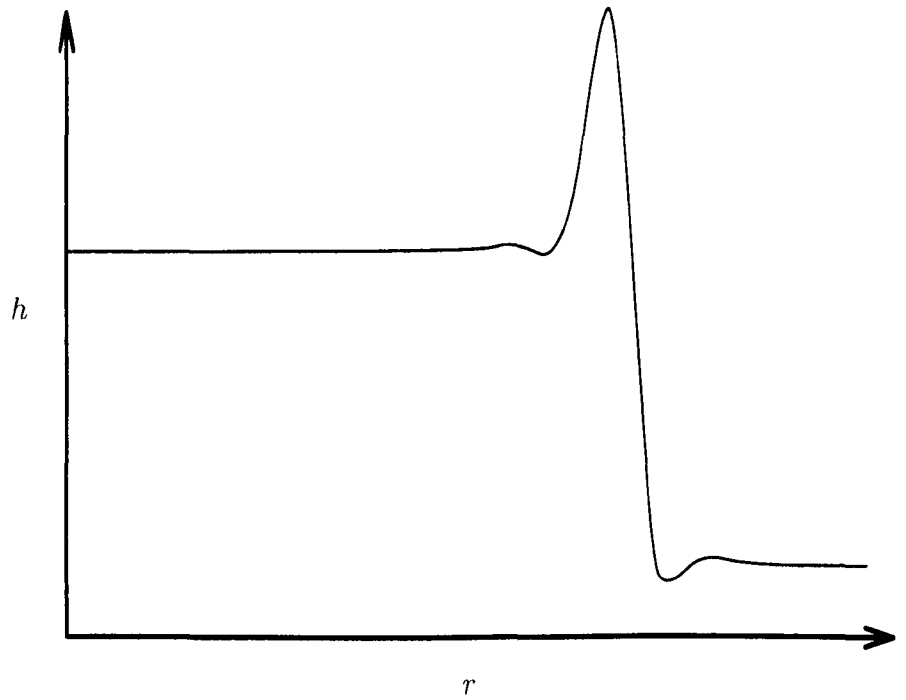

Figure 1.3: Typical leading order composite solution in the limit of weak surface tension for the profile of a drop during spin coating as described by Moriarty *et al.* [43].

tersen [2] examined the spin coating of a non-Newtonian power-law fluid and found that, in contrast to the Newtonian case, even an initially uniform drop will develop non-uniformities as it spreads. Meyerhofer [40] included evaporation effects and found good agreement with experiment if the evaporation rate was assumed to vary as the square root of the angular velocity, and Tu [54], Yanagisawa [63] and Wilson, Hunt & Duffy [61] analysed the effect of different slip models at the fluid/solid interface. Moriarty, Schwartz & Tuck [43] obtained both analytical and numerical solutions for spin coating in the asymptotic limit of weak surface tension using the method of matched asymptotic expansions. In the "outer " region far away from the contact line, the problem is identical to that studied by Emslie *et al.* [12]. In this case, surface-tension effects are only significant in the "inner" region near the contact line in which the free surface profile has a distinctive "capillary ridge". A typical leading order composite solution is shown in Fig. 1.3. Lawrence [31] examined the spin coating of polymer

films including solvent evaporation and gave a prediction for the final dry-film thickness, Lawrence & Zhou [32] studied the effect of various non-Newtonian viscosity models on the final drop thickness, while Jenekhe & Schuldt [24] and Burgess & Wilson [7] investigated the spin coating of Bingham materials. Various other authors have analysed a variety of additional physical effects on the spin coating of a fluid film. Higgins [17] included weak fluid inertia and derived an asymptotic solution for small Reynolds number describing the thinning of a fluid during spin coating which assumed that the interface remained flat during spinning. Bornside, Macosko & Scriven [4] included the effects of variations in concentration, viscosity and diffusivity across the fluid film and concluded that film thinning initially slows down due to a decrease in film thickness and finally stops due to an increase in viscosity of the coating liquid as solvents evaporate. Reisfeld, Bankoff & Davis [46] investigated the linear stability of the free surface in the presence of evaporation and absorption effects. When there is evaporation present, the free surface is stable to perturbations with small wavenumber and transiently stable for larger wavenumbers (transiently stable means that, as time increases, perturbations grow to some finite amplitude but will ultimately decay to zero), and when there is absorption present, the free surface is stable to perturbations with small wavenumbers, transiently stable for intermediate wavenumbers and exponentially unstable for large wavenumbers. Momoniat & Mason [41] investigated the effect of the hitherto neglected Coriolis force on the spin coating of a thin fluid film while neglecting inertia.

Experimental studies of spin coating (see, for example, Melo, Joanny & Fauve [39], Fraysse & Homsy [15] and Spaid & Homsy [50]) show that a drop of Newtonian fluid does indeed become increasingly uniform during spinning, except near the contact line where the capillary ridge develops. Typically, the contact line of the drop initially remains approximately circular as the drop spreads, but at a critical radius the contact line becomes unstable and develops into non-axisymmetric "fingers" distributed roughly equally around the circumference of the drop. This fingering instability arises due to the local variations in the fluid thickness, whereby thicker regions of fluid advance more rapidly over the

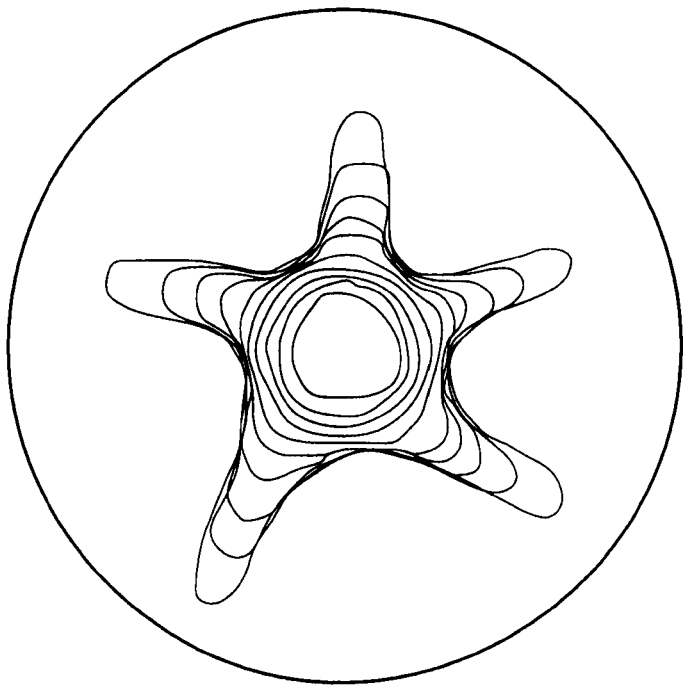

Figure 1.4: Typical plot taken from Spaid & Homsy [50] showing a sequence of pictures of the experimentally-measured contact line of an initially approximately circular drop developing into fingers as it spreads out during spin coating.

substrate. Figure 1.4 is a typical plot taken from Spaid & Homsy [50] showing the experimentally-measured position of the contact line of an initially approximately circular drop developing into fingers as it spreads. Wilson *et al.* [61] were able to obtain good agreement between their numerical calculations for the evolution of the drop radius prior to the onset of fingering and the corresponding experimental results of Fraysse & Homsy [15] and Spaid & Homsy [50]. The linear stability of an initially two-dimensional capillary ridge at an advancing contact line was first studied analytically by Troian, Herbolzheimer, Safran & Joanny [53] who showed that it is always unstable to perturbations in the transverse direction with sufficiently long wavelength. Fraysse & Homsy [15] found that their experimentally-measured azimuthal wavenumber and growth rate of the fingering were in good agreement with the theoretical predictions of Troian *et al.* [53] provided that the critical radius for the onset of the instability was taken from the experiment itself. An extensive review of the literature on spin coating is given by Larson & Rehg [30].

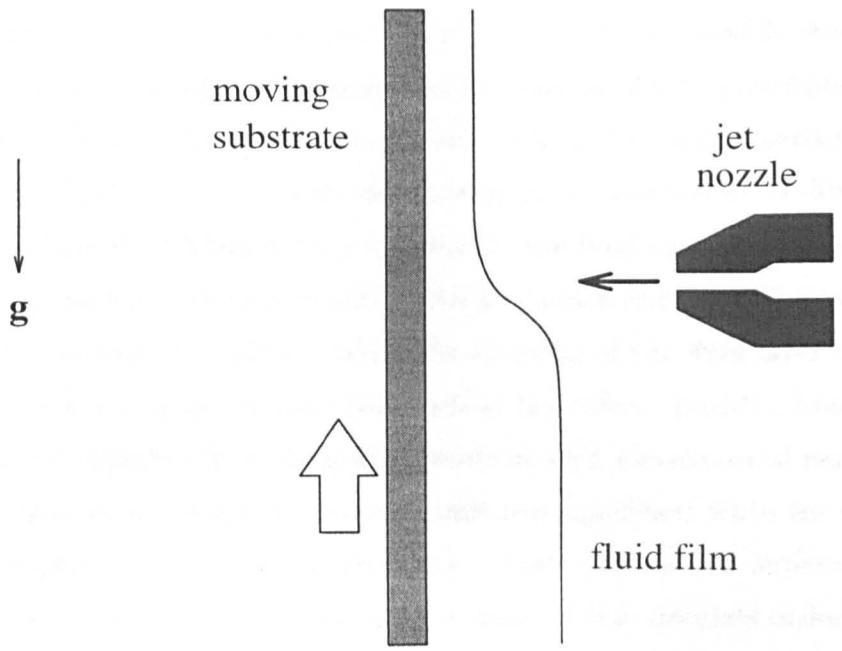

Figure 1.5: Schematic of the jet-stripping process.

The spreading of a thin film due to a jet of air has received less attention thus far. Much of the work that has been done on problems of this kind is motivated by the so-called "jet-stripping" or "air-knife" industrial coating process in which the thickness of a fluid film that has been applied to a moving substrate is controlled by blowing a jet of air onto the film. This process is used in many coating applications such as hot-dip galvanisations of metal strips and wires as well as the deposition of photographic emulsions. Figure 1.5 shows a typical schematic of this process. An upward-moving substrate emerges from a bath and withdraws an amount of coating fluid. A jet produced by an appropriate nozzle (typically a rectangular or annular slit) impinges on the fluid film. The jet (usually air or nitrogen) induces a "runback" flow of the fluid that returns some of the fluid to the coating bath under the action of gravity.

The pioneering steady two-dimensional analysis by Thornton & Graff [52] gave an expression for the final thin-film thickness in terms of speed of the substrate, jet strength, nozzle slot width and distance between the jet nozzle and the fluid, and good agreement was found between the predictions of their an-

alytical model and experimental data. Tuck [55] analysed possible steady-flow solutions, and by considering the characteristic curves of the corresponding unsteady flows, showed that steady flow is stable to long-wavelength perturbations. Ellen & Tu [11] included a non-zero shear stress at the free surface in their model and showed that their analytical prediction for the final coating thickness gave improved agreement with experiment. Tuck & Vanden-Broeck [56] showed that the inclusion of surface tension inhibits the thinning of the fluid layer and gave numerical results to quantify the magnitude of this effect. Buchlin, Manna, Arnalsteen & Riethmuller [6] compared theoretical with experimental results and concluded that surface-tension effects become less significant when the pressure gradient caused by the jet of air increases. They also showed experimentally that for large enough substrate velocities a spray of tiny droplets dislodge from the fluid surface ("splashing") that can ruin the final film thickness, thus putting a practical upper limit on the substrate velocity.

Several other authors have also investigated the effect of a jet of air on a fluid film. Moriarty *et al.* [43] considered the unsteady spreading of a two-dimensional drop of fluid under the action of a jet of air blowing either vertically downwards onto the substrate or parallel to it. In the first case, the jet was modelled as a parabolic pressure distribution in the air, and the shear stress at the free surface of the fluid caused by the air flow was neglected, while in the second case the jet was modelled as a constant shear stress distribution at the free surface of the fluid while the variations in the air pressure were neglected. In both cases, unsteady solutions were obtained both numerically and analytically in the asymptotic limit of weak surface tension (similar to the spin-coating analysis of the same authors described earlier). King, Tuck & Vanden-Broeck [28] studied steady two-dimensional periodic waves on a fluid film on an inclined plane caused by a jet of air flowing upwards over it. King *et al.*'s [28] model used thin aerofoil theory to model the flow of air past the thin film and allowed the external pressure gradient to depend on the shape of the free surface of the film, but assumed that the shear stress at the free surface was constant. King & Tuck [27] studied the corresponding problem for a ridge of fluid of finite width on an inclined plane

and found that steady solutions are possible only if the angle of inclination of the plane to the horizontal is sufficiently small and that below this critical value two steady solutions exist for each inclination angle. Recently Kriegsmann, Miksis & Vanden-Broeck [29] investigated the effect of a steadily-moving exponential pressure distribution on a fluid film on an inclined plane and found that there is a finite range of values of the capillary number where no steady solution exists and where unsteady solutions develop shock-like free-surface profiles.

A related class of problems relevant to the present work concerns the stability and evolution of holes in thin fluid layers. The pioneering work of Taylor & Michael [51] considered the stability of axisymmetric holes in fluid layers of infinite extent lying on a solid horizontal substrate. They showed that a single equilibrium hole exists if the layer is sufficiently thin and that this equilibrium hole is unconditionally unstable. They conjectured that holes with radius smaller than the equilibrium value would close while those with larger radius would open. To test their hypothesis they conducted a series of experiments in which holes were made in a horizontal layer of mercury standing on a glass disc with a series of cylindrical probes of different radii. All holes either opened or closed and the division between the two kinds of behaviour was in good agreement with the theoretically-calculated critical radius. Moriarty & Schwartz [42] and Wilson & Terrill [62] considered the dynamics of axisymmetric laterally-bounded holes in thin fluid layers and showed that for a sufficiently small volume of fluid there are two equilibrium holes, the hole with smaller radius being unstable, and that with larger radius being stable. Figure 1.6 plots typical stable and unstable equilibrium axisymmetric holes with the same volume of fluid, laterally bounded at $r = 1$. Analysis of the stability to non-axisymmetric perturbations and non-linear evolution of these holes has recently been undertaken by López, Miksis & Bankoff [35] who showed that the most unstable wavenumber depends on the radius of the hole and the position of the boundary wall.

The general issue of the stability of thin fluid films has received considerable attention in recent years. The pioneering analysis of the stability of an advancing capillary ridge by Troian *et al.* [53] (revisited in Chapter 4 Sec. 4.3.4) has subse-

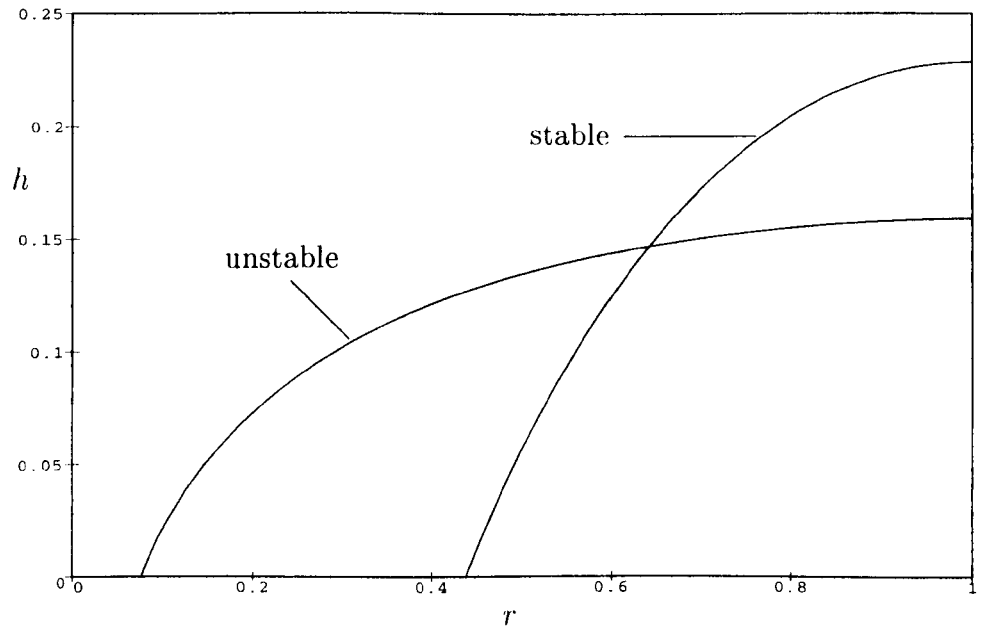

Figure 1.6: Typical stable and unstable equilibrium axisymmetric holes with the same volume of fluid, laterally bounded ar $r = 1$, as studied by Moriarty & Schwartz [42], Wilson & Terrill [62] and López *et al.* [35].

quently been re-examined and generalised by several authors, including Spaid & Homsy [49] who investigated the stability of Newtonian and viscoelastic moving contact lines, by Bertozzi & Brenner [3] who studied the effect of changing the angle of inclination of the plane down which the fluid was draining, by López, Bankoff & Miksis [33] who investigated the stability of non-isothermal spreading on an inclined plane, by López, Miksis & Bankoff [34] who included inertial effects and by Kataoka & Troian [25, 26] who included Marangoni (surface-tension-gradient) effects to study the stability of a thermally-driven climbing film. The linear stability and non-linear evolution of an initially two-dimensional ridge of finite width on an inclined plane was analysed by Hocking [20] and Hocking & Miksis [23]. In particular, Hocking & Miksis [23] found that the quasi-static analysis of Hocking [20] (which predicts that the ridge is most unstable to long-wavelength perturbations in the transverse direction) is appropriate only for very small values of the slip parameter. Relaxing the quasi-static assumption, they concluded that the ridge is always unstable to sufficiently long-wavelength

perturbations in the transverse direction and calculated the most unstable wavelength (the work of Hocking & Miksis [23] is revisited in Chapter 4 Sec. 4.3.3).

In this thesis we shall focus on the interesting behaviour found in both spin-coating and air-jet-blowing problems due to the presence of both surface-tension and moving-contact-line effects. The general issue of the motion of contact lines has been the subject of much debate in recent years (see, for example, the work by Hocking [21]). The key issue is the determination of the relationship between the experimentally-measured macroscopic contact angle θ (inferred from global properties or measured some distance from the contact line) and the speed of the contact line U. One approach takes the view that it is not necessary to model the details of the flow in the vicinity of the contact line, but that one may instead adopt an empirically-determined "Tanner Law" relating U and θ. Greenspan [16] pioneered this approach by proposing a linear relationship, and this was subsequently generalised to a power-law dependence by Ehrhard & Davis [10], who found that a particular cubic power law gave the best fit to their experimental data. This approach has the great practical advantage that the difficult problem of the flow in the vicinity of the contact line is circumvented, and as a result it has been widely used in recent years to study several problems involving the dynamics of thin fluid films. For example, it was used by Greenspan [16] to study the spreading of a drop, by Ehrhard & Davis [10] to study the spreading of a non-isothermal drop, by Ehrhard [9] to study the spreading of a pendent drop, by Braun, Murray, Boettinger & McFadden [5] to study the reactive spreading of a drop, by Wilson & Terrill [62] and López *et al.* [35] to study the opening and closing of a hole in a fluid film, by López *et al.* [33] to study the non-isothermal draining of a fluid film down an inclined plane, by López *et al.* [34] to study the effect of fluid inertia on the draining of a fluid film down an inclined plane and by Wilson & Duffy [60] to study the quasi-static stability of a rivulet draining down a non-uniform substrate. An alternative approach takes the view that, while the former approach may yield physically-reasonable results for relatively little effort, it is conceptually superior to determine the relationship between U and θ analytically rather than impose it (rather like an additional "constitutive

law"). In order to perform this kind of calculation some additional physical effects must be included, but there is currently no agreement on what effects are appropriate. Hocking [18, 19] has determined the relationship between U and θ under the assumptions of a fixed microscopic contact angle and a simple slip model at the substrate, while more recently Hocking [22] included intermolecular forces. On the other hand, Shikhmurzaev [47, 48] modelled the thermodynamic state of the interfacial regions near the contact line, allowing for relaxation in properties of a fluid element as it traverses the contact-line zone. He derived the relationship between θ and U predicted by the model and also showed that the model resolves the stress singularity at a moving contact line. In particular, Shikhmurzaev [48] obtained numerically-calculated examples of non-thin drops spreading on a substrate due to gravity and to rotation of the substrate. For simplicity we shall adopt the first approach in the present work, but shall employ a rather general Tanner Law in Chapters 2 and 3 relating U and θ which incorporates as special cases all the specific forms used in Chapters 5 and 6 and by earlier authors.

1.2 Outline of Thesis

In Chapters 2 and 3 we investigate the quasi-static spreading of a finite-sized thin drop of incompressible, Newtonian fluid on a planar substrate in the presence of a jet of air in both symmetric planar two-dimensional and axisymmetric three-dimensional geometries. Since we shall consider only the leading-order solution in the quasi-static limit in these Chapters, the stress singularity at the moving contact line does not appear explicitly (although, as Hocking [21] has shown, it would do so if we continued the analysis to higher orders). Three specific problems are studied in detail: a jet of air acting normally to the substrate when gravity effects are negligible, a jet of air directed vertically downwards onto a sessile drop on a horizontal substrate and a jet of air directed vertically upwards onto a pendent drop on a horizontal substrate. In Chapter 2 we consider drops without a dry patch (hereafter referred to as "non-annular" drops) and

in Chapter 3 we consider drops with a dry patch at their centre (hereafter referred to as "annular" drops). Since, for the simple model of the jet we shall adopt, the axisymmetric air-jet-blowing problem is identical to the axisymmetric spin-coating problem of a drop of fluid on a horizontal substrate rotating with uniform angular velocity, the results in the axisymmetric case will also apply to the spin-coating problem with an appropriate redefinition of the parameters. For each problem we determine the physically-realisable equilibrium solutions for the profile of the drop and investigate their stability to uniform perturbations in the two-dimensional case and axisymmetric perturbations in the three-dimensional case. An account of the work in Chapters 2 and 3 has recently been published in *Phys. Fluids* (McKinley, Wilson & Duffy [38]).

The next step is to investigate the linear stability to general perturbations for non-zero capillary number. With this in mind, Chapter 4 describes the writing and testing of a numerical finite-difference code that is capable of solving coupled linear differential eigenvalue problems of the kind studied by Troian *et al.* [53], who investigated the linear stability of a capillary ridge on an inclined plane, by Hocking & Miksis [23], who studied the linear stability of a ridge of fluid of finite width on an inclined plane and by López *et al.* [35], who analysed the linear stability of a hole in a laterally-bounded thin film.

In Chapter 5 we investigate the linear stability to both uniform (zero wavenumber) and non-uniform (non-zero wavenumber) perturbations of an initially two-dimensional thin ridge of Newtonian fluid of finite width on a horizontal planar substrate acting under the influence of a jet of air normal to the substrate in the general case of non-zero capillary number. Two problems are considered: the special case when the jet acts at the centre of the ridge (which in two dimensions corresponds to the non-annular problem studied in Chapter 2) and the more general case when the jet acts off-centre (which in two dimensions corresponds to the annular problem studied in Chapter 3). For both problems we confirm and extend the previous analytical results in the special case of quasi-static motion (corresponding to zero capillary number) and investigate numerically the general case of non-zero capillary number. The work in Chapter 5 has been submitted

for publication.

Finally, in Chapter 6 we investigate the linear stability to both axisymmetric (zero wavenumber) and non-axisymmetric (non-zero wavenumber) perturbations of an initially axisymmetric thin drop of Newtonian fluid either on a uniformly rotating substrate or under the influence of a jet of air directed normally towards a stationary substrate in the general case of non-zero capillary number. As before, the results in this Chapter also apply to the spin-coating problem with an appropriate redefinition of the parameters. Two problems are considered: one in which the drop has no dry patch (which in an axisymmetric geometry corresponds to the non-annular problem studied in Chapter 2) and one in which the drop has a dry patch at its centre (which in an axisymmetric geometry corresponds to the annular problem studied in Chapter 3). For both problems we confirm and extend the previous analytical results in the special case of quasi-static motion and investigate numerically the general case of non-zero capillary number. The work in Chapter 6 has also been submitted for publication.

In Chapter 7 we present our conclusions and describe directions of further work.

1.3 Thin-film Equations and Boundary Conditions

In this section we derive the equations and boundary conditions which govern the behaviour of a thin film of Newtonian fluid that will used throughout this thesis. Suppose that we have a incompressible Newtonian fluid of constant density ρ and constant viscosity μ whose motion is governed by the Navier-Stokes equations (see, for example, Acheson [1]), given by

$$\rho(\mathbf{u}_t + (\mathbf{u}\cdot\nabla)\mathbf{u}) = -\nabla p + \mathbf{g} + \mu\nabla^2\mathbf{u}, \tag{1.2}$$

$$\nabla\cdot\mathbf{u} = 0, \tag{1.3}$$

where $\mathbf{u}$ is the fluid velocity, p is the pressure, t is time and $\mathbf{g}$ is the acceleration due to gravity. Our aim is to obtain the simplified form of Eqs. (1.2) and (1.3)

appropriate when the fluid film is thin and slender. If we let H denote a typical vertical length scale and L a typical horizontal length scale, then this means that

$$\delta = \frac{H}{L} \ll 1, \tag{1.4}$$

where δ is the aspect ratio.

1.3.1 Cartesian Coordinates

Using Cartesian coordinates (x, y, z) with z directed vertically upwards, the Navier-Stokes equations take the form

$$\rho(u_t + uu_x + vu_y + wu_z) = -p_x + \mu(u_{xx} + u_{yy} + u_{zz}), \tag{1.5}$$

$$\rho(v_t + uv_x + vv_y + wv_z) = -p_y + \mu(v_{xx} + v_{yy} + v_{zz}), \tag{1.6}$$

$$\rho(w_t + uw_x + vw_y + ww_z) = -p_z - \rho g + \mu(w_{xx} + w_{yy} + w_{zz}), \tag{1.7}$$

$$u_x + v_y + w_z = 0, \tag{1.8}$$

where the fluid velocity has been written $\mathbf{u} = (u, v, w)$ and $\mathbf{g} = (0, 0, -g)$ denotes the acceleration due to gravity. We introduce the scalings $u = Uu'$, $v = Uv'$, $t = Lt'/U$, $w = S_1 w'$, $x = Lx'$, $y = Ly'$, $z = Hz'$, $p = S_2 p'$ and $g = S_3 g'$ where U is the horizontal velocity scale; the scalings S_1, S_2 and S_3 will be determined subsequently. Substituting these rescaled variables into Eqs. (1.5) – (1.8) and dropping the primes at once for simplicity, the mass conservation condition (1.8) yields

$$\frac{U}{L}u_x + \frac{U}{L}v_y + \frac{S_1}{H}w_z = 0,$$

and hence if we choose $S_1 = UH/L$, then Eq. (1.8) becomes

$$u_x + v_y + w_z = 0. \tag{1.9}$$

The scaled version of Eq. (1.5) is given by

$$R_e(u_t + uu_x + vu_y + wu_z) = -\frac{S_2 L}{\mu U}p_x + \left(u_{xx} + u_{yy} + \frac{1}{\delta^2}u_{zz}\right), \tag{1.10}$$

where $R_e = \rho UL/\mu$ is the Reynolds number. The viscous term dominates the inertia term when

$$R_e\delta^2 \ll 1, \tag{1.11}$$

i.e. when the *reduced* Reynolds number is small. In order to keep the pressure term in Eq. (1.10) at leading order, we choose $S_2 = \mu UL/H^2$. Hence to leading order in δ, Eq. (1.10) yields

$$u_{zz} = p_x. \tag{1.12}$$

The scaled version of Eq. (1.6) is given by

$$R_e(v_t + uv_x + vv_y + wv_z) = -\frac{1}{\delta^2}p_y + \left(v_{xx} + v_{yy} + \frac{1}{\delta^2}v_{zz}\right), \tag{1.13}$$

and to leading order in δ, Eq. (1.13) yields

$$v_{zz} = p_y. \tag{1.14}$$

The scaled version of Eq. (1.7) is given by

$$R_e(w_t + uw_x + vw_y + ww_z) = -\frac{1}{\delta^4}p_z - \frac{\rho S_3 L^3}{\mu UH}g + \left(w_{xx} + w_{yy} + \frac{1}{\delta^2}w_{zz}\right). \tag{1.15}$$

In order to keep the gravity term in Eq. (1.15) at leading order, we choose $S_3 = \mu UL/\rho H^3$. Hence to leading order in δ, Eq. (1.15) yields

$$0 = p_z + g. \tag{1.16}$$

Written in Cartesian coordinates the appropriate boundary conditions for Eqs. (1.5) - (1.8) are given by

$$u = v = 0 \quad \text{on} \quad z = 0, \tag{1.17}$$

$$w = h_t + uh_x + vh_y \quad \text{on} \quad z = h, \tag{1.18}$$

$$\mathbf{n}\cdot\mathbf{T}\cdot\mathbf{n} = -P - 2\tau H \quad \text{on} \quad z = h, \tag{1.19}$$

$$\mathbf{n}\cdot\mathbf{T}\cdot\mathbf{t_1} = 0 \quad \text{on} \quad z = h, \tag{1.20}$$

$$\mathbf{n}\cdot\mathbf{T}\cdot\mathbf{t_2} = 0 \quad \text{on} \quad z = h, \tag{1.21}$$

where $P = P(x)$ is the air pressure, τ is the coefficient of surface tension, $z = h(x, y, t)$ is the free surface of the fluid film, $\mathbf{T}$ is the stress tensor given by

$$\mathbf{T} = \begin{pmatrix} -p + 2\mu u_x & \mu(u_y + v_x) & \mu(u_z + w_x) \\ \mu(v_x + u_y) & -p + 2\mu v_y & \mu(v_z + w_y) \\ \mu(w_x + u_z) & \mu(w_y + v_z) & -p + 2\mu w_z \end{pmatrix}, \tag{1.22}$$

$\mathbf{n}$ is the normal unit vector to the free surface given by

$$\mathbf{n} = \frac{(-h_x, -h_y, 1)}{(1 + h_x^2 + h_y^2)^{\frac{1}{2}}}, \tag{1.23}$$

$\mathbf{t}_1$ and $\mathbf{t}_2$ are tangential unit vectors to the free surface (such that $\mathbf{t}_1 \cdot \mathbf{t}_2 = 0$) given by

$$\mathbf{t_1} = \frac{(1, 0, h_x)}{(1 + h_x^2 + h_y^2)^{\frac{1}{2}}}, \tag{1.24}$$

$$\mathbf{t_2} = \frac{\left(\frac{-h_x h_y}{h_x^2 + 1}, 1, \frac{h_y}{h_x^2 + 1}\right)}{(1 + h_x^2 + h_y^2)^{\frac{1}{2}}}, \tag{1.25}$$

and $2H = \nabla \cdot \mathbf{n}$ where H is the mean curvature of the free surface. Equation (1.17) is the no-slip condition at the solid substrate, Eq. (1.18) is the free-surface kinematic condition, Eq. (1.19) balances normal stress, air pressure and surface tension forces and Eqs. (1.20) and (1.21) require that the tangential stress at the free surface is zero. We now derive the thin-film versions of Eqs. (1.17) – (1.21). We use the same scalings as before together with $P = \mu U L P'/H^2$ and $\tau = S_4 \tau'$, where S_4 will be determined subsequently. Substituting into Eqs. (1.17) – (1.21) and again dropping the primes at once for simplicity, the scaled version of Eq. (1.17) is simply

$$u = v = 0 \quad \text{on} \quad z = 0. \tag{1.26}$$

The scaled version of Eq. (1.18) is given by

$$w = h_t + u h_x + v h_y \quad \text{on} \quad z = h. \tag{1.27}$$

The scaled version of Eq. (1.19) is given by

$$h_x^2(-p + 2\delta^2 u_x) + 2\delta^2 h_x h_y (u_y + v_x) - 2h_x(u_z + \delta^2 w_x) - 2h_y(v_z + \delta^2 w_y)$$
$$+h_y^2(-p + 2\delta^2 v_y) - \frac{1}{\delta^2} p + 2w_z = -\frac{1}{\delta^2} P + \frac{S_4 \tau H}{\mu U L}(h_{xx} + h_{yy})(1 + \delta^2 h_x^2 + \delta^2 h_y^2)^{\frac{1}{2}}. \tag{1.28}$$

In order to keep the curvature term in Eq. (1.28) at leading order, we choose $S_4 = \mu U L^3/H^3$. Hence to leading order in δ, Eq. (1.28) yields

$$p = P - \tau \nabla^2 h \quad \text{on} \quad z = h, \tag{1.29}$$

where

$$\nabla^2 = \frac{\partial^2}{\partial x^2} + \frac{\partial^2}{\partial y^2}.$$

The scaled version of Eq. (1.20) is given by

$$2\delta h_x(w_z - u_x) - \delta h_y(u_y + v_x) + \frac{1}{\delta}u_z + \delta w_x - \delta h_x^2(\delta^2 w_x + u_z) - \delta h_x h_y(\delta^2 w_y + v_z) = 0. \tag{1.30}$$

To leading order in δ, Eq. (1.30) yields

$$u_z = 0 \quad \text{on} \quad z = h. \tag{1.31}$$

The scaled version of Eq. (1.21) is given by

$$\begin{aligned} \delta^3 h_x^2 h_y \left(\frac{2}{\delta^2}p - 2u_x - v_y\right) + \delta^3 h_x h_y^2(u_y + v_x) - 2\delta^2 h_x h_y \left(\frac{1}{\delta}u_z + \delta w_x\right) \\ -\delta h_x(\delta^2 h_x^2 + 1)(v_x + u_y) + (\delta^2 h_x^2 + 1)\left(\frac{1}{\delta}v_z + \delta w_y\right) \\ -\delta^2 h_y^2\left(\delta w_y + \frac{1}{\delta}v_z\right) + \delta h_y(2w_z - v_y) = 0. \end{aligned} \tag{1.32}$$

To leading order in δ, Eq. (1.32) yields

$$v_z = 0 \quad \text{on} \quad z = h. \tag{1.33}$$

In dimensional form, the leading-order equations and boundary conditions are given by

$$0 = p_z + \rho g, \tag{1.34}$$

$$\mu u_{zz} = p_x, \tag{1.35}$$

$$\mu v_{zz} = p_y, \tag{1.36}$$

$$u_x + v_y + w_z = 0, \tag{1.37}$$

subject to

$$u = v = 0 \quad \text{on} \quad z = 0, \tag{1.38}$$

$$\mu u_z = 0, \quad \mu v_z = 0 \quad \text{on} \quad z = h, \tag{1.39}$$

$$p = P - \tau\nabla^2 h \quad \text{on} \quad z = h, \tag{1.40}$$

$$w = h_t + uh_x + vh_y \quad \text{on} \quad z = h. \tag{1.41}$$

1.3.2 Cylindrical Polar Coordinates

Using cylindrical polar coordinates (r, φ, z) with z directed vertically upwards, the Navier-Stokes equations take the form

$$\rho\left(u_t + uu_r + \frac{v}{r}u_\varphi + wu_z - \frac{v^2}{r}\right) = -p_r + \mu\left(\nabla^2 u - \frac{u}{r^2} - \frac{2}{r^2}v_\varphi\right), \quad (1.42)$$

$$\rho\left(v_t + uv_r + \frac{v}{r}v_\varphi + wv_z + \frac{uv}{r}\right) = -\frac{1}{r}p_\varphi + \mu\left(\nabla^2 v + \frac{2}{r^2}u_\varphi - \frac{v}{r^2}\right), \quad (1.43)$$

$$\rho\left(w_t + uw_r + \frac{v}{r}w_\varphi + ww_z\right) = -p_z - \rho g + \mu\nabla^2 w, \quad (1.44)$$

$$\frac{1}{r}(ru)_r + \frac{1}{r}v_\varphi + w_z = 0, \quad (1.45)$$

where

$$\nabla^2 = \frac{1}{r}\frac{\partial}{\partial r}\left(r\frac{\partial}{\partial r}\right) + \frac{1}{r^2}\frac{\partial^2}{\partial \varphi^2},$$

and, as before, the fluid velocity has been written $\mathbf{u} = (u, v, w)$ and $\mathbf{g} = (0, 0, -g)$. The corresponding boundary conditions are given by

$$u = v = 0 \quad \text{on} \quad z = 0, \quad (1.46)$$

$$w = h_t + uh_x + \frac{v}{r}h_\varphi \quad \text{on} \quad z = h, \quad (1.47)$$

$$\mathbf{n}\cdot\mathbf{T}\cdot\mathbf{n} = -P - 2\tau H \quad \text{on} \quad z = h, \quad (1.48)$$

$$\mathbf{n}\cdot\mathbf{T}\cdot\mathbf{t_1} = 0 \quad \text{on} \quad z = h, \quad (1.49)$$

$$\mathbf{n}\cdot\mathbf{T}\cdot\mathbf{t_2} = 0 \quad \text{on} \quad z = h, \quad (1.50)$$

where $P = P(r)$ is the air pressure and the stress tensor $\mathbf{T}$ is given by

$$\mathbf{T} = \begin{pmatrix} -p + 2\mu u_r & \mu r\frac{\partial}{\partial r}\left(\frac{v}{r}\right) + \frac{\mu}{r}u_\varphi & \mu(u_z + w_r) \\ \mu r\frac{\partial}{\partial r}\left(\frac{v}{r}\right) + \frac{\mu}{r}u_\varphi & -p + \frac{2\mu}{r}(v_\varphi + u) & \mu\left(\frac{1}{r}w_\varphi + v_z\right) \\ \mu(u_z + w_r) & \mu\left(\frac{1}{r}w_\varphi + v_z\right) & -p + 2\mu w_z \end{pmatrix}, \quad (1.51)$$

and $\mathbf{n}$, $\mathbf{t}_1$ and $\mathbf{t}_2$ are given by

$$\mathbf{n} = \frac{\left(-h_r, -\frac{1}{r}h_\varphi, 1\right)}{\left(1 + h_r^2 + \frac{h_\varphi^2}{r^2}\right)^{\frac{1}{2}}}, \quad (1.52)$$

$$\mathbf{t_1} = \frac{(1, 0, h_r)}{\left(1 + h_r^2 + \frac{h_\varphi^2}{r^2}\right)^{\frac{1}{2}}}, \tag{1.53}$$

$$\mathbf{t_2} = \frac{\left(\frac{-h_r h_\varphi}{r(h_r^2+1)}, 1, \frac{h_\varphi}{r(h_r^2+1)}\right)}{\left(1 + h_r^2 + \frac{h_\varphi^2}{r^2}\right)^{\frac{1}{2}}}. \tag{1.54}$$

As before, Eq. (1.46) is the no-slip condition at the solid substrate, Eq. (1.47) is the free-surface kinematic condition, Eq. (1.48) balances normal stress, air pressure and surface tension forces and Eqs. (1.49) and (1.50) require that the tangential stress at the free surface is zero. The analysis for this case follows exactly as for the Cartesian case. In dimensional form, the leading-order equations and boundary conditions are given by

$$0 = p_z + \rho g, \tag{1.55}$$

$$\mu u_{zz} = p_r, \tag{1.56}$$

$$\mu v_{zz} = \frac{1}{r} p_\varphi, \tag{1.57}$$

$$\frac{1}{r}(ru)_r + \frac{1}{r} v_\varphi + w_z = 0, \tag{1.58}$$

subject to

$$u = v = 0 \quad \text{on} \quad z = 0, \tag{1.59}$$

$$\mu u_z = 0, \quad \mu v_z = 0 \quad \text{on} \quad z = h, \tag{1.60}$$

$$p = P - \tau \nabla^2 h \quad \text{on} \quad z = h, \tag{1.61}$$

$$w = h_t + u h_r + \frac{v}{r} h_\varphi \quad \text{on} \quad z = h. \tag{1.62}$$

Chapter 2

Quasi-static Analysis of a Non-annular Drop

2.1 Introduction

In this Chapter we investigate the quasi-static spreading of a finite-sized thin drop of incompressible Newtonian fluid on a planar substrate in the presence of a jet of air in both symmetric planar two-dimensional and axisymmetric three-dimensional geometries. Three specific problems are studied in detail: a jet of air acting normally to the substrate when gravity effects are negligible, a jet of air directed vertically downwards onto a sessile drop on a horizontal substrate and a jet of air directed vertically upwards onto a pendent drop on a horizontal substrate. In this Chapter we restrict our attention to drops without a dry patch ("non-annular" drops) and examine drops with a dry patch at their centre ("annular" drops) in Chapter 3. For each problem we determine the physically-realisable equilibrium solutions for the profile of the drop and investigate their stability to uniform perturbations in the two-dimensional case and axisymmetric perturbations in the three-dimensional case. Note that the restricted class of perturbations considered here does not include the (non-uniform and non-axisymmetric) fingering instabilities described in Chapter 1. Linear stability analysis for non-uniform and non-axisymmetric perturbations is discussed in Chapters 5 and 6.

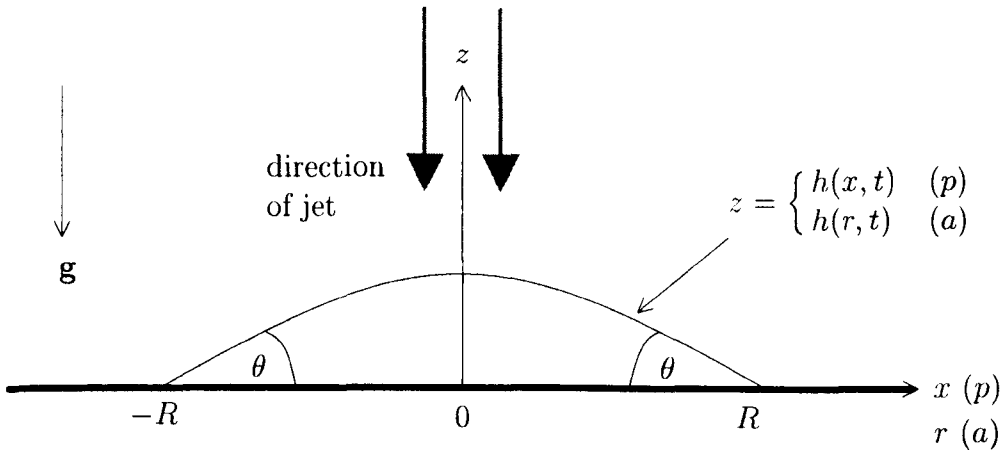

Figure 2.1: Geometry of the non-annular problem.

2.2 Problem Formulation

Consider a constant volume of incompressible Newtonian fluid with constant viscosity μ, density ρ and surface tension τ spreading on a solid horizontal planar substrate in the presence of a jet of air. We analyse both the symmetric planar two-dimensional case, denoted by (p), and the axisymmetric three-dimensional case, denoted by (a), for which we employ Cartesian coordinates (x, z) and cylindrical polar coordinates (r, z) respectively, with the z-axis vertically upwards or downwards as appropriate. The thickness of the fluid film is denoted by $z = h(x,t)$ (p) or $z = h(r,t)$ (a), where t denotes time, and the velocity of the fluid is denoted by $\mathbf{u} = \mathbf{u}(x,z,t)$ (p) or $\mathbf{u} = \mathbf{u}(r,z,t)$ (a). Following Moriarty *et al.* [43] we model the jet of air as a parabolic pressure distribution in the air so that $P = p_0 - kx^2/2$ (p) or $P = p_0 - kr^2/2$ (a), where P denotes the pressure, p_0 is the maximum value of the air pressure at the centre of the drop and k is a positive constant; the shear stress at the free surface of the fluid caused by the air flow is assumed to be negligible. The geometry of the problem in the case of a sessile drop is shown in Fig. 2.1; the only difference in the pendent case is that the direction of gravity is reversed.

We assume that the speed of the contact line, at position $x = R(t)$ (p) or

$r = R(t)$ (a), is related to the contact angle $\theta = \theta(t)$ by the general Tanner Law

$$R_t = \kappa F\left(\frac{\theta}{\theta_0}\right), \tag{2.1}$$

where κ is an empirically-determined positive constant with dimensions of velocity, $F(\theta/\theta_0)$ is an empirically-determined function satisfying $F(1) = 0$, and $\theta_0 > 0$ is the equilibrium contact angle. Typically $F(\theta/\theta_0)$ is a monotonically-increasing function and so its first non-zero derivative at $\theta = \theta_0$ will be positive and of odd order.

From the results given in Chapter 1 the conventional lubrication approximation to the governing Navier-Stokes equations yields

$$0 = p_z + \rho g, \tag{2.2}$$

$$\begin{cases} \mu u_{zz} = p_x, & (p) \\ \mu u_{zz} = p_r, & (a) \end{cases} \tag{2.3}$$

$$\begin{cases} u_x + w_z = 0, & (p) \\ \dfrac{1}{r}(ru)_r + w_z = 0, & (a) \end{cases} \tag{2.4}$$

where g denotes acceleration due to gravity, subject to the boundary conditions

$$u = 0 \quad \text{on} \quad z = 0, \tag{2.5}$$

$$\mu u_z = 0 \quad \text{on} \quad z = h, \tag{2.6}$$

$$\begin{cases} p = p_0 - \dfrac{kx^2}{2} - \tau h_{xx} & (p) \\ p = p_0 - \dfrac{kr^2}{2} - \dfrac{\tau}{r}(rh_r)_r & (a) \end{cases} \quad \text{on} \quad z = h, \tag{2.7}$$

$$\begin{cases} w = h_t + uh_x & (p) \\ w = h_t + uh_r & (a) \end{cases} \quad \text{on} \quad z = h, \tag{2.8}$$

where the fluid velocity has been written $\mathbf{u}=(u, w)$ in the appropriate coordinates. Equation (2.5) is the no-slip condition at the substrate, Eq. (2.6) represents zero tangential stress at the free surface and Eq. (2.7) is the normal stress

condition which includes both the effects of surface tension and the non-uniform external pressure loading caused by the jet of air. Equation (2.8) is the kinematic free-surface condition which can be used with Eq. (2.4) to derive the flux condition

$$\begin{cases} h_t + Q_x = 0, & (p) \\ h_t + \dfrac{1}{r}(rQ)_r = 0, & (a) \end{cases} \tag{2.9}$$

where Q denotes the flux per unit length (p) or circumference (a), defined by

$$Q = \int_0^h u \, \mathrm{d}z. \tag{2.10}$$

Solving Eqs. (2.2) – (2.7) for u allows Q to be evaluated from Eq. (2.10) and substituting Q into Eq. (2.9) gives the governing equation for h.

We non-dimensionalise the problem using a characteristic horizontal length scale L (to be defined subsequently) and κ as the characteristic horizontal velocity scale. The corresponding non-dimensional variables are defined by $x = Lx'$, $r = Lr'$, $R = LR'$, $h = \theta_0 Lh'$, $t = Lt'/\kappa$ and $\theta = \theta_0\theta'$. Dropping the primes at once for simplicity we obtain the non-dimensional version of the governing equation, namely

$$\begin{cases} Ch_t + \left[\dfrac{h^3}{3}\left((h_{xx} - G^2 h)_x + Jx\right)\right]_x = 0, & (p) \\ Ch_t + \dfrac{1}{r}\left[\dfrac{rh^3}{3}\left\{\left(\dfrac{1}{r}(rh_r)_r - G^2 h\right)_r + Jr\right\}\right]_r = 0, & (a) \end{cases} \tag{2.11}$$

together with the non-dimensional version of Eq. (2.1), namely

$$R_t = F(\theta). \tag{2.12}$$

The constant $J = kL^3/\tau\theta_0$ is a non-dimensional measure of the jet strength, $C = \kappa\mu/\tau\theta_0^3$ is the capillary number and $G^2 = \rho g L^2/\tau$ is the Bond number. The appropriate boundary conditions for Eq. (2.11) are

$$h(R, t) = 0, \tag{2.13}$$

$$\begin{cases} h_x(R, t) = -\theta, & (p) \\ h_r(R, t) = -\theta, & (a) \end{cases} \tag{2.14}$$

together with the regularity conditions

$$\begin{cases} h_x(0,t) = 0, & (p) \\ h_r(0,t) = 0, & (a) \end{cases} \tag{2.15}$$

$$Q(0,t) = 0, \tag{2.16}$$

which must be satisfied together with appropriate initial conditions for h and R. The volume of the drop is given by

$$\begin{cases} 2V = 2\int_0^R h \, \mathrm{d}x, & (p) \\ 2\pi V = 2\pi \int_0^R hr \, \mathrm{d}r. & (a) \end{cases} \tag{2.17}$$

If we identify the dimensional jet strength k with $\rho\omega^2$ then Eq. (2.11)(a) is exactly the same as the corresponding equation obtained in the special case $G = 0$ by Moriarty *et al.* [43] (their Eq. 30) for a thin axisymmetric fluid film spreading under the action of the centrifugal force on a substrate rotating uniformly with angular speed ω. Hence all our results for the axisymmetric air-jet-blowing problem also apply to the axisymmetric spin-coating problem. We note, however, that as Emslie *et al.* [12] pointed out, in this problem the Coriolis force can be properly neglected compared to the centrifugal force (as it was by Emslie *et al.* [12] and Moriarty *et al.* [43]) only if the fluid motion is sufficiently slow.

2.3 Quasi-static Motion

In the limit of small capillary number, $C \to 0$, the contact line moves slowly relative to the bulk of the fluid and so the dynamics of the motion are controlled by those of the contact line. At leading order in $C \ll 1$ we drop the unsteady term in Eq. (2.11) and so the flux is constant; then by Eq. (2.16) it is zero everywhere. Hence we obtain a third-order ordinary differential equation for the thickness of the drop:

$$\begin{cases} (h_{xx} - G^2 h)_x + Jx = 0, & (p) \\ \left(h_{rr} + \dfrac{h_r}{r} - G^2 h\right)_r + Jr = 0, & (a) \end{cases} \tag{2.18}$$

to be integrated subject to Eqs. (2.13) – (2.15). The solution for h is easily obtained and can be written in the form

$$h = \theta f(\cdot, R) + Jg(\cdot, R), \tag{2.19}$$

where the symbol "$\cdot$" denotes x (p) or r (a) and the functions $f(\cdot, R)$ and $g(\cdot, R)$ are given by

$$\begin{cases} f(x,R) = \dfrac{\cosh GR - \cosh Gx}{G \sinh GR}, & (p) \\ f(r,R) = \dfrac{I_0(GR) - I_0(Gr)}{GI_1(GR)}, & (a) \end{cases} \tag{2.20}$$

$$\begin{cases} g(x,R) = \dfrac{2R(\cosh GR - \cosh Gx) + G \sinh GR(x^2 - R^2)}{2G^3 \sinh GR}, & (p) \\ g(r,R) = \dfrac{2R(I_0(GR) - I_0(Gr)) + GI_1(GR)(r^2 - R^2)}{2G^3 I_1(GR)}, & (a) \end{cases} \tag{2.21}$$

where $I_0(\cdot)$ and $I_1(\cdot)$ are modified Bessel functions of the first kind. The volume of this quasi-static drop is given by

$$V = \theta S(R) + JT(R), \tag{2.22}$$

where the functions $S = S(R)$ and $T = T(R)$ are given by

$$S(R) = \begin{cases} \dfrac{GR \cosh GR - \sinh GR}{G^2 \sinh GR}, & (p) \\ \dfrac{GR^2 I_0(GR) - 2RI_1(GR)}{2G^2 I_1(GR)}, & (a) \end{cases} \tag{2.23}$$

$$T(R) = \begin{cases} \dfrac{3GR^2 \cosh GR - 3R \sinh GR - G^2 R^3 \sinh GR}{3G^4 \sinh GR}, & (p) \\ \dfrac{4GR^3 I_0(GR) - 8R^2 I_1(GR) - G^2 R^4 I_1(GR)}{8G^4 I_1(GR)}. & (a) \end{cases} \tag{2.24}$$

Note that the functions $f(\cdot, R)$ and $S(R)$ are precisely the familiar expressions for h and V in the absence of blowing ($J = 0$).

When $g \neq 0$ we can, without loss of generality, choose the horizontal length-scale L to be the capillary length $(\tau/\rho g)^{1/2}$ (corresponding to setting $|G| = 1$). Alternatively, whatever the value of g, we can (again without loss of generality)

choose either $L = (\tau\theta_0/k)^{1/3}$ (corresponding to setting $J = 1$), or $L = (V/\theta_0)^{1/2}$ (p), $L = (V/\theta_0)^{1/3}$ (a) (corresponding to setting $V = 1$). Of course all of these choices are equally valid; however in order to treat clearly both the problem of a drop with fixed volume under a jet of varying strength and the problem of a drop of variable volume under a jet of fixed strength we need to retain both the parameters V and J explicitly in what follows. We therefore choose L to be the capillary length, and so the sessile ($g > 0$) and pendent ($g < 0$) cases correspond to $G = 1$ and $G = i$ respectively. The special case of zero gravity corresponds to the limit $G \to 0$, and in this case L remains arbitrary.

Rearranging Eq. (2.22) we obtain an expression for the contact angle θ for constant $V = V_0$ and $J = J_0$:

$$\theta = \frac{V_0 - J_0 T(R)}{S(R)}. \tag{2.25}$$

Substituting this expression for θ into Eq. (2.12) we obtain a non-linear first-order differential equation for the speed of the contact line, namely

$$R_t = F\left(\frac{V_0 - J_0 T(R)}{S(R)}\right), \tag{2.26}$$

to be solved subject to an appropriate initial condition on $R(t)$.

2.4 Equilibrium Solutions

In equilibrium $\theta = 1$ and $R = R_0$, say. Using Eq. (2.22) we can either write the volume $V = V(R_0)$ as a function of R_0 for fixed $J = J_0$ in the form

$$V(R_0) = S(R_0) + J_0 T(R_0), \tag{2.27}$$

or write the jet strength $J = J(R_0)$ as a function of R_0 for fixed $V = V_0$ in the form

$$J(R_0) = \frac{V_0 - S(R_0)}{T(R_0)}. \tag{2.28}$$

The possible equilibrium positions of the contact line $R = R_0$ are the solutions of $V = V_0$ for $J = J_0$ (where $V_0 > 0$ and $J_0 > 0$ are prescribed constants) and so R_0 satisfies

$$V_0 = S(R_0) + J_0 T(R_0). \tag{2.29}$$

2.5 Stability Analysis

To determine the stability of an equilibrium drop of radius $R = R_0$ to small uniform (p) or axisymmetric (a) perturbations we write $R(t) = R_0 + R^1(t)$ and expand Eq. (2.26) for small R^1 to yield

$$(R^1)_t = \frac{M(\lambda R^1)^m}{m!}, \tag{2.30}$$

where $M = \mathrm{d}^m F(\theta)/\mathrm{d}\theta^m|_{\theta=1} > 0$ ($m = 1, 3, 5, \ldots$) is the first non-zero derivative of $F(\theta)$ evaluated at $\theta = 1$ and λ is a constant given by

$$\lambda = -\frac{S'(R_0) + J_0 T'(R_0)}{S(R_0)}. \tag{2.31}$$

Equation (2.30) is easily solved to yield

$$R^1 = \begin{cases} \bar{R}e^{\lambda M t} & \text{if } m = 1, \\ \bar{R}\left(1 - \dfrac{(m-1)M(\lambda\bar{R})^m t}{\bar{R}m!}\right)^{-\frac{1}{m-1}} & \text{if } m = 3, 5, 7, \ldots, \end{cases} \tag{2.32}$$

where $\bar{R} = R^1(0)$ is the initial perturbation to the radius of the drop. Equation (2.32) shows that an equilibrium drop is unstable to small perturbations when $\lambda > 0$ and stable when $\lambda < 0$. Small perturbations grow or decay exponentially when $m = 1$ and algebraically when $m = 3, 5, 7, \ldots$. Examining Eq. (2.31) shows that for marginal stability we require

$$\frac{V'(R_0)}{S(R_0)} = 0, \tag{2.33}$$

where $V(R_0)$ is given by Eq. (2.27), or alternatively, we can write Eq. (2.33) in the equivalent form

$$\frac{J'(R_0)T(R_0)}{S(R_0)} = 0, \tag{2.34}$$

where $J(R_0)$ is given by Eq. (2.28).

Hereafter, we drop the zero subscript on R for clarity.

2.6 Results

2.6.1 Explanation of Figures

In what follows we present results for both the problem of a drop with fixed volume under a jet of varying strength (that is, variable J and fixed V) and

the problem of a drop of variable volume under a jet of fixed strength (that is, variable V and fixed J) for both sessile and pendent drops and in the special case of zero gravity. Since the results for the planar case are qualitatively similar to the axisymmetric case we present the plots for the latter case only, although relevant results for the planar case are given where appropriate for completeness.

Figure 2.2 shows plots of J against R for three values of V_0 in the zero-gravity case, and corresponding typical drop profiles are shown in Fig. 2.3. Figure 2.4 shows plots of V against R for three values of J_0 in the zero-gravity case; the drop profiles shown in Fig. 2.3 are again typical. Figure 2.5 shows an example of the contact angle θ plotted against radius R in the zero-gravity case. Figure 2.6 shows corresponding examples of the evolution of the radius R as a function of time t for a particular choice of $F(\theta)$, while Figs. 2.7 and 2.8 show corresponding examples of the evolution of the profile of the drop. Figures 2.9 and 2.10 show plots of J against R and V against R respectively in the case of a sessile drop, and the corresponding results in the pendent case are given in Figs. 2.11 and 2.12. Results for the pendent case corresponding to Figs. 2.5–2.8 in the zero-gravity case are given in Figs. 2.13–2.16. Finally, Fig. 2.17 shows an example of the contact angle θ plotted against radius R in the pendent case for a special value of J.

Since we are concerned only with $V > 0$, $J > 0$ and $R > 0$, all the plots of V against R and J against R are restricted to the first quadrant. On these figures the possible equilibrium solutions are classified as either physically-realisable or not physically-realisable (the latter implying that $h < 0$ at some part of the drop) and either stable ($\lambda < 0$) or unstable ($\lambda > 0$). This classification is indicated as follows:

- a solid thick line indicates stable and physical drop profiles,
- a solid thin line indicates stable but unphysical drop profiles,
- a dashed thick line indicates physical but unstable drop profiles,
- a dashed thin line indicates drop profiles that are both unstable and un-

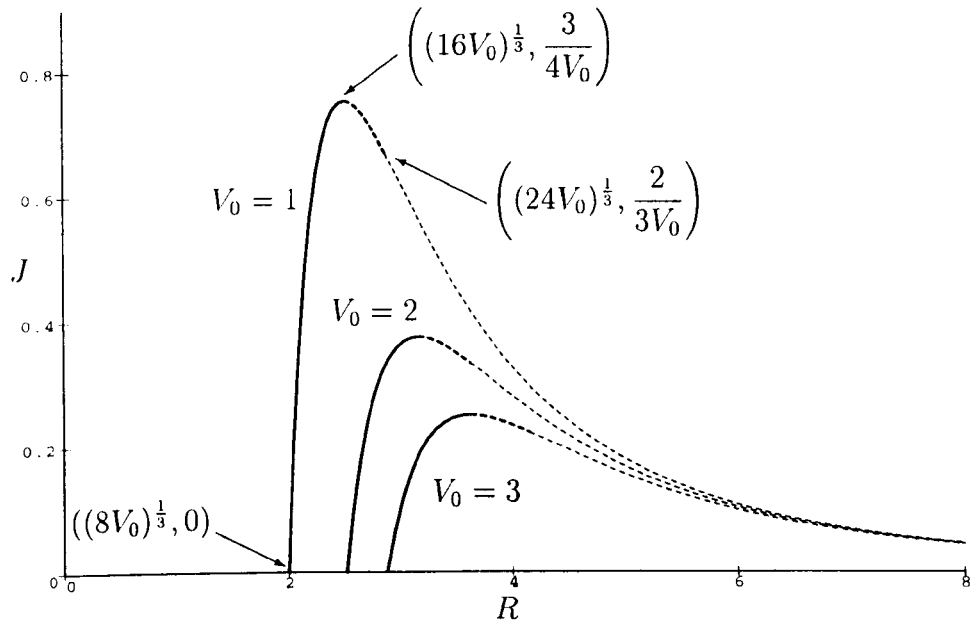

Figure 2.2: Plot of jet strength J against radius R for an axisymmetric drop in the case of zero gravity for $V_0 = 1, 2, 3$. The line styles are defined in Sec. 2.6.1. Typical drop profiles are given in Fig. 2.3.

physical.

2.6.2 Zero-gravity Case ($G = 0$)

In the special case of no air jet, $J = 0$, the function V is monotonically increasing in R, and for all values of $V > 0$ there is a single stable and physical equilibrium solution.

Figure 2.2 shows J plotted against R for $V_0 = 1, 2$ and 3. Each curve has one zero at $R = (3V_0)^{1/2}$ (p) or $R = (8V_0)^{1/3}$ (a), and a maximum $J = J_m$ at $R = R_m$, where $J_m = 6/(5V_0)^{3/2}$ and $R_m = (5V_0)^{1/2}$ (p) or $J_m = 3/(4V_0)$ and $R_m = (16V_0)^{1/3}$ (a). For all values of V_0 we find that $J \to 0$ like $15/R^3$ (p) or $24/R^3$ (a) as $R \to \infty$. The left-hand part of each curve corresponds to stable and physical drop profiles like those numbered 1 and 2 in Fig. 2.3. At $R = R_m$ the solutions remain physical and look like profile 3 in Fig. 2.3 but become unstable. For $R > R_m$ the equilibrium solutions remain unstable and, as R increases, eventually become unphysical via $h = 0$ at the origin like

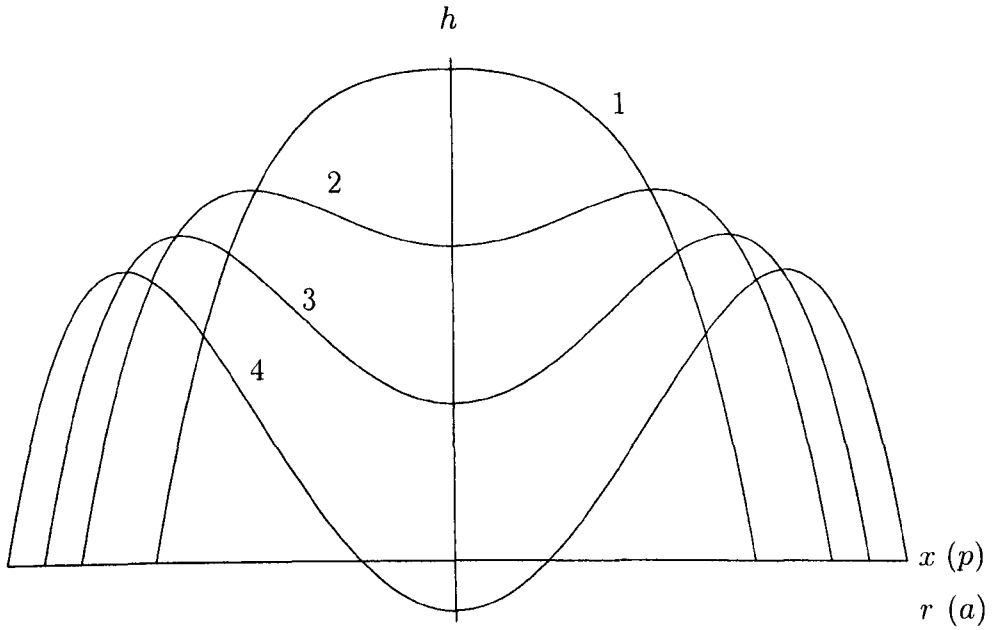

Figure 2.3: Typical drop profiles for various values of radius R for a drop in zero gravity. Drop profiles in the sessile drop case are qualitatively similar to those shown here.

profile 4 in Fig. 2.3, at $R = (15V_0)^{1/2}$, $J = 12/(15V_0)^{3/2}$ (p) or $R = (24V_0)^{1/3}$, $J = 2/(3V_0)$ (a). In the planar case the drop profile changes from having one turning point to three (that is, changes from one like profile 1 to one like profile 2 in Fig. 2.3) when R increases through $R = R_m$, while in the axisymmetric case this change occurs inside the interval of stable and physical drop profiles at $R = (12V_0)^{1/3} < R_m$, $J = 2/(3V_0)$. The width of the interval of R values corresponding to stable and physical profiles increases as V_0 is increased, and for any value of J in the range $0 \leq J \leq J_m$ there exists a unique stable and physical equilibrium solution; however, J_m decreases with increasing V_0.

Figure 2.4 shows V plotted against R for $J_0 = 1, 2$ and 3, which can be interpreted in a similar way to Fig. 2.2. Each curve has two zeros, at $R = 0$ and $R = (15/J_0)^{1/3}$ (p) or $R = (24/J_0)^{1/3}$ (a), and a maximum $V = V_m$ at $R = R_m$, where $V_m = (6/J_0)^{2/3}/5$ and $R_m = (6/J_0)^{1/3}$ (p) or $V_m = 3/(4J_0)$ and $R_m = (12/J_0)^{1/3}$ (a). For all values of J_0, we find that $V \to 0$ like $R^2/3$ (p) or $R^3/8$ (a) as $R \to 0$. Again the left-hand part of each curve corresponds to

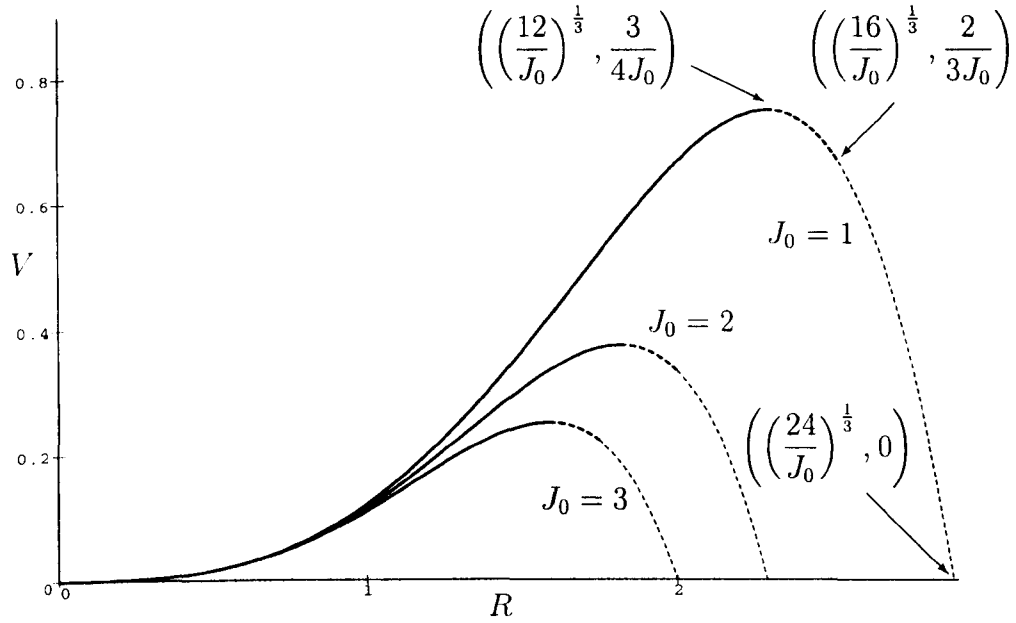

Figure 2.4: Plot of volume V against radius R for an axisymmetric drop in the case of zero gravity for $J_0 = 1, 2, 3$. The line styles are defined in Sec. 2.6.1. Typical drop profiles are given in Fig. 2.3.

stable and physical drop profiles. At $R = R_{\rm m}$ the solutions remain physical but become unstable, while for $R > R_m$ the equilibrium solutions remain unstable and, as R increases, eventually become unphysical via $h = 0$ at the origin at $R = (12/J_0)^{1/3}$, $V = (12/J_0)^{2/3}/15$ (p) or $R = (16/J_0)^{1/3}$, $V = 2/(3J_0)$ (a). In the planar case the drop profile changes from having one turning point to three when R increases through $R = R_{\rm m}$, while in the axisymmetric case this change occurs inside the interval of stable and physical drop profiles at $R = (8/J_0)^{1/3} < R_{\rm m}$, $V = 2/(3J_0)$. In this case the width of the interval of R values corresponding to stable and physical profiles decreases as J_0 is increased, and for any value of V in the range $0 < V \leq V_{\rm m}$ there exists a unique stable and physical equilibrium solution; however, $V_{\rm m}$ decreases for increasing J_0.

Figure 2.5 plots contact angle θ, given by Eq. (2.25), against radius R in the case $V_0 = 0.4$ and $J_0 = 1$. The thick line corresponds to physical solutions and the thin line corresponds to unphysical solutions. The points of intersection with the horizontal line $\theta = 1$ correspond to equilibrium solutions at $R \approx 1.5608$

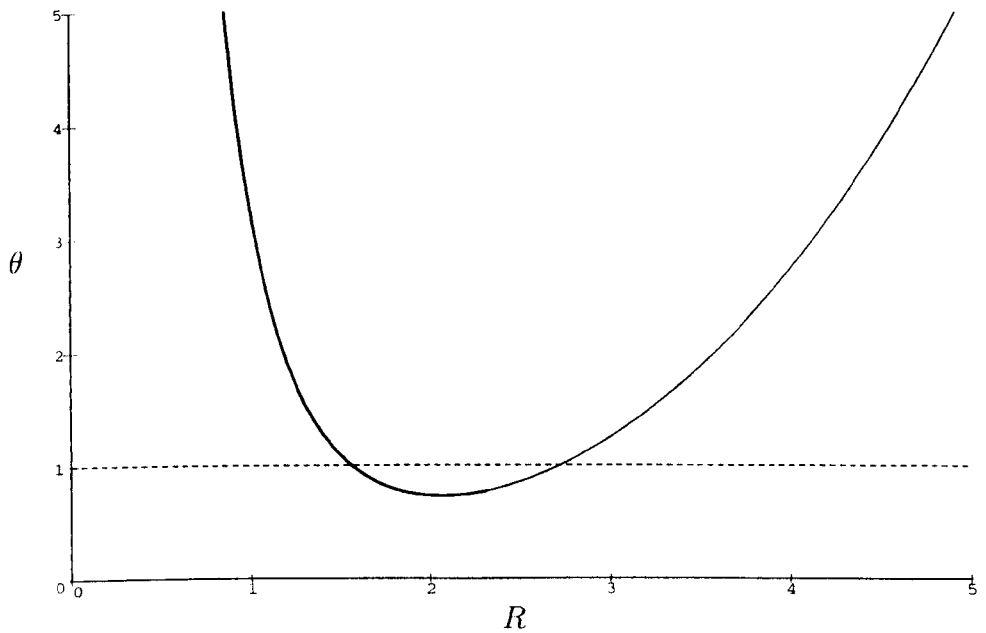

Figure 2.5: Plot of contact angle θ against radius R for an axisymmetric drop in the case of zero gravity, with $V_0 = 0.4$ and $J_0 = 1$. The thick line corresponds to physical solutions; the thin line corresponds to unphysical solutions. The points of intersection with the horizontal line $\theta = 1$ correspond to equilibrium solutions.

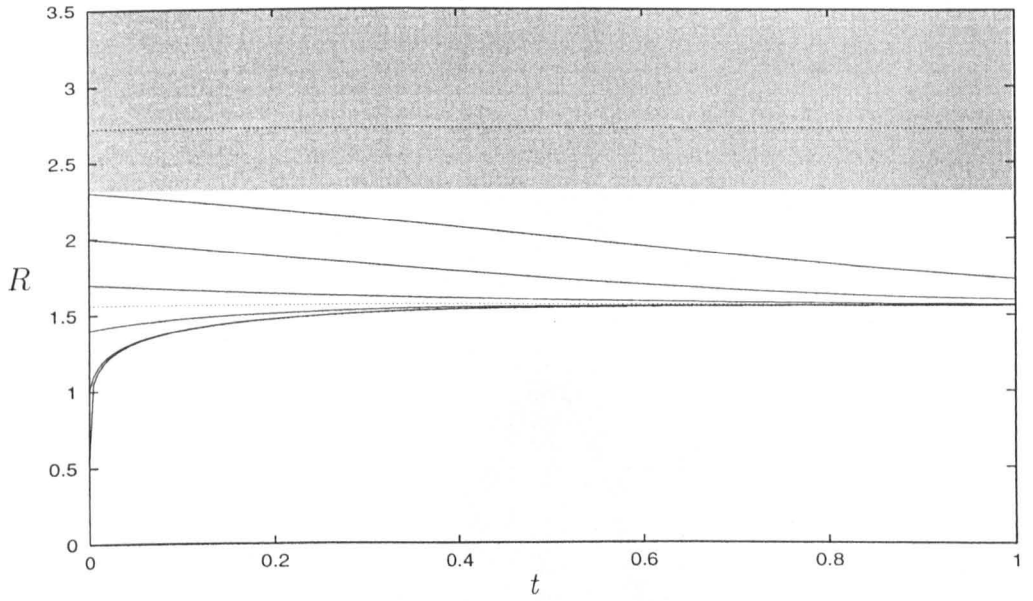

Figure 2.6: Examples of the evolution of drop radius $R(t)$ for an axisymmetric drop in the case of zero gravity when $V_0 = 0.4$ and $J_0 = 1$ obtained by solving Eq. (2.26) numerically in the case $F(\theta) = \theta^3 - 1$. The equilibrium values $R \approx 1.5608$ (stable) and $R \approx 2.7233$ (unstable) are indicated by horizontal dashed lines, and the shaded area denotes a region of unphysical solutions.

(stable) and $R \approx 2.7233$ (unstable). Figure 2.6 plots examples of the evolution of the radius R as a function of time t obtained by numerically solving Eq. (2.26) in the particular case $F(\theta) = \theta^3 - 1$. Detailed analysis in the vicinity of the contact line (see, for example, Hocking [21], Oron *et al.* [45] and Duffy & Wilson [8]) motivates this specific choice of Tanner Law. The shaded area denotes a region of unphysical solutions; our computations exclude this region. Evidently for all the initial conditions shown in Fig. 2.6 the drop evolves to the stable equilibrium solution with $R \approx 1.5608$. Figures 2.7 and 2.8 show the evolution of the drop profile in the cases $R(0) = 0.5$ and $R(0) = 2.3$ respectively; in both figures the stable equilibrium solution with $R \approx 1.5608$ is shown with a dashed curve. (Note that Figs. 2.7 and 2.8 use different vertical scales, for clarity.)

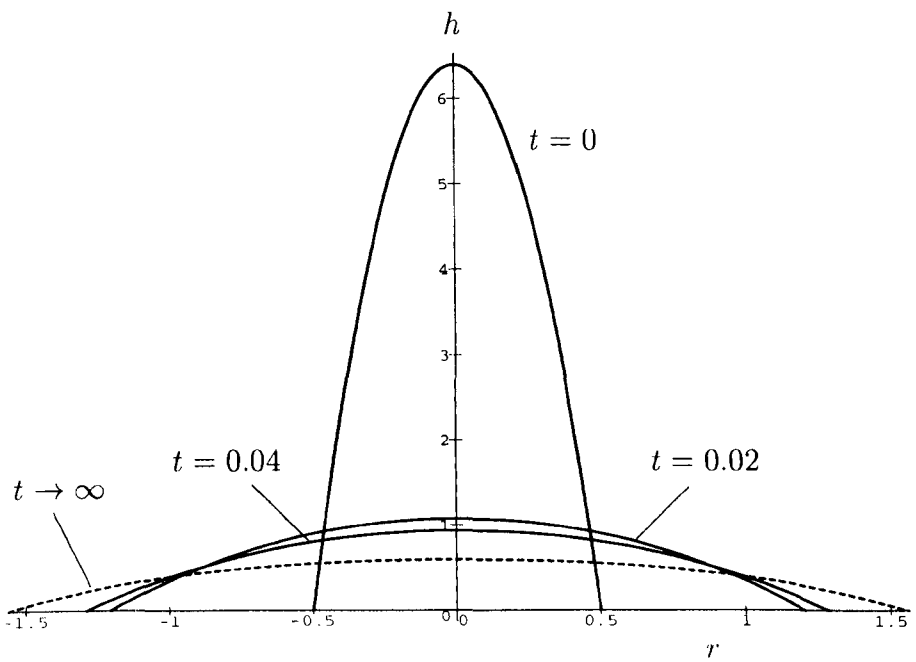

Figure 2.7: Evolution of a quasi-static drop profile for an axisymmetric drop in the case of zero gravity when $V_0 = 0.4$, $J_0 = 1$, with the initial condition $R(0) = 0.5$. The dashed curve corresponds to the stable equilibrium solution $R \approx 1.5608$.

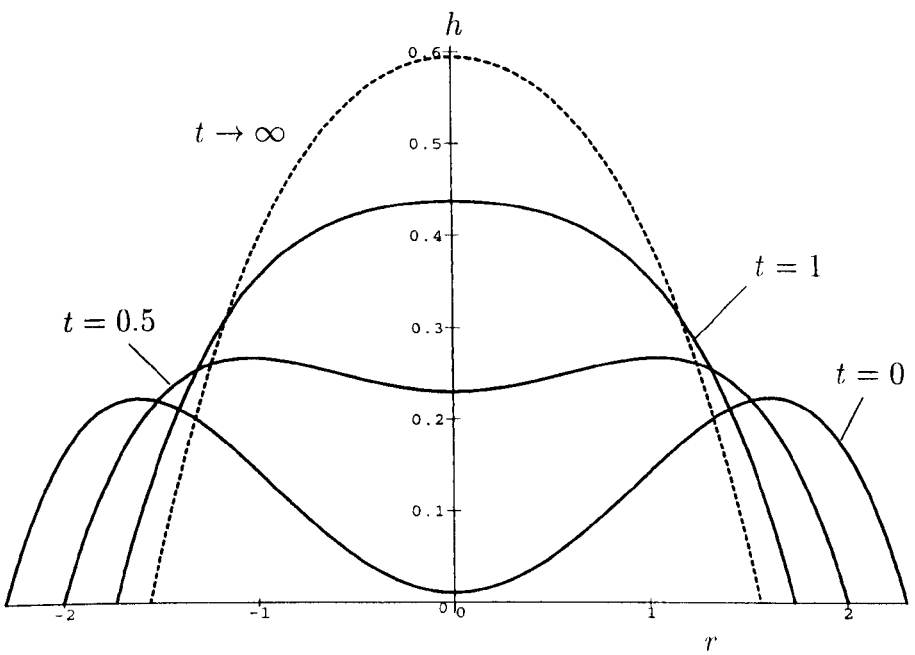

Figure 2.8: Evolution of a quasi-static drop profile for an axisymmetric drop in the case of zero gravity when $V_0 = 0.4$, $J_0 = 1$, with the initial condition $R(0) = 2.3$. The dashed curve corresponds to the stable equilibrium solution $R \approx 1.5608$.

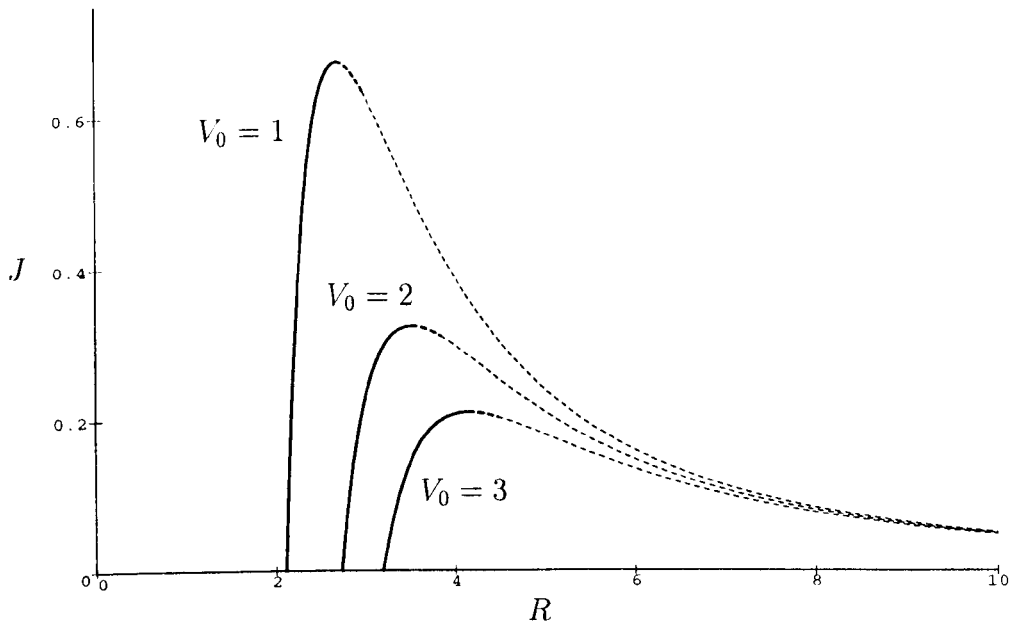

Figure 2.9: Plot of jet strength J against radius R for an axisymmetric sessile drop for $V_0 = 1, 2, 3$. The line styles are defined in Sec. 2.6.1. Drop profiles in this case are qualitatively similar to those shown in Fig. 2.3.

2.6.3 Sessile Case ($G = 1$)

In the special case $J = 0$ the function V is monotonically increasing in R and for all values of $V > 0$ there is a single stable and physical equilibrium solution, just as in the zero-gravity case.

Figures 2.9 and 2.10 show J plotted against R for $V_0 = 1, 2$ and 3 and V plotted against R for $J_0 = 1, 2$ and 3. The qualitative behaviour of the solutions in this case is the same as that of the zero-gravity solutions and so, for the sake of brevity, the details are not repeated here.

2.6.4 Pendent Case ($G = i$)

In the special case $J = 0$ the function V is monotonically increasing in R between each of its infinitely many vertical asymptotes, and for every value of $V > 0$ there are infinitely many stable equilibrium profiles. However, only the solution on the first branch is physically realisable and so again there is only a single stable

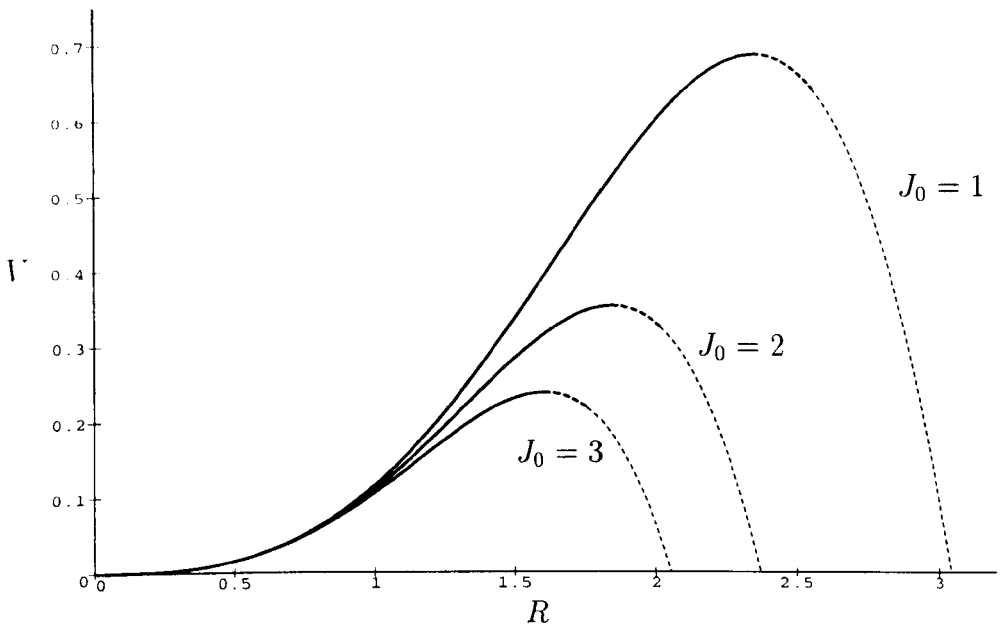

Figure 2.10: Plot of volume V against radius R for an axisymmetric sessile drop for $J_0 = 1, 2, 3$. The line styles are defined in Sec. 2.6.1. Drop profiles in this case are qualitatively similar to those shown in Fig. 2.3.

and physical equilibrium solution for all values of $V > 0$. Unlike the previous two cases the introduction of non-zero J changes this situation qualitatively.

Figure 2.11 shows J plotted against R for $V_0 = 20$, $V_0 = V_c \approx 32.4642$ and $V_0 = 40$. The branches in Fig. 2.11 can be classified as one of three types:

- J1 - a branch with a maximum/minimum "kink",
- J2 - a branch with a maximum turning point,
- J3 - a monotonically decreasing function.

The only order in which these branches can appear on each plot is J1 then J2 followed by J3 as R increases. Each branch lies between the vertical asymptotes of J, which occur at values of R satisfying

$$\begin{cases} \tan R = \dfrac{3R}{3 - R^2}, & (p) \\ \dfrac{J_1(R)}{J_0(R)} = \dfrac{4R}{8 - R^2}, & (a) \end{cases} \tag{2.35}$$

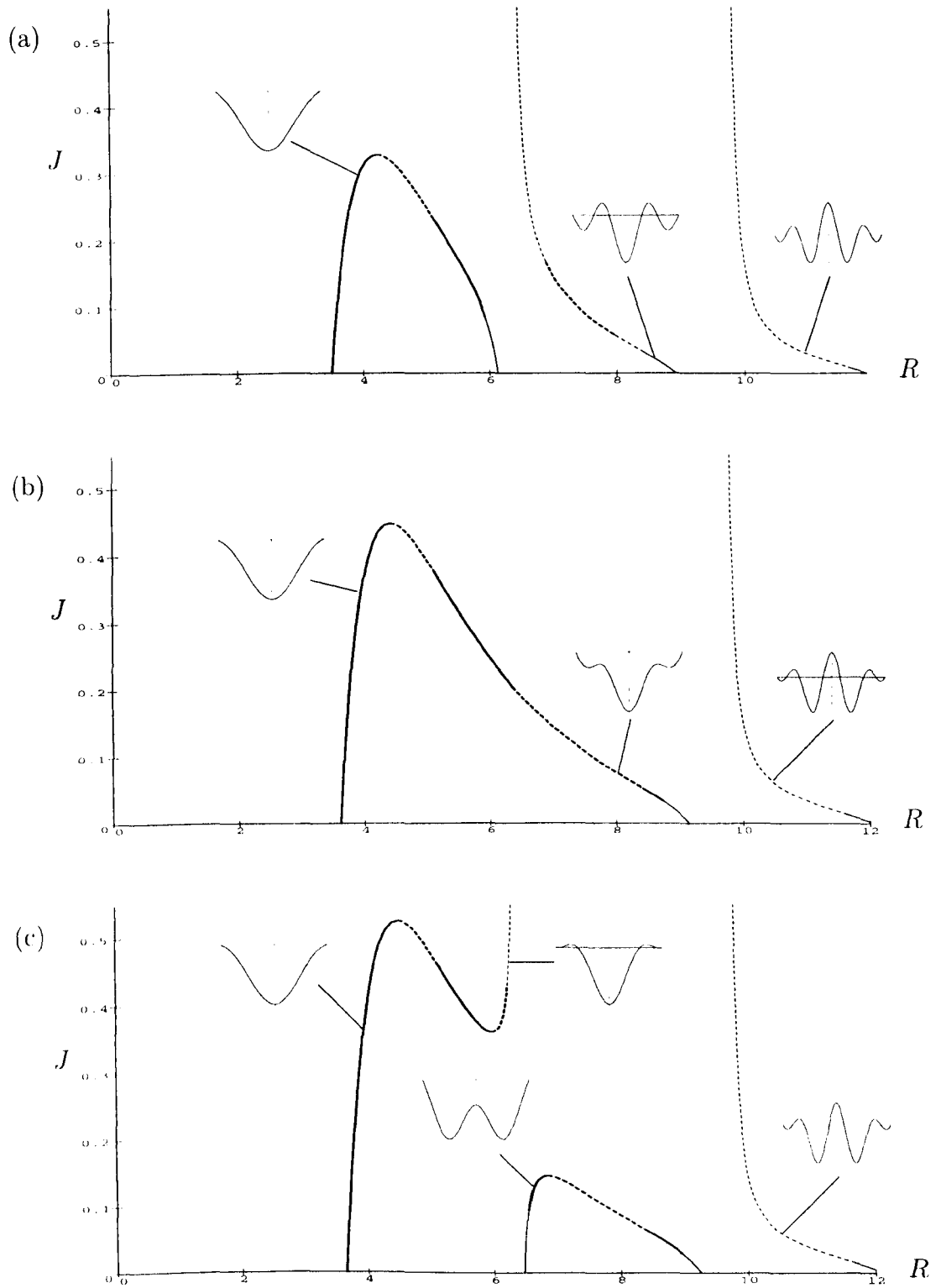

Figure 2.11: Plot of jet strength J against radius R for an axisymmetric pendent drop when (a) $V_0 = 20 < V_c$, (b) $V_0 = V_c \approx 32.4642$ and (c) $V_0 = 40 > V_c$. The line styles are defined in Sec. 2.6.1.

which are independent of V_0, and where $J_0(R)$ and $J_1(R)$ are Bessel functions of the first kind. The number of J1 branches depends on the value of V_0, whereas there is only ever one J2 branch and an infinite number of J3 branches extending to the right. The special value $V = V_c$ corresponds to the case where one of the vertical asymptotes of J disappears, leaving a continuous curve connecting what were two adjacent branches for $V \neq V_c$. Equating the numerator and denominator of Eq. (2.28) to zero we find that V_c satisfies

$$\begin{cases} \tan(3V_c)^{\frac{1}{2}} = \dfrac{(3V_c)^{\frac{1}{2}}}{1 - V_c}, & (p) \\ \dfrac{J_1(2V_c^{\frac{1}{3}})}{J_0(2V_c^{\frac{1}{3}})} = \dfrac{2V_c^{\frac{1}{3}}}{2 - V_c^{\frac{2}{3}}}. & (a) \end{cases} \tag{2.36}$$

The values of R at which there is marginal stability are the solutions of Eq. (2.34) and, as the plots in Fig. 2.11 show, stable and physical solutions can occur on other branches as well as the first. Note that some of the regions of stability are relatively small. For example, in Fig. 2.11(a) there is a small stable but unphysical region between $R \approx 11.6198$ and $R \approx 11.9047$. As the drop profiles in Fig. 2.11 show, unlike in the zero-gravity and sessile cases, the solutions can become unphysical via $h = 0$ at locations other than the origin.

Figure 2.11(a) with $V_0 = 20$ shows one J2 branch and the first two of the J3 branches. In Fig. 2.11(b) V_0 is increased to V_c; the vertical asymptote at $R \approx 6.3802$ vanishes and a J2 branch and a J3 branch connect to form a critical J2 branch. In Fig. 2.11(c) V_0 is increased to 40 and the figure shows a J1, a J2 and the first J3 branch. Note that the number of J1 branches increases as V_0 increases, with the maximum/minimum kink occurring at smaller values of J as R increases. The drop profiles usually (but not always) have an increasing number of maxima and minima as R increases. For example, in Fig. 2.11(a) the drop profile on the J2 branch has one turning point and the drop profile on the J3 branch immediately to the right has five, whereas in Fig. 2.11(c) the drop profile on the J1 branch for $R \approx 6.3$ has five turning points (two very close to $r = \pm R$) while the drop profile on the J2 branch immediately to the right has only three. For any given value of J there are finitely many (at least one and

possibly more) stable and physical profiles, and there is a maximum value of $J = J_m$ above which no physical and stable solutions exist.

Figure 2.12 shows V plotted against R for $J_0 = 0.12$, $J_0 = J_c \approx 0.1425$ and $J_0 = 0.16$, which can be described in a similar way to Fig. 2.11. The branches in Fig. 2.12 can be classified as one of three types:

- V1 - a monotonically increasing function,
- V2 - a branch with a maximum turning point,
- V3 - a branch with a minimum/maximum "kink".

The only order in which these branches can appear on each plot is V1 then V2 followed by V3 as R increases. Each branch lies between the vertical asymptotes of V, which occur at values of R satisfying

$$\begin{cases} \sin R = 0, & (p) \\ J_1(R) = 0, & (a) \end{cases} \tag{2.37}$$

which are independent of J_0. The number of V1 branches depends on the value of J_0, whereas there is only ever one V2 branch and an infinite number of V3 branches extending to the right. The special value $J = J_c$ corresponds to the case where one of the vertical asymptotes of V disappears leaving a continuous curve connecting what were two adjacent branches for $J \neq J_c$. Equating the numerator and denominator of Eq. (2.27) to zero we find that J_c satisfies

$$\begin{cases} \sin\left(\dfrac{1}{J_c}\right) = 0, & (p) \\ J_1\left(\dfrac{1}{J_c}\right) = 0. & (a) \end{cases} \tag{2.38}$$

The values of R at which there is marginal stability are the solutions of Eq. (2.33) and, unlike in the case $J = 0$, stable and physical solutions can occur on branches other than just the first. Note that again some of the regions are relatively small. For example, in Fig. 2.12(a) there is a small unstable but physical region between $R \approx 4.9684$ and $R \approx 5.1356$. Once again the solutions can become unphysical via $h = 0$ at locations other than the origin.

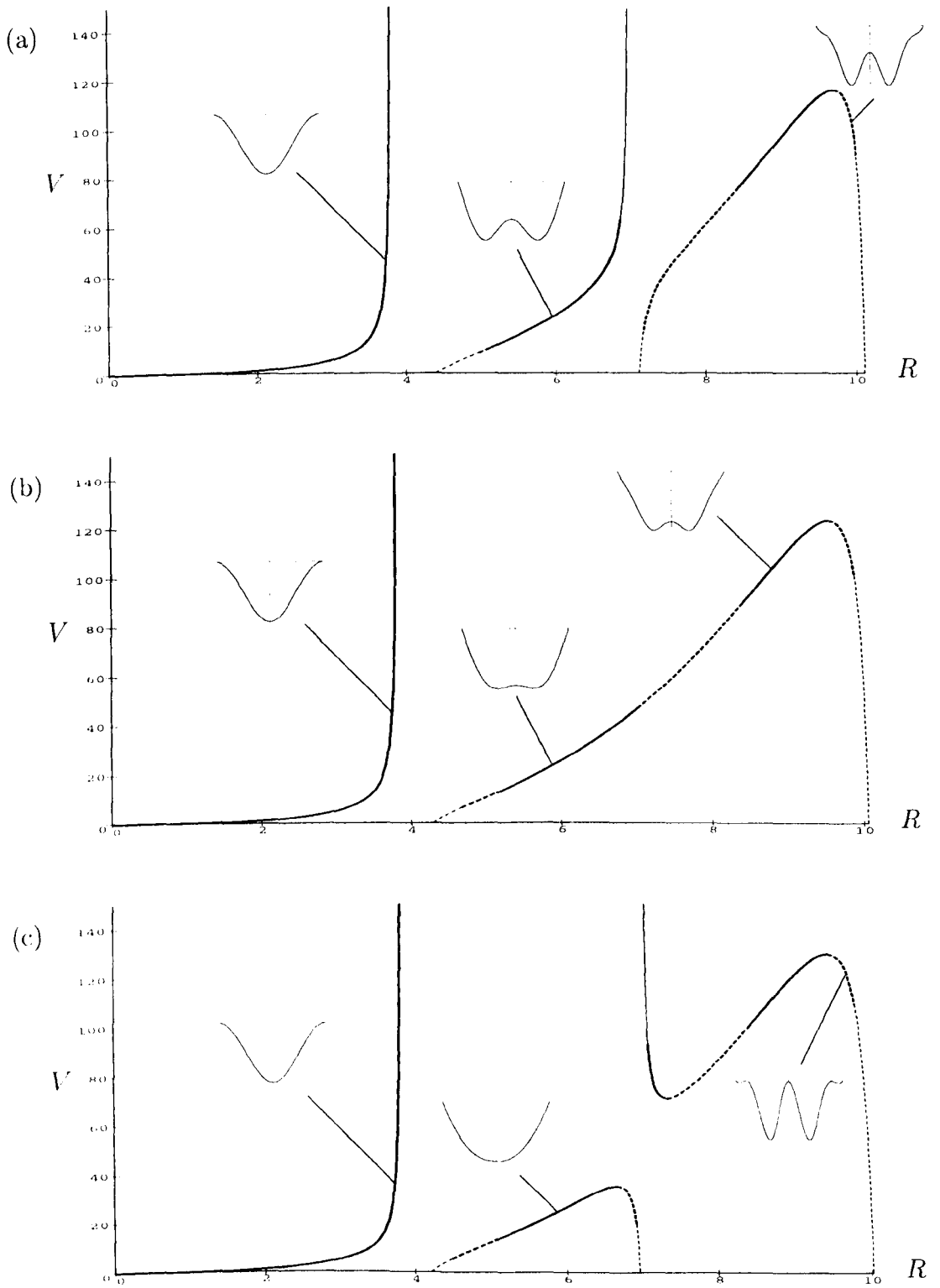

Figure 2.12: Plot of volume V against radius R for an axisymmetric pendent drop when (a) $J_0 = 0.12 < J_c$, (b) $J_0 = J_c \approx 0.1425$ and (c) $J_0 = 0.16 > J_c$. The line styles are defined in Sec. 2.6.1.

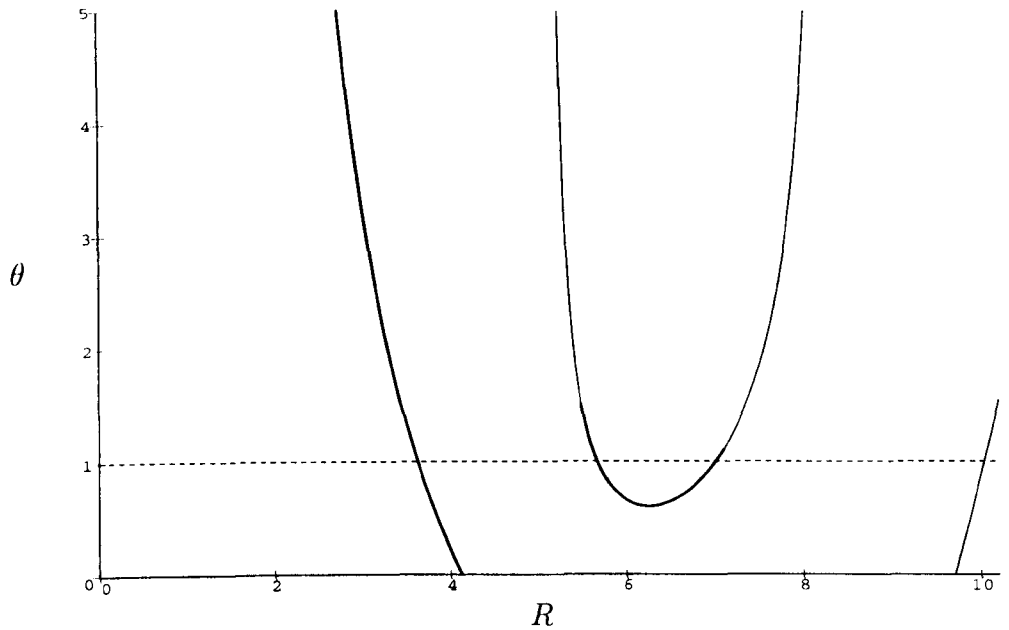

Figure 2.13: Plot of contact angle θ against radius R for an axisymmetric pendent drop, with $V_0 = 20$ and $J_0 = 0.16$. The thick lines correspond to physical solutions; the thin lines correspond to unphysical solutions. The points of intersection with the horizontal line $\theta = 1$ correspond to equilibrium solutions.

Figure 2.12(a) with $J_0 = 0.12$ shows two V1 branches and a V2 branch with V3 branches extending infinitely to the right thereafter. In Fig. 2.12(b) J_0 is increased to J_c; the vertical asymptote $R = R_c \approx 7.0156$ vanishes, and a V1 branch and a V2 branch connect to form a critical V2 branch. In Fig. 2.12(c) J_0 is increased to 0.16 and the figure shows a V1, a V2 and the first V3 branch. Note that in this case the number of V1 branches decreases as J_0 increases while the minimum/maximum kink on the V3 branches occurs at ever larger values of V as R increases. As previously, the drop profiles usually (but not always) have an increasing number of maxima and minima as R increases. In this case for any given value of V there are finitely many (at least one and possibly more) stable and physical profiles, but there is no upper limit on the value of V for physical and stable solutions to exist.

Figure 2.13 plots contact angle θ against radius R in the case $V_0 = 20$ and $J_0 = 0.16$. The thick lines correspond to physical solutions and the thin

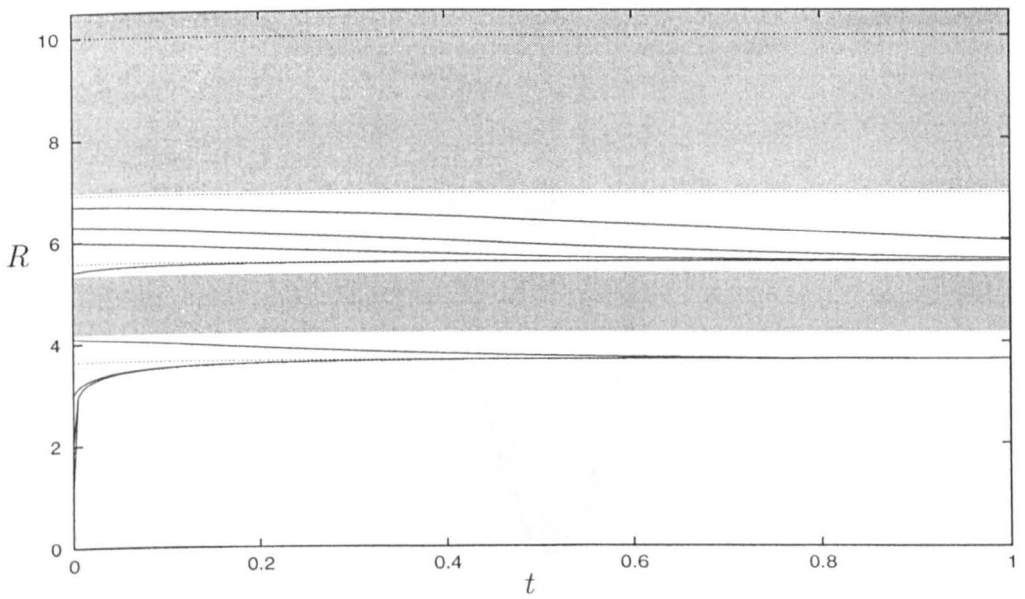

Figure 2.14: Examples of the evolution of drop radius $R(t)$ for an axisymmetric pendent drop when $V_0 = 20$ and $J_0 = 0.16$, obtained by solving Eq. (2.26) numerically in the case $F(\theta) = \theta^3 - 1$. The equilibrium values $R \approx 3.6524$ (stable), $R \approx 5.5740$ (stable), $R \approx 6.9149$ (unstable) and $R \approx 10.0041$ (unstable) are indicated by horizontal dashed lines, and the shaded areas denote regions of unphysical solutions.

lines correspond to unphysical solutions. The points of intersection with the horizontal line $\theta = 1$ correspond to equilibrium solutions at $R \approx 3.6524$ (stable), $R \approx 5.5740$ (stable) $R \approx 6.9149$ (unstable) and $R \approx 10.0041$ (unstable). Figure 2.14 plots examples of the evolution of the radius R as a function of time t obtained by solving Eq. (2.26) numerically in the particular case $F(\theta) = \theta^3 - 1$. The shaded areas denote regions of unphysical solutions; our computations again exclude these regions. Figures 2.15 and 2.16 show the evolution of the drop profile in the cases $R(0) = 1$ and $R(0) = 6.8$ respectively; in both figures the appropriate stable equilibrium solution is shown with a dashed curve.

Figure 2.17 plots contact angle θ against radius R for $V_0 = 20$ in the special case $J_0 = J_c \approx 0.1425$ and shows that, despite what the corresponding plot of V against R shown in Fig. 2.12(b) might suggest, the dynamics in this case are qualitatively similar to those when $J_0 = 0.12$ and $J_0 = 0.16$. Note, however,

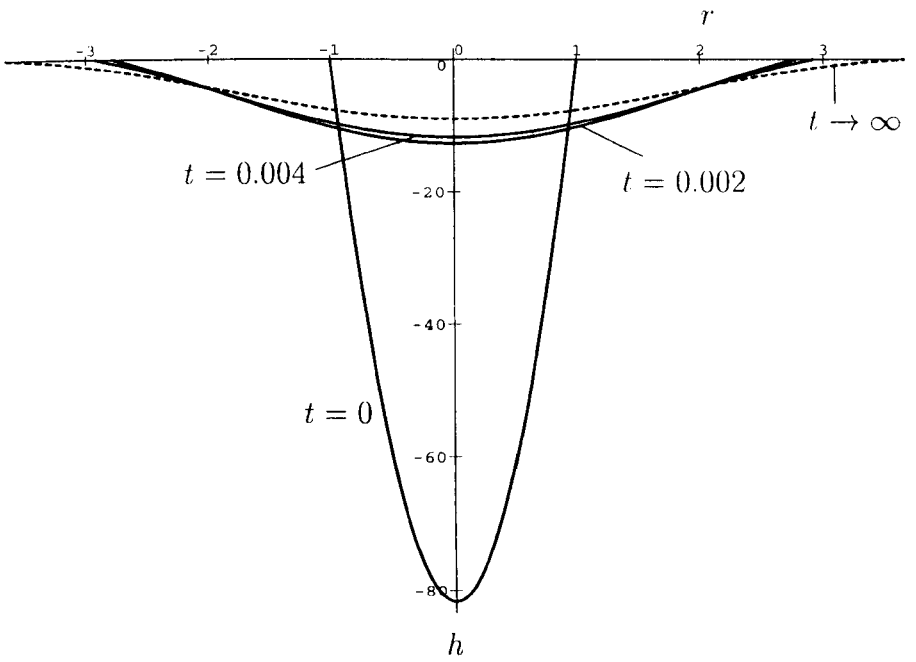

Figure 2.15: Evolution of a quasi-static drop profile for an axisymmetric pendent drop when $V_0 = 20$, $J_0 = 0.16$, with the initial condition $R(0) = 1$. The dashed curve corresponds to the stable equilibrium solution $R \approx 3.6524$.

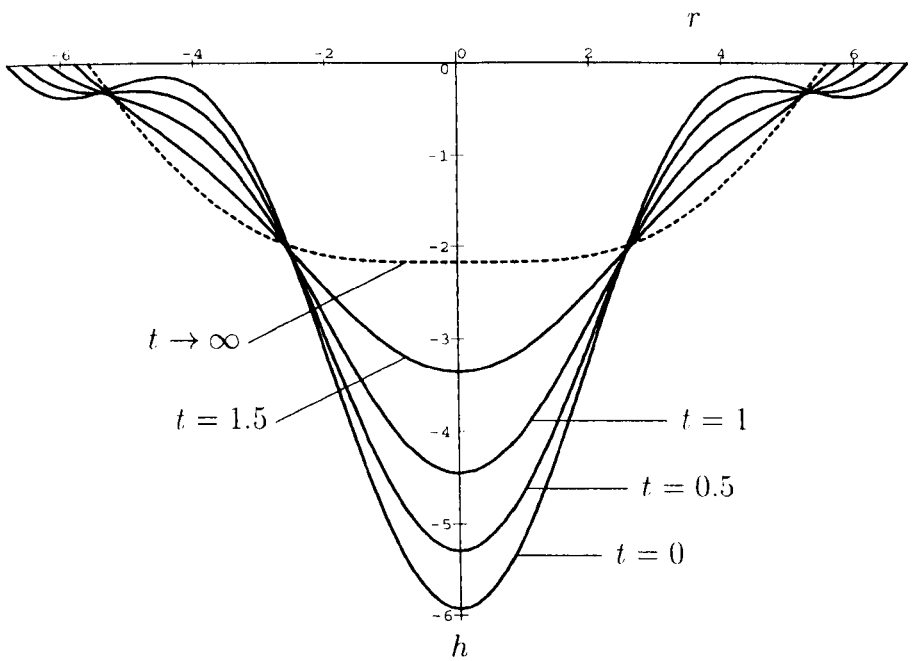

Figure 2.16: Evolution of a quasi-static drop profile for an axisymmetric pendent drop when $V_0 = 20$, $J_0 = 0.16$, with the initial condition $R(0) = 6.8$. The dashed curve corresponds to the stable equilibrium solution $R \approx 5.5740$.

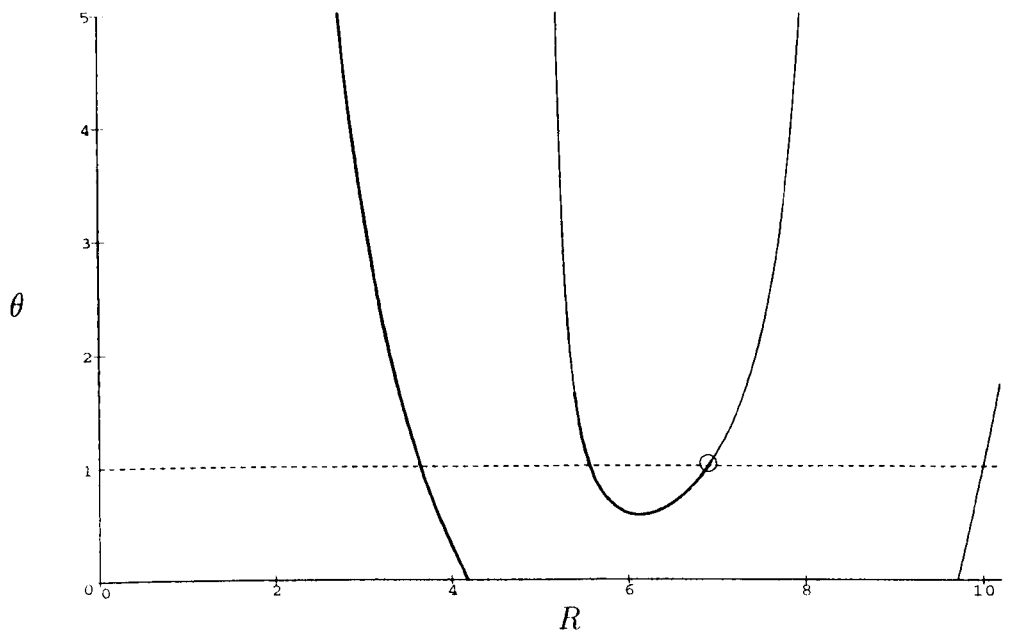

Figure 2.17: Plot of contact angle θ against radius R for an axisymmetric pendent drop, with $V_0 = 20$ and $J_0 = J_c \approx 0.1425$. The thick lines correspond to physical solutions; the thin lines correspond to unphysical solutions. The points of intersection with the horizontal line $\theta = 1$ correspond to equilibrium solutions. The open circle (○) indicates that there is no solution with the correct volume at this special value of $R = R_c \approx 7.0156$.

that when $J_0 = J_c$ there is, in general, no equilibrium solution with the correct volume with $R = R_c \approx 7.0156$, the value of R corresponding to the vertical asymptote of $V(R)$ that disappears when $J_0 = J_c$. Corresponding behaviour is observed when $V_0 = V_c$.

In all parts of Figs. 2.11 and 2.12 (but not the corresponding figures in the zero-gravity and sessile cases) there are evidently changes in stability at points other than the local extrema. Inspection of Eqs. (2.33) and (2.34) shows that these "unusual" changes of stability occur at points $R = R^*$ where $S(R^*) = 0$, and inspection of the definition of $S(R)$ in Eq. (2.23) shows that this is indeed possible only in the pendent case. Since $|\theta| \to \infty$ as these points are approached the lubrication approximation and possibly also (depending on the specific form of $F(\theta)$) the quasi-static approximation fail in the immediate vicinity of these points.

In the special case $J_0 = J_c$ (Fig. 2.12(b)) stability also changes at the point $R = R_c$ (the value of R corresponding to the vertical asymptote of $V(R)$ that disappears). Corresponding behaviour is again observed when $V_0 = V_c$.

Chapter 3

Quasi-static Analysis of an Annular Drop

3.1 Introduction

As we have already seen, in many cases the solutions discussed thus far can fail to be physically-realisable via $h(0) = 0$. (Indeed, this is the only way that the solutions become unphysical when $G^2 \geq 0$.) It is therefore natural to examine next the possibility of solutions that have a dry patch with no fluid near the origin. In an axisymmetic geometry these solutions take the form of an annular ring of fluid centered on $r = 0$, while in a planar geometry they take the form of two disconnected drops which are symmetric about $x = 0$. In order to keep the algebra manageable we shall concentrate solely in this Chapter on the special case of zero gravity, that is, the case $G = 0$.

3.2 Problem Formulation

Clearly the major difference between the annular solutions discussed in this Chapter and the non-annular solutions discussed previously is that the former have two contact lines and hence two contact angles. The outer contact line is located at $x = R_2(t)$ (p) or $r = R_2(t)$ (a) and the inner one at $x = R_1(t)$ (p) or $r = R_1(t)$ (a). The corresponding contact angles are denoted by $\theta = \theta(t)$ and $\phi = \phi(t)$. Physically-realisable solutions satisfy $\theta \geq 0$, $\phi \geq 0$ and $R_2 > R_1$, and

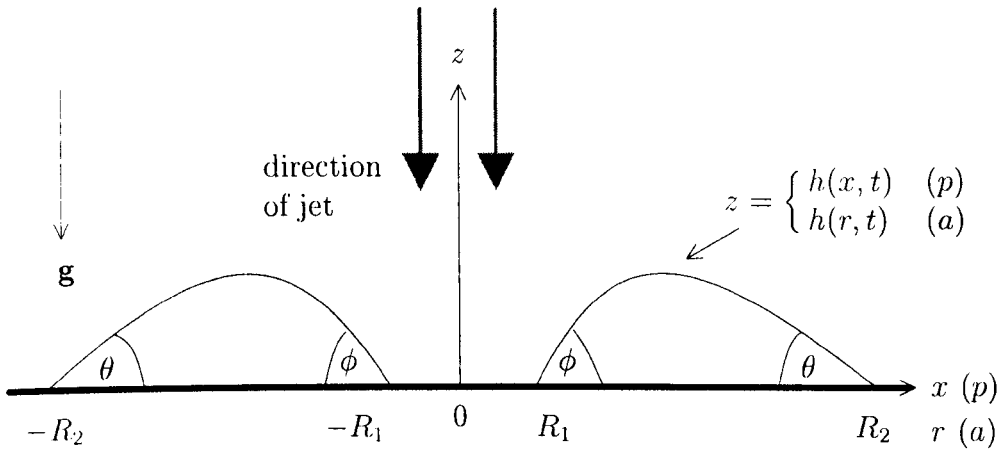

Figure 3.1: Geometry of the annular problem.

in equilibrium $\theta = \theta_0$ and $\phi = \phi_0$. The geometry of the problem is summarised in Fig. 3.1.

Choosing the same scalings for the variables as before (see Chapter 2, Sec. 2.2) means that we can set $\theta_0 = 1$ without loss of generality. Furthermore, since we are considering only the case $G = 0$ we can, without loss of generality, set either $J = 1$ or $V = 1$; for ease of comparison with the earlier results and for clarity we shall retain both V and J in what follows and then present results for both $J = 1$ and $V = 1$. Hereafter scaled variables are used unless stated otherwise.

3.3 Quasi-static Motion

For quasi-static motion with $Q = 0$ at leading order in C the equation for h is given again by Eq. (2.18) with $G = 0$, namely

$$\begin{cases} h_{xxx} + Jx = 0, & (p) \\ \left(h_{rr} + \dfrac{h_r}{r}\right)_r + Jr = 0. & (a) \end{cases} \tag{3.1}$$

Since there are now two moving contact lines we need to replace Eq. (2.12) by two Tanner Laws relating the speed of each contact line to its contact angle. For these we use the forms

$$(R_1)_t = -F_1(\phi), \tag{3.2}$$

$$(R_2)_t = F_2(\theta), \tag{3.3}$$

where the empirically-determined functions F_1 and F_2 satisfy $F_1(\phi_0) = F_2(1) = 0$. Analogously to the non-annular case in Chapter 2 we assume that F_1 and F_2 are monotonically-increasing locally near $\phi = \phi_0$ and $\theta = 1$ respectively, and so their first non-zero derivatives at these points will be positive and of odd order. The boundary conditions for Eq. (3.1) are

$$h(R_1, t) = 0, \tag{3.4}$$

$$h(R_2, t) = 0, \tag{3.5}$$

$$\begin{cases} h_x(R_2, t) = -\theta, & (p) \\ h_r(R_2, t) = -\theta, & (a) \end{cases} \tag{3.6}$$

$$\begin{cases} h_x(R_1, t) = \phi, & (p) \\ h_r(R_1, t) = \phi. & (a) \end{cases} \tag{3.7}$$

Solving Eq. (3.1) subject to Eqs. (3.4) – (3.6) yields

$$h = \theta f(\cdot, R_1, R_2) + J g(\cdot, R_1, R_2), \tag{3.8}$$

where the symbol "$\cdot$" again denotes x (p) or r (a) and the functions $f(\cdot, R_1, R_2)$ and $g(\cdot, R_1, R_2)$ are given by

$$\begin{cases} f(x, R_1, R_2) = \dfrac{(R_2 - x)(R_1 - x)}{R_1 - R_2}, & (p) \\ f(r, R_1, R_2) = \Big[R_2(R_2^2 - r^2)\ln R_1 - R_2(R_1^2 - r^2)\ln R_2 \\ \qquad\qquad - R_2(R_2^2 - R_1^2)\ln r\Big]\Big[R_2^2 - R_1^2 + 2R_2^2\ln(R_1/R_2)\Big]^{-1}, & (a) \end{cases} \tag{3.9}$$

$$\begin{cases} g(x, R_1, R_2) = \dfrac{1}{24}(R_2 - x)^2(R_1 - x)(R_1 + 2R_2 + x), & (p) \\ g(r, R_1, R_2) = \dfrac{1}{32}\Big[-2R_2^2(R_2^2 - r^2)^2\ln R_1 + 2R_2^2(R_2^2 - R_1^2)^2\ln r \\ \qquad + 2R_2^2(R_1^2 - r^2)(2R_2^2 - R_1^2 - r^2)\ln R_2 \\ \qquad - (R_1^2 - r^2)(R_2^2 - r^2)(R_2^2 - R_1^2)\Big] \\ \qquad \times \Big[R_2^2 - R_1^2 + 2R_2^2\ln(R_1/R_2)\Big]^{-1}. & (a) \end{cases} \tag{3.10}$$

The volume of this annular drop is given by

$$\begin{cases} 2V = 2\int_{R_1}^{R_2} h\,\mathrm{d}x, & (p) \\ 2\pi V = 2\pi\int_{R_1}^{R_2} hr\,\mathrm{d}r, & (a) \end{cases} \tag{3.11}$$

and so

$$V = \theta S(R_1, R_2) + JT(R_1, R_2), \tag{3.12}$$

where the functions $S = S(R_1, R_2)$ and $T = T(R_1, R_2)$ are given by

$$S(R_1, R_2) = \begin{cases} \dfrac{(R_2 - R_1)^2}{6}, & (p) \\ \dfrac{R_2(R_2^4 - R_1^4)\ln(R_1/R_2) + R_2(R_2^2 - R_1^2)^2}{4[R_2^2 - R_1^2 + 2R_2^2\ln(R_1/R_2)]}, & (a) \end{cases} \tag{3.13}$$

$$T(R_1, R_2) = \begin{cases} -\dfrac{(2R_1 + 3R_2)(R_2 - R_1)^4}{360}, & (p) \\ -\Big[4R_2^2(2R_1^2 + R_2^2)(R_2^2 - R_1^2)^2\ln(R_1/R_2) \\ +(R_1^2 + 5R_2^2)(R_2^2 - R_1^2)^3\Big] \\ \times\Big[384[R_2^2 - R_1^2 + 2R_2^2\ln(R_1/R_2)]\Big]^{-1}. & (a) \end{cases} \tag{3.14}$$

We can trivially re-write Eq. (3.12) as an explicit expression for θ for constant $V = V_0$ and $J = J_0$ in the form

$$\theta = \frac{V_0 - J_0 T(R_1, R_2)}{S(R_1, R_2)}. \tag{3.15}$$

The remaining boundary condition Eq. (3.7) yields an explicit expression for ϕ for constant $V = V_0$ and $J = J_0$ in the form

$$\phi = \begin{cases} \theta - \dfrac{J_0}{12}(R_2 + R_1)(R_2 - R_1)^2, & (p) \\ \Big[(R_2^2 - R_1^2)\left[R_2^4 - R_1^4 + 4R_1^2R_2^2\ln(R_1/R_2)\right]J_0 \\ -16R_2\left[R_2^2 - R_1^2 + 2R_1^2\ln(R_1/R_2)\right]\theta\Big] \\ \times\Big[16R_1[R_2^2 - R_1^2 + 2R_2^2\ln(R_1/R_2)]\Big]^{-1}. & (a) \end{cases} \tag{3.16}$$

Evidently in equilibrium ($\theta = 1$, $\phi = \phi_0$) annular solutions are impossible in the planar case if $\phi_0 \geq 1$; in particular, there is no non-trivial annular solution in

the case in which the contact angles are equal, that is, when $\phi_0 = 1$. Indeed, from Eq. (3.16)(p) it is clear that equilibrium annular solutions with equal inner and outer contact angles are possible only when $J_0 = 0$. The explanation for this is that in the planar case the "annulus" comprises two disconnected drops, symmetrically placed about $x = 0$, each of them subject to an off-centre jet; such a drop cannot be in equilibrium when $\theta_0 = \phi_0$ since the net external force on it is non-zero (because the resultant force due to the jet has a non-zero x-component, whereas the x-components of the surface-tension forces at the two contact lines cancel each other out exactly when $\theta_0 = \phi_0$). As we shall see there is no similar restriction on the value of ϕ_0 for annular solutions in the axisymmetric case.

In the planar case Eqs. (3.15) and (3.16) yield

$$\theta = \frac{360V_0 + (3R_2 + 2R_1)(R_2 - R_1)^4 J_0}{60(R_2 - R_1)^2}, \tag{3.17}$$

$$\phi = \frac{360V_0 - (2R_2 + 3R_1)(R_2 - R_1)^4 J_0}{60(R_2 - R_1)^2}, \tag{3.18}$$

while in the axisymmetric case they yield

$$\theta = \frac{\tau_1(R_1, R_2)J_0 + \tau_2(R_1, R_2)V_0}{96R_2(R_2^2 - R_1^2)[R_2^2 - R_1^2 + (R_1^2 + R_2^2)\ln(R_1/R_2)]}, \tag{3.19}$$

$$\phi = \frac{\tau_3(R_1, R_2)J_0 + \tau_4(R_1, R_2)V_0}{96R_1(R_2^2 - R_1^2)[R_2^2 - R_1^2 + (R_1^2 + R_2^2)\ln(R_1/R_2)]}, \tag{3.20}$$

where the functions τ_1, τ_2, τ_3 and τ_4 are given by

$$\left.\begin{aligned}
\tau_1(R_1, R_2) &= (R_2^2 - R_1^2)^2[5R_2^4 - 4R_1^2R_2^2 - R_1^4 + (4R_2^4 + 8R_1^2R_2^2)\ln(R_1/R_2)], \\
\tau_2(R_1, R_2) &= 384[R_2^2 - R_1^2 + 2R_2^2\ln(R_1/R_2)], \\
\tau_3(R_1, R_2) &= (R_2^2 - R_1^2)^2[R_2^4 + 4R_1^2R_2^2 - 5R_1^4 + (4R_1^4 + 8R_2^2R_1^2)\ln(R_1/R_2)], \\
\tau_4(R_1, R_2) &= -384[R_2^2 - R_1^2 + 2R_1^2\ln(R_1/R_2)].
\end{aligned}\right\} \tag{3.21}$$

Note that in the limit $R_1, R_2 \to \infty$ for fixed $R_2 - R_1 > 0$ we recover the previous results for the planar case, while in the limit $R_2 \to \infty$ for fixed R_1 we obtain the special case of a hole in an unbounded fluid film corresponding to the thin-film limit of the zero-gravity version of the problem studied by Taylor & Michael [51] and Wilson & Duffy [59].

3.4 Stability Analysis

Proceeding as in Chapter 2 we can determine the stability of an equilibrium drop for which $\theta = 1$, $\phi = \phi_0$, $R_1 = R_1^0$ and $R_2 = R_2^0$ to small perturbations in R_1 and R_2 by writing $R_1(t) = R_1^0 + R_1^1(t)$ and $R_2(t) = R_2^0 + R_2^1(t)$ and expanding Eqs. (3.2) and (3.3) for small R_1^1 and R_2^1 to yield

$$\begin{cases} (R_1^1)_t = -\dfrac{M}{m!}(\alpha_1 R_1^1 + \alpha_2 R_2^1)^m, \\ (R_2^1)_t = \dfrac{N}{n!}(\beta_1 R_1^1 + \beta_2 R_2^1)^n, \end{cases} \tag{3.22}$$

where $M = \mathrm{d}^m F_1(\phi)/\mathrm{d}\phi^m|_{\phi=\phi_0} > 0$ $(m = 1, 3, 5, \ldots)$ is the first non-zero derivative of $F_1(\phi)$ evaluated at $\phi = \phi_0$, and $N = \mathrm{d}^n F_2(\theta)/\mathrm{d}\theta^n|_{\theta=1} > 0$ $(n = 1, 3, 5, \ldots)$ is the first non-zero derivative of $F_2(\theta)$ evaluated at $\theta = 1$, and the constants α_1, α_2, β_1 and β_2 are given by $\alpha_i = \partial\phi/\partial R_i$ and $\beta_i = \partial\theta/\partial R_i$ evaluated at $R_1 = R_1^0$ and $R_2 = R_2^0$ for $i = 1, 2$. As before, we shall immediately drop the clumsy superscript notation and in the remainder of this section we shall denote R_1^0 and R_2^0 simply by R_1 and R_2. Unfortunately, unlike in the previous Chapter, we have been unable to obtain either the general solution of Eq. (3.22) or general criteria for the growth or decay of the solutions of Eq. (3.22) as $t \to \infty$. However, we can make progress in the special case $m = n = 1$ when the system given by Eq. (3.22) is linear and has eigenvalues

$$\lambda_\pm = \frac{N\beta_2 - M\alpha_1 \pm \left[(M\alpha_1 + N\beta_2)^2 - 4MN\alpha_2\beta_1\right]^{\frac{1}{2}}}{2}, \tag{3.23}$$

and so stability of the equilibrium solution is determined by the sign of $\mathrm{Re}(\lambda_+)$. Hereafter we shall take $M = N$ for simplicity.

3.4.1 Planar Case

In the planar case we can use Eqs. (3.17) and (3.18) to evaluate the α_i and β_i for $i = 1, 2$ and hence obtain simple explicit expressions for $\lambda_\pm/M$, namely

$$\frac{\lambda_+}{M} = \frac{J_0}{12}(R_2 - R_1)^2, \tag{3.24}$$

$$\frac{\lambda_-}{M} = \frac{J_0}{20}(R_2 - R_1)^2 - \frac{24V_0}{(R_2 - R_1)^3}. \tag{3.25}$$

Note that λ_+ is independent of V_0 in this case. We can deduce immediately that the eigenvalues $\lambda_\pm$ are purely real and, since $\lambda_+ > 0$ for all values of V_0 and J_0, that all planar annular solutions are unconditionally unstable.

3.4.2 Axisymmetric Case

In the axisymmetric case we can use Eqs. (3.19), (3.20) and (3.21) to evaluate the α_i and β_i for $i = 1, 2$ and hence obtain the corresponding expressions for $\lambda_\pm$. However, these expressions are now very lengthy and considerably more effort is required to establish the sign of $\mathrm{Re}(\lambda_+)$ than in the planar case. To simplify the subsequent algebra we write $R_1 = \eta$, $R_2 = c\eta$ and so the requirements that $R_1 > 0$, $R_2 > 0$ and $R_2 > R_1$ mean that $\eta > 0$ and $c > 1$.

Firstly, we demonstrate that $\lambda_\pm$ are purely real. If we denote the discriminant of $\lambda_\pm/M$ by $D_1 = (\alpha_1 + \beta_2)^2 - 4\alpha_2\beta_1$ then by setting $J_0 = 1$ without loss of generality we can write

$$D_1 = \frac{1}{\eta^8}\left[\nu_1(c)V_0^2 + \eta^6\nu_2(c)V_0 + \eta^{12}\nu_3(c)\right], \tag{3.26}$$

where ν_1, ν_2 and ν_3 are known functions of c, not reproduced here for brevity. Evidently D_1 can change sign only when V_0 satisfies

$$\nu_1(c)V_0^2 + \eta^6\nu_2(c)V_0 + \eta^{12}\nu_3(c) = 0. \tag{3.27}$$

Thus the existence or non-existence of real solutions for V_0 depends on the sign of the discriminant D_2 of Eq. (3.27), which is given by

$$\begin{aligned} D_2 = \eta^{12}(c^4 - 4c^2\ln c - 1)^2\Big[&(7c^2-1)(c^2-7)(c^2-1)^3 \\ &- 3(c^2+1)(c^4-22c^2+1)(c^2-1)^2\ln c - 8c^2(c^2-1)(5c^4-4c^2+5)(\ln c)^2 \\ &- 48c^4(c^2+1)(\ln c)^3\Big]\Big[c^4(c^2-1)^2(c^2\ln c - c^2 + \ln c + 1)^5\Big]^{-1}. \end{aligned} \tag{3.28}$$

Note that $D_2 \sim O(-(c-1)^{-2})$ as $c \to 1^+$ and $D_2 \sim O(-(\ln c)^{-4})$ as $c \to \infty$. Evidently the sign of D_2 depends only on c and not on η. Figure 3.2 shows a plot of D_2 as a function of $c > 1$ and clearly demonstrates that $D_2 < 0$ for all values of c. Hence there are no real roots of Eq. (3.27) and therefore D_1 is of

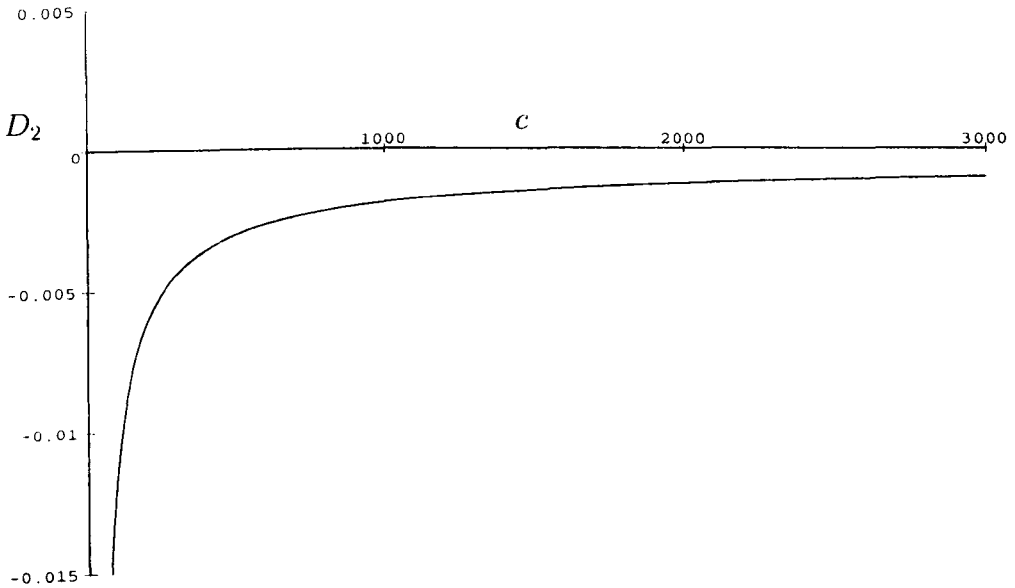

Figure 3.2: Plot of D_2 defined in Eq. (3.28) as a function of c.

one sign. A simple evaluation of D_1 with values $V_0 > 0$ and $c > 1$ shows that it is always positive and hence the eigenvalues $\lambda_\pm$ are always real.

Secondly, we demonstrate that $\lambda_+ > 0$. From Eq. (3.23) we can write

$$\frac{\lambda_\pm}{M} = \gamma_1(c)\eta^2 + \frac{\gamma_2(c)}{\eta} \pm \left[\gamma_3(c)\eta^4 + \gamma_4(c)\eta + \frac{\gamma_5(c)}{\eta^2}\right]^{\frac{1}{2}}, \tag{3.29}$$

where the γ_i, $i = 1, \ldots, 5$ are known functions of c, not reproduced here for brevity. Typical values of $\lambda_\pm/M$ are plotted as functions of η for a range of values of c in Fig. 3.3. Of most importance are the minimum value of λ_+/M (denoted by $\lambda_{\min}$) and the maximum value of λ_-/M (denoted by $\lambda_{\max}$) and numerically calculated values of these quantities are shown in Fig. 3.4. Note that $\lambda_{\min} \sim 2^{-1/3}$ and $\lambda_{\max} \sim 2^{-1/3}$ as $c \to \infty$ while $\lambda_{\min} \sim O((c-1)^{5/3})$ and $\lambda_{\max} \sim O(-(c-1)^{5/3})$ as $c \to 1^+$. As Fig. 3.4 shows, $\lambda_{\max} < 0$ when $1 < c < c_{\text{crit}}$ and $\lambda_{\max} > 0$ when $c > c_{\text{crit}}$, where $c = c_{\text{crit}} \simeq 31.05$ is the single real root of the equation

$$(c^2 - 4c + 1)\ln c - 3c^2 + 3 = 0. \tag{3.30}$$

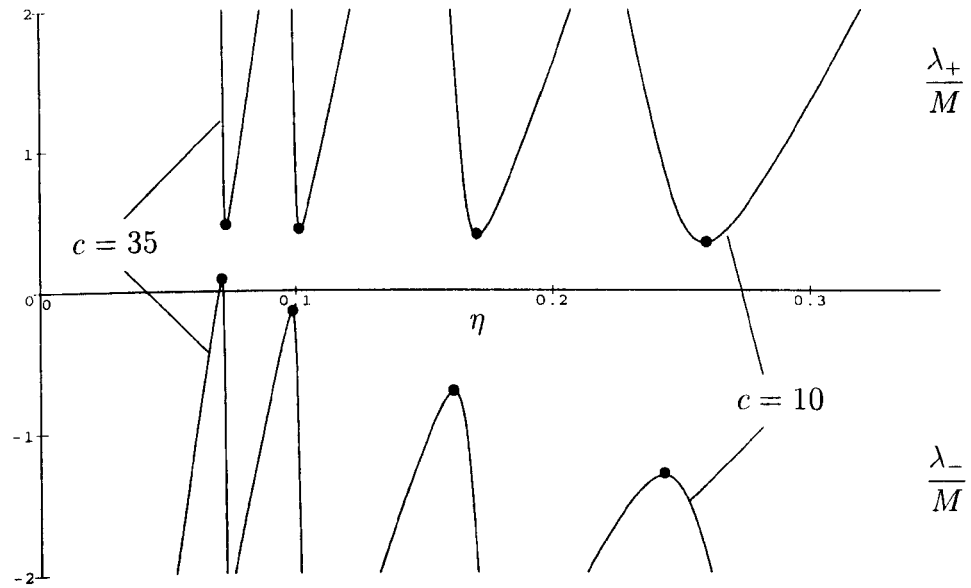

Figure 3.3: Plot of λ_+/M and λ_-/M for $c = 10$, 15, 25 and 35. The dots (•) denote the points corresponding to $\lambda_{\min}$ and $\lambda_{\max}$.

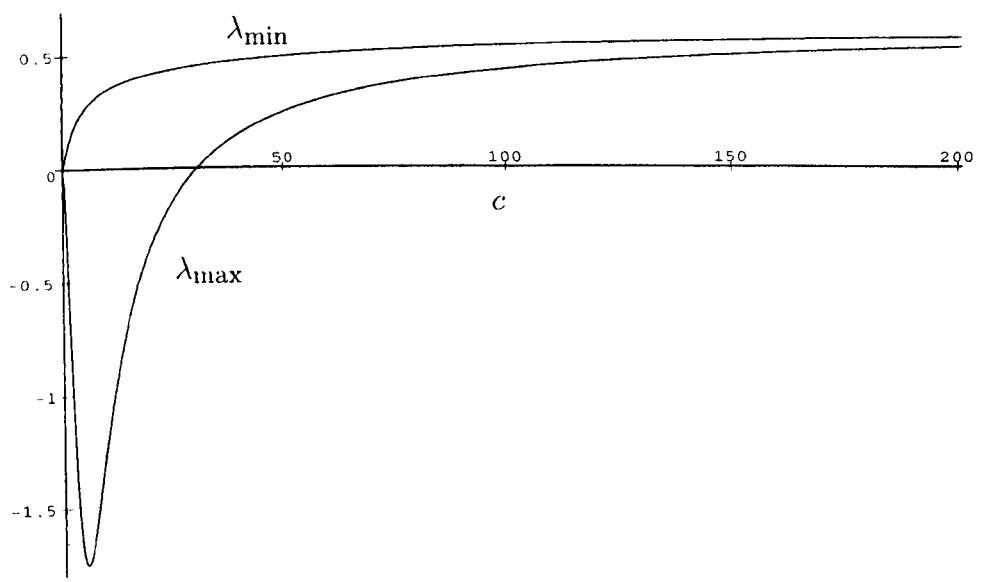

Figure 3.4: Plot of $\lambda_{\min}$ (upper curve) and $\lambda_{\max}$ (lower curve) as a function of c.

More significantly, Fig. 3.4 also shows that $\lambda_{\min} > 0$ for all $c > 1$ and so $\lambda_+ \geq \lambda_{\min} > 0$ for $c > 1$; therefore all axisymmetric annular solutions are unconditionally unstable, just as in the planar case.

3.5 Results

3.5.1 Explanation of Figures

In Figs. 3.5–3.8 we present plots of jet strength J against outer radius R_2 for fixed volume $V_0 = 1$, and volume V against outer radius R_2 for fixed jet strength $J_0 = 1$. Note that all the annular solutions depicted in Figs. 3.5–3.8 are physically realisable and unstable, and therefore represented by thick dashed lines. Each of these plots contain annular solutions for various inner contact angles ϕ_0. Since $\theta_0 = 1$, values of ϕ_0 other than $\phi_0 = 1$ require that either the system exhibits contact-angle hysteresis (with $\theta_r \leq \theta_0 \leq \theta_a$, where θ_r and θ_a are the receding and advancing contact angles respectively) or, more artificially, that the substrate be inhomogeneous with a change of physical properties somewhere in $R_1 < x < R_2$ (p) or $R_1 < r < R_2$ (a). The case $\phi_0 = 1$, however, requires no such conditions. In each plot, curve (A) corresponds to the physically-realisable non-annular solutions as discussed in Chapter 2 Sec. 2.6.2. In the planar case (Figs. 3.5 and 3.6) curve (B) corresponds to solutions with $R_1 = 0$, representing two contiguous drops, one in $-R_2 \leq x \leq 0$ and the other in $0 \leq x \leq R_2$. In the axisymmetric case, however, the only solution with $R_1 = 0$ occurs when $\phi_0 = 0$, and so there is no curve in Figs. 3.7 and 3.8 corresponding to curve (B) in Figs. 3.5 and 3.6. Figure 3.9 shows examples of the evolution of the radii R_1 and R_2 as functions of time in the axisymmetric case for particular choices of $F_1(\phi)$ and $F_2(\theta)$, while Figs. 3.10 and 3.11 show corresponding examples of the evolution of the profile of the annular drop. Unlike for the non-annular solutions described in Chapter 2 Sec. 2.6, the qualitative behaviour of the planar and axisymmetric annular solutions are quite different, and so in what follows we discuss these two cases separately.

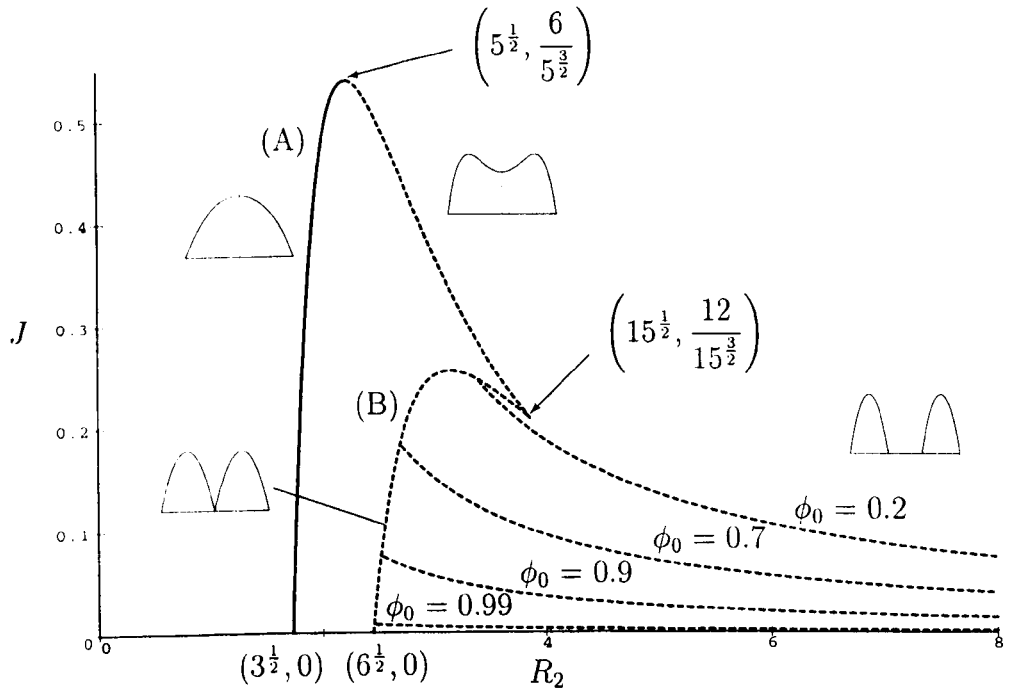

Figure 3.5: Plot of jet strength J against outer radius R_2 for a planar annular drop for $\phi_0 = 0.2$, 0.7, 0.9 and 0.99 when $V_0 = 1$ and $G = 0$. A solid, thick line represents stable and physical equilibrium solutions; a dashed, thick line represents unstable and physical solutions. Curve (A) corresponds to physically-realisable non-annular solutions and curve (B) corresponds to solutions for two physically-realisable contiguous drops.

3.5.2 Planar Case

Figure 3.5 shows a plot of J against R_2 when $V_0 = 1$ for inner contact angles $\phi_0 = 0.2$, 0.7, 0.9 and 0.99. In particular, Fig. 3.5 shows how each annular curve branches away from curve (B) at a different point. Note that, as previously indicated, there are no non-trivial annular solutions for $\phi_0 \geq 1$, and that as $\phi_0 \to 1^-$ the corresponding J against R_2 curve approaches the $J = 0$ axis. For all the annular curves $J \sim (1 - \phi_0^2)/2R_2$ as $R_2 \to \infty$.

Figure 3.6 shows a plot of V against R_2 when $J_0 = 1$ for inner contact angles $\phi_0 = 0.2$, 0.7, 0.9 and 0.99, and again shows how each annular curve branches away from curve (B) at a different point. As $\phi_0 \to 1^-$ the corresponding V against R_2 curve approaches the $V = 0$ axis. For all the annular curves $V \sim (1 - \phi_0^2)/2R_2$ as $R_2 \to \infty$.

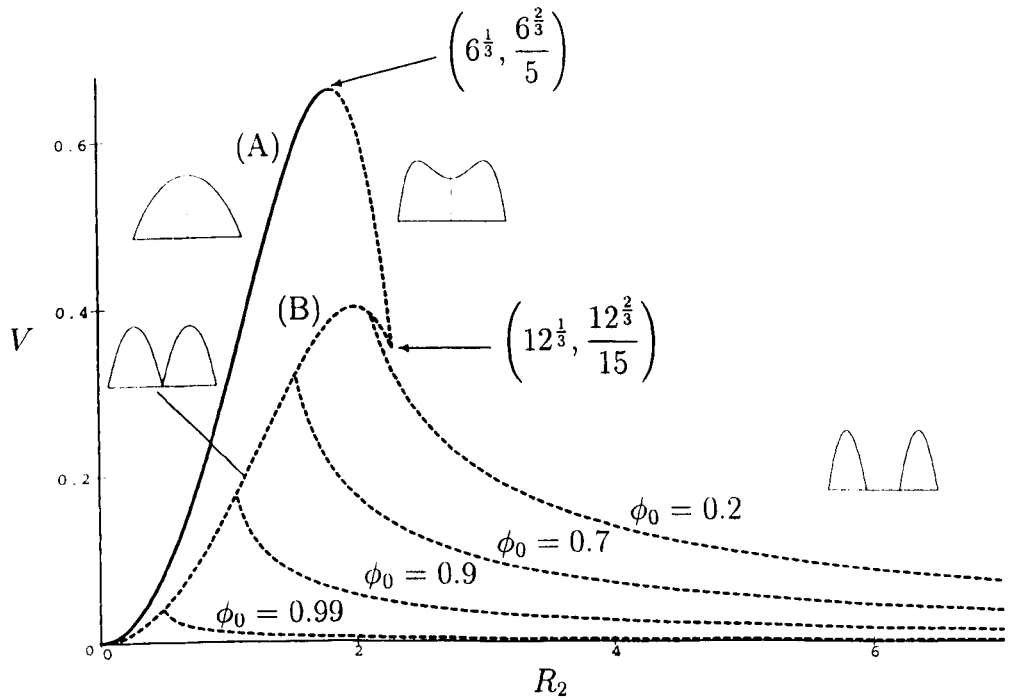

Figure 3.6: Plot of volume V against outer radius R_2 for a planar annular drop for $\phi_0 = 0.2$, 0.7, 0.9 and 0.99 when $J_0 = 1$ and $G = 0$. A solid, thick line represents stable and physical equilibrium solutions; a dashed, thick line represents unstable and physical solutions. Curve (A) corresponds to physically-realisable non-annular solutions and curve (B) corresponds to solutions for two physically-realisable contiguous drops.

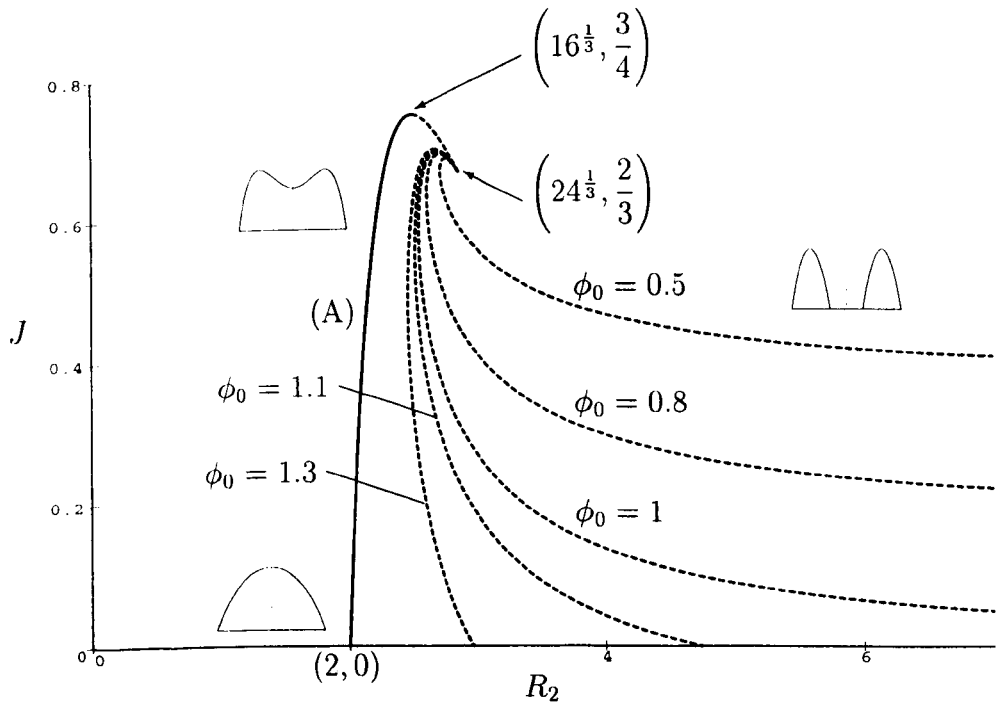

Figure 3.7: Plot of jet strength J against outer radius R_2 for an axisymmetric annular drop for $\phi_0 = 0.5$, 0.8, 1, 1.1 and 1.3 when $V_0 = 1$ and $G = 0$. A solid, thick line represents stable and physical equilibrium solutions; a dashed, thick line represents unstable and physical solutions. Curve (A) corresponds to physically-realisable non-annular solutions.

3.5.3 Axisymmetric Case

Figure 3.7 shows a plot of J against R_2 when $V_0 = 1$ for inner contact angles $\phi_0 = 0.5$, 0.8, 1, 1.1 and 1.3, and shows how all the annular curves branch away from the non-annular curve (A) at the single point $R_2 = 24^{1/3}$ and $J = 2/3$ where the non-annular solutions fail to be physical via $h(0) = 0$. Unlike in the planar case, annular solutions are now possible for all values of $\phi_0 \geq 0$. Whatever the value of ϕ_0 we have $J \to (1 - \phi_0^2)/2$ as $R_2 \to \infty$, and so only those curves for $0 \leq \phi_0 \leq 1$ approach a non-negative limiting value of J as $R_2 \to \infty$; curves for $\phi_0 > 1$ cross the $J = 0$ axis at a finite value of $R_2 > 0$.

Figure 3.8 shows a plot of V against R_2 when $J_0 = 1$ for inner contact angles $\phi_0 = 0.7$, 0.9, 1, 1.02, 1.1 and 1.3, and again shows how all the annular curves branch away from the non-annular curve (A) at the single point $R_2 = 16^{1/3}$ and $V = 2/3$ where the non-annular solutions fail to be physical via $h(0) = 0$. Figure

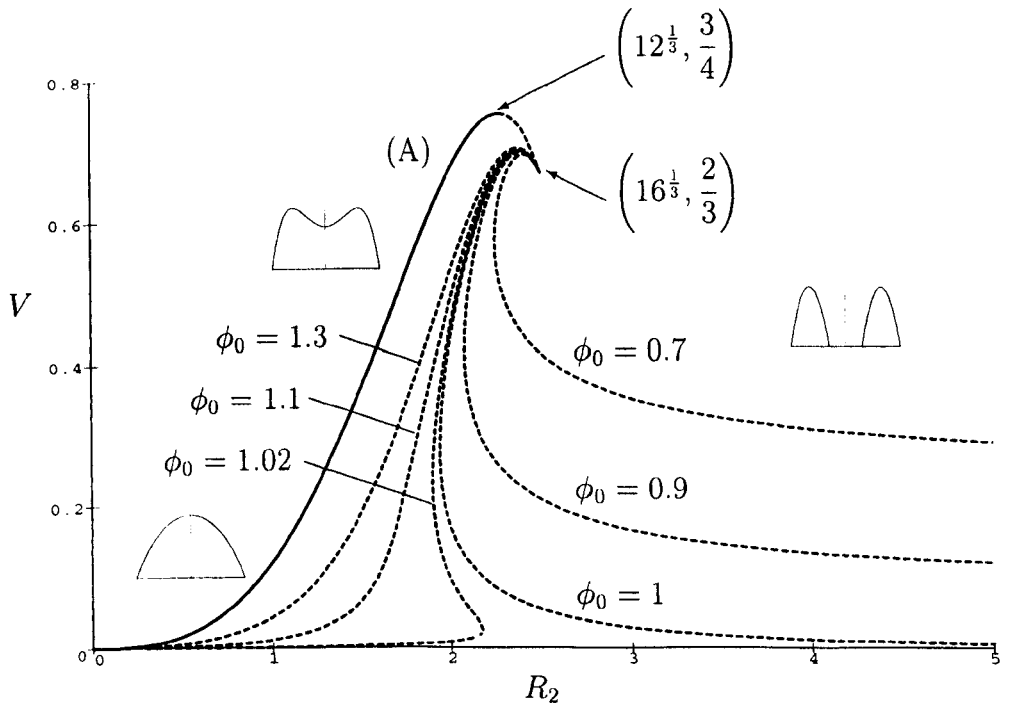

Figure 3.8: Plot of volume V against outer radius R_2 for an axisymmetric annular drop for $\phi_0 = 0.7$, 0.9, 1, 1.02, 1.1 and 1.3 when $J_0 = 1$ and $G = 0$. A solid, thick line represents stable and physical equilibrium solutions; a dashed, thick line represents unstable and physical solutions. Curve (A) corresponds to physically-realisable non-annular solutions.

3.8 also shows that the curves corresponding to $0 \leq \phi_0 \leq 1$ and $\phi_0 > 1$ have qualitatively different behaviour. When $0 \leq \phi_0 \leq 1$ we have $V \to (1 - \phi_0^2)/2$ as $R_2 \to \infty$, and hence these curves approach a non-negative limiting value of V as $R_2 \to \infty$. On the other hand, when $\phi_0 > 1$ we have

$$V \sim \frac{(1 - A^2)^2 + (1 - A^4) \ln A}{4(1 - A^2 + 2 \ln A)} R_2^3 \tag{3.31}$$

as $R_2 \to 0$, where the unique value of A depends on the value of ϕ_0 via the equation

$$\frac{1 - A^2 + 2A^2 \ln A}{A(1 - A^2 + 2 \ln A)} + \phi_0 = 0. \tag{3.32}$$

Figure 3.9 plots examples of the evolution of the inner radius R_1 and the outer radius R_2 as functions of time t obtained by numerically solving Eqs. (3.2) and (3.3) in the particular case $F_1(\phi) = \phi^3 - 1$ and $F_2(\theta) = \theta^3 - 1$ (i.e. equal equilibrium contact angles corresponding to $M = N = 3$) for $J_0 = 1$ and $V_0 = 0.1696$. The horizontal dashed lines correspond to the equilibrium values $R_1 \approx 1.1968$, $R_2 = 2$. The thick lines correspond to the curves with initial conditions $R_1(0) = 1$, $R_2(0) = 1.7$, the thin lines correspond to $R_1(0) = 1$, $R_2(0) = 2.2$, the dashed lines correspond to $R_1(0) = 1.3$, $R_2(0) = 1.7$ and the dot-dashed lines correspond to $R_1(0) = 1.3$, $R_2(0) = 2.2$. These examples illustrate what we found in all the cases that we investigated (with different initial conditions), namely that an annular drop 'closes' if the initial outer radius $R_2(0)$ is smaller than the equilibrium value and 'opens' if $R_2(0)$ is larger than the equilibrium value, irrespective of the value of the initial inner radius $R_1(0)$. This behaviour was also found in cases with different values of the inner equilibrium contact angle ϕ_0. Figures 3.10 and 3.11 show the evolution of the annular drop profile in the cases $R_1(0) = 1.3$, $R_2(0) = 1.7$ and $R_1(0) = 1.3$, $R_2(0) = 2.2$ respectively, and show how the annular drop with initial outer radius smaller than the equilibrium value 'closes' and the annular drop with initial outer radius larger than the equilibrium value 'opens'.

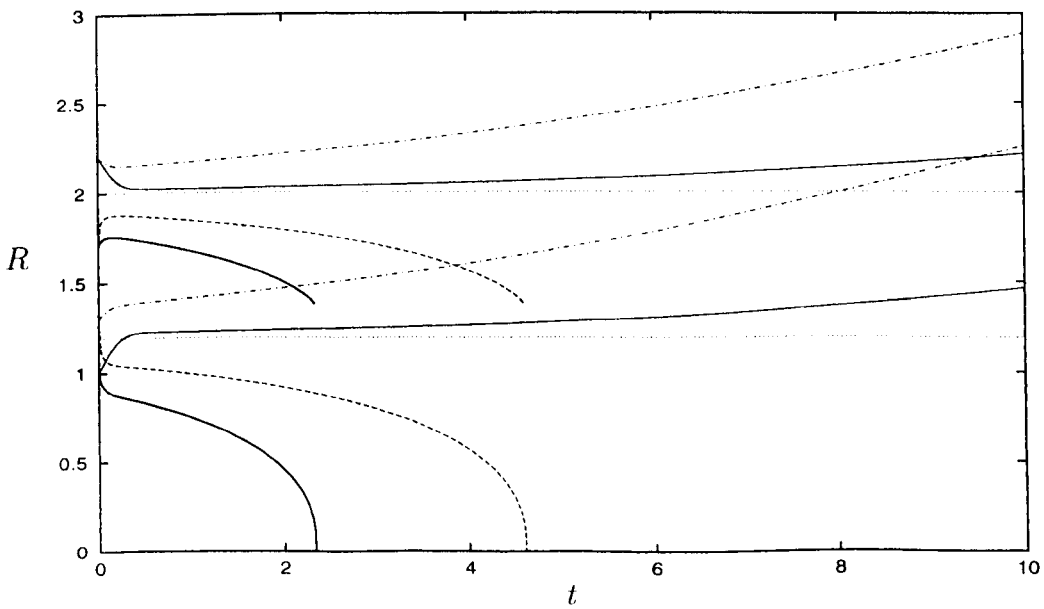

Figure 3.9: Examples of the evolution of drop radii $R_1(t)$ and $R_2(t)$ for an axisymmetric annular drop in the case of zero gravity when $J_0 = 1$ and $V_0 = 0.1696$, obtained by solving Eqs. (3.2) and (3.3) numerically in the case $F_1(\phi) = \phi^3 - 1$ and $F_2(\theta) = \theta^3 - 1$. The unstable equilibrium values $R_1 \approx 1.1968$, $R_2 = 2$ are indicated by horizontal dashed lines. The initial conditions are $R_1(0) = 1$, $R_2(0) = 1.7$ (thick lines), $R_1(0) = 1$, $R_2(0) = 2.2$ (thin lines), $R_1(0) = 1.3$, $R_2(0) = 1.7$ (dashed lines) and $R_1(0) = 1.3$, $R_2(0) = 2.2$ (dot-dashed lines).

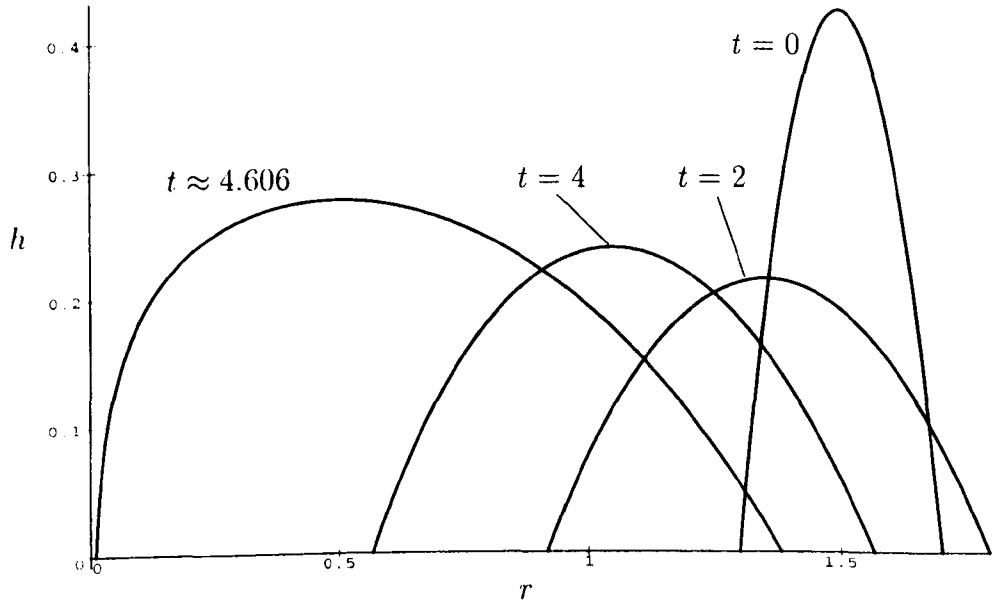

Figure 3.10: Evolution of a quasi-static drop profile for an axisymmetric annular drop in the case of zero gravity when $J_0 = 1$, $V_0 = 0.1696$, with the initial conditions $R_1(0) = 1.3$, $R_2(0) = 1.7$.

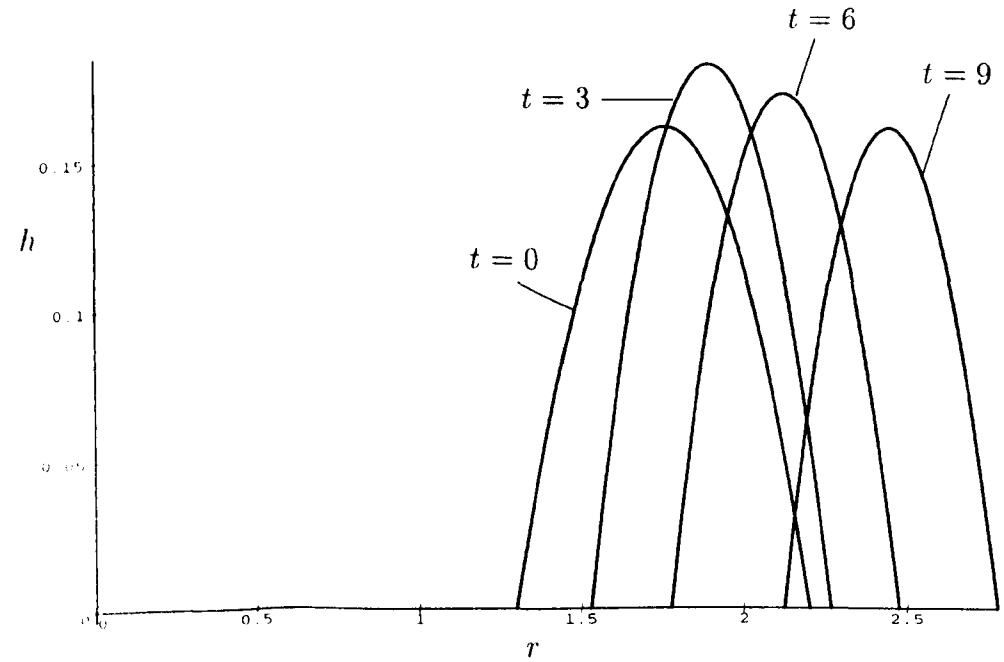

Figure 3.11: Evolution of a quasi-static drop profile for an axisymmetric annular drop in the case of zero gravity when $J_0 = 1$, $V_0 = 0.1696$, with the initial conditions $R_1(0) = 1.3$, $R_2(0) = 2.2$.

Chapter 4

Numerical Solution of Linear Differential Eigenvalue Problems

4.1 Introduction

So far in this thesis we have only considered stability in the quasi-static limit corresponding to the special case of zero capillary number. Analysing stability for non-zero capillary number typically gives rise to high-order differential equations which must, in general, be solved numerically. There have been numerous studies of this kind. For example, Troian *et al.* [53] investigated the linear stability of a capillary ridge on an inclined plane, Hocking & Miksis [23] studied the linear stability of a ridge of fluid of finite width on an inclined plane and López *et al.* [35] analysed the linear stability of a hole in a laterally-bounded thin film. In this Chapter, therefore, we describe a numerical finite-difference code capable of solving an eigenvalue problem posed by n coupled linear ordinary differential equations with appropriate boundary conditions. Specifically, we require the solution of the system given by

$$V_i(Y_1, Y_2, \ldots, Y_n) = \lambda W_i(Y_1, Y_2, \ldots, Y_n), \quad i = 1, \ldots, n, \tag{4.1}$$

where

$$V_i = \sum_{j=1}^{n} \sum_{s=0}^{l_{ij}} h_s^{ij}(x) Y_j^{(s)}(x), \quad i = 1, \ldots, n,$$

$$W_i = \sum_{j=1}^{n} \sum_{s=0}^{m_{ij}} g_s^{ij}(x) Y_j^{(s)}(x), \quad i = 1, \ldots, n,$$

where we have defined

$$Y_j^{(s)}(x) = \frac{\mathrm{d}^s Y_j}{\mathrm{d}x^s},$$

where Y_j are the unknown variables and h_s^{ij} and g_s^{ij} are the coefficients of the jth unknown to the sth derivative in the ith equation of V and W respectively. If we define $b_i = \max(\max_{j=1,\ldots,n}(l_{ij}), \max_{j=1,\ldots,n}(m_{ij}))$ for $i = 1, \ldots, n$ then we require b_i boundary conditions for the ith equation. We associate ℓ_i lower boundary conditions (evaluated at $x = a$) and u_i upper boundary conditions (evaluated at $x = b$) with the ith equation such that $\ell_i + u_i = b_i$. The lower boundary conditions are listed as

$$\sum_{j=1}^{n} \sum_{s=0}^{\gamma_{ijk}} \alpha_{sk}^{ij}(a) Y_j^{(s)}(a) = 0, \quad k = 1, \ldots, \ell_i, \quad i = 1, \ldots, n, \tag{4.2}$$

and the upper boundary conditions as

$$\sum_{j=1}^{n} \sum_{s=0}^{\delta_{ijk}} \beta_{sk}^{ij}(b) Y_j^{(s)}(b) = 0, \quad k = 1, \ldots, u_i, \quad i = 1, \ldots, n, \tag{4.3}$$

where α_{sk}^{ij} and β_{sk}^{ij} are the coefficients of the jth unknown to the sth derivative in the ith equation corresponding to the kth lower and upper boundary condition respectively. Each boundary condition corresponds to one row entry in a matrix, however the order in which the boundary conditions appear in the matrix has no influence on the solution itself.

4.2 Numerical Solution

A FORTRAN code was written to solve the eigenvalue problem specified by Eq. (4.1) and the boundary conditions (4.2) and (4.3) numerically using a finite-difference method and is capable of adopting arbitrary order approximations for any order of derivative appearing in either the equations or boundary conditions limited only by the number of grid points, $N+1$. To obtain the finite-difference weights we use the notably short and fast algorithm recently discovered by Fornberg [13]. For a given (not necessarily regular) set of grid points $x_0, \ldots, x_N$, the point at which approximations are desired $x = \xi$ (not necessarily a grid point)

and highest order of derivative of interest m, Fornberg's algorithm calculates weights d_{ij}^k such that the approximations

$$\left.\frac{\partial^k f}{\partial x^k}\right|_{x=\xi} \simeq \sum_{j=0}^{i} d_{ij}^k f(x_j), \quad k = 0, \ldots, m, \ i = k, \ldots, N,$$

are all optimal in the sense that they permit the maximum order of approximation possible for a stencil consisting of $i+1$ points. For example, approximations of the first derivative at a grid point x_i in a regular grid are given by

$$f'(x_i) = \begin{cases} [\quad -\frac{1}{2}f(x_{i-1}) + 0f(x_i) + \frac{1}{2}f(x_{i+1}) \quad]/h + O(h^2) \\ [\frac{1}{12}f(x_{i-2}) - \frac{2}{3}f(x_{i-1}) + 0f(x_i) + \frac{2}{3}f(x_{i+1}) - \frac{1}{12}f(x_{i+2})]/h + O(h^4) \\ \vdots \end{cases}$$

which can easily be verified by Taylor series. In terms of the relabelled grid nodes $y_0 = x_i$, $y_1 = x_{i-1}$, $y_2 = x_{i+1}$, $y_3 = x_{i-2}$, ...we have the weights $d_{20}^1 = 0$, $d_{21}^1 = -\frac{1}{2}$ and $d_{22}^1 = \frac{1}{2}$ for the second-order approximation and $d_{40}^1 = 0$, $d_{41}^1 = -\frac{2}{3}$, $d_{42}^1 = \frac{2}{3}$, $d_{43}^1 = \frac{1}{12}$ and $d_{44}^1 = -\frac{1}{12}$ for the fourth-order approximation. Table 4.1 is taken from Fornberg & Sloan [14] and gives the weights for some centred difference approximations on a regular grid for various orders of accuracy and various derivatives. Table 4.2 is also taken from Fornberg & Sloan [14] and gives the weights for some one-sided difference approximations on a regular grid for various orders of accuracy and various derivatives which will be used at the boundaries in the present application (note that only the left-hand boundary is represented in Table 4.2, however similar results for the right-hand boundary follow immediately).

In the present application we will obtain approximations at the grid points only. In addition we will only apply the algorithm to a subset of the domain, the number of nodes depending on the required order of approximation to the derivative I. We have modified the algorithm slightly such that we introduce weights c_{jw}^k where

$$\left.\frac{\mathrm{d}^k f}{\mathrm{d}x^k}\right|_{x=x_w} \simeq \sum_{j=s_0^w}^{s_n^w} c_{jw}^k f(x_j), \tag{4.4}$$

where the number of nodes in the stencil is given by $s_n^w - s_0^w + 1$. For a given accuracy I the number of nodes in a particular stencil depends on the derivative

		LOCATION OF GRID NODES								
k	I	-4	-3	-2	-1	0	1	2	3	4
0	∞					1				
1	2				$-\frac{1}{2}$	0	$\frac{1}{2}$			
	4			$\frac{1}{12}$	$-\frac{2}{3}$	0	$\frac{2}{3}$	$-\frac{1}{12}$		
	6		$-\frac{1}{60}$	$\frac{3}{20}$	$-\frac{3}{4}$	0	$\frac{3}{4}$	$-\frac{3}{20}$	$\frac{1}{60}$	
	8	$\frac{1}{280}$	$-\frac{4}{105}$	$\frac{1}{5}$	$-\frac{4}{5}$	0	$\frac{4}{5}$	$-\frac{1}{5}$	$\frac{4}{105}$	$-\frac{1}{280}$
2	2				1	-2	1			
	4			$-\frac{1}{12}$	$\frac{4}{3}$	$-\frac{5}{2}$	$\frac{4}{3}$	$-\frac{1}{12}$		
	6		$\frac{1}{90}$	$-\frac{3}{20}$	$\frac{3}{2}$	$-\frac{49}{18}$	$\frac{3}{2}$	$-\frac{3}{20}$	$\frac{1}{90}$	
	8	$-\frac{1}{560}$	$\frac{8}{315}$	$-\frac{1}{5}$	$\frac{8}{5}$	$-\frac{205}{72}$	$\frac{8}{5}$	$-\frac{1}{5}$	$\frac{8}{315}$	$-\frac{1}{560}$
3	2			$-\frac{1}{2}$	1	0	-1	$\frac{1}{2}$		
	4		$\frac{1}{8}$	-1	$\frac{13}{8}$	0	$-\frac{13}{8}$	1	$-\frac{1}{8}$	
	6	$-\frac{7}{240}$	$\frac{3}{10}$	$-\frac{169}{120}$	$\frac{61}{30}$	0	$-\frac{61}{30}$	$\frac{169}{120}$	$-\frac{3}{10}$	$\frac{7}{240}$

Table 4.1: Weights for some centred difference schemes on a regular grid. The approximations are evaluated at grid node 0. The parameter k denotes the derivative and I denotes the order of accuracy of the approximation.

		LOCATION OF GRID NODES								
k	I	0	1	2	3	4	5	6	7	8
0	∞	1								
1	1	-1	1							
	2	$-\frac{3}{2}$	2	$-\frac{1}{2}$						
	3	$-\frac{11}{6}$	3	$-\frac{3}{2}$	$\frac{1}{3}$					
	4	$-\frac{25}{12}$	4	-3	$\frac{4}{3}$	$-\frac{1}{4}$				
	5	$-\frac{137}{60}$	5	-5	$\frac{10}{3}$	$-\frac{5}{4}$	$\frac{1}{5}$			
	6	$-\frac{49}{20}$	6	$-\frac{15}{2}$	$\frac{20}{3}$	$-\frac{15}{4}$	$\frac{6}{5}$	$-\frac{1}{6}$		
	7	$-\frac{363}{140}$	7	$-\frac{21}{2}$	$\frac{35}{3}$	$-\frac{35}{4}$	$\frac{21}{5}$	$-\frac{7}{6}$	$\frac{1}{7}$	
	8	$-\frac{761}{280}$	8	-14	$\frac{56}{3}$	$-\frac{35}{2}$	$\frac{56}{5}$	$-\frac{14}{3}$	$\frac{8}{7}$	$-\frac{1}{8}$
2	1	1	-2	1						
	2	2	-5	4	-1					
	3	$\frac{35}{12}$	$-\frac{26}{3}$	$\frac{19}{2}$	$-\frac{14}{3}$	$\frac{11}{12}$				
	4	$\frac{15}{4}$	$-\frac{77}{6}$	$\frac{107}{6}$	-13	$\frac{61}{12}$	$-\frac{5}{6}$			
	5	$\frac{203}{45}$	$-\frac{87}{5}$	$\frac{117}{4}$	$-\frac{254}{9}$	$\frac{33}{2}$	$-\frac{27}{5}$	$\frac{137}{180}$		
	6	$\frac{469}{90}$	$-\frac{223}{10}$	$\frac{879}{20}$	$-\frac{949}{18}$	41	$-\frac{201}{10}$	$\frac{1019}{180}$	$-\frac{7}{10}$	
	7	$\frac{29531}{5040}$	$-\frac{962}{35}$	$\frac{621}{10}$	$-\frac{4006}{45}$	$\frac{691}{8}$	$-\frac{282}{5}$	$\frac{2143}{90}$	$-\frac{206}{35}$	$\frac{363}{560}$
3	1	-1	3	-3	1					
	2	$-\frac{5}{2}$	9	-12	7	$-\frac{3}{2}$				
	3	$-\frac{17}{4}$	$\frac{71}{4}$	$-\frac{59}{2}$	$\frac{49}{2}$	$-\frac{41}{4}$	$\frac{7}{4}$			
	4	$-\frac{49}{8}$	29	$-\frac{461}{8}$	62	$-\frac{307}{8}$	13	$-\frac{15}{8}$		
	5	$-\frac{967}{120}$	$\frac{638}{15}$	$-\frac{3929}{40}$	$\frac{389}{3}$	$-\frac{2545}{24}$	$\frac{268}{5}$	$-\frac{1849}{120}$	$\frac{29}{15}$	
	6	$-\frac{801}{80}$	$\frac{349}{6}$	$-\frac{18353}{120}$	$\frac{2391}{10}$	$-\frac{1457}{6}$	$\frac{4891}{30}$	$-\frac{561}{8}$	$\frac{527}{30}$	$-\frac{469}{240}$

Table 4.2: Weights for some one-sided difference schemes on a regular grid. The approximations are evaluated at grid node 0. The parameter k denotes the derivative and I denotes the order of accuracy of the approximation.

k to be approximated and whether the approximation is centred (as in Table 4.1) or one-sided (as in Table 4.2). If we define N_s^o and N_s^c as

$$N_s^o = I + k - 1,$$
$$N_s^c = \begin{cases} I + k - 1, & \text{if } k \text{ is odd,} \\ I + k - 2, & \text{if } k \text{ is even.} \end{cases}$$

then $N_s^o + 1$ corresponds to the number of nodes in a one-sided stencil and $N_s^c + 1$ corresponds to the number of nodes in a centred stencil for a given accuracy I and derivative k.

4.2.1 Differentiation Matrices

Before solving the eigenvalue problem itself, it is useful to generate the differentiation matrices $D^{(k)}$ (square matrices of size $N+1$ with elements $D_{ij}^{(k)}$) associated with the problem which approximate the derivatives of the unknown variables i.e.

$$Y_j^{(k)} \simeq D^{(k)} \mathbf{Y}_j,$$

where $\mathbf{Y}_j = (Y_{j0}, Y_{j1}, \ldots, Y_{jN})^T$, Y_{jl} represents our approximation to $Y_j(x_l)$ and k is the value of the derivative. The first row of the matrix $D^{(k)}$ corresponds to the approximation of the kth derivative at x_0. The second row corresponds to the approximation at x_1, and so on. Therefore we have

$$D^{(k)}_{(w+1)\,(j+1)} = c^k_{jw}, \tag{4.5}$$

for $j = 0, \ldots, N_s^o$ and $w = 0, \ldots, N_s^c/2 - 1$. Equation (4.5) is used to calculate the entries for the first $N_s^c/2$ rows of $D^{(k)}$ and uses one-sided differences. The entries for rows $N + 2 - N_s^c/2, \ldots, N + 1$ (again using one-sided differences) are given by

$$D^{(k)}_{(w+1)\,(N+j+1-N_s^o)} = c^k_{(N-N_s^o+j)\,w}, \tag{4.6}$$

for $j = 0, \ldots, N_s^o$ and $w = N + 1 - N_s^c/2, \ldots, N$. The entries for the remaining rows correspond to centred differences and are given by

$$D^{(k)}_{(w+1)\,(j+w+1-N_s^c/2)} = c^k_{(j+w-N_s^c/2)\,w}, \tag{4.7}$$

for $j = 0, \ldots, N_s^c$ and $w = N_s^c/2, \ldots, N - N_s^c/2$. All other elements of the matrices $D^{(k)}$ are set to zero.

4.2.2 An Algebraic Eigenvalue Problem

We are now in a position to set up our eigenvalue problem. Using the differentiation matrices described in the previous section we generate square matrices A and B (of size $n(N+1)$) using the following algorithm:

$p := 1$ to n
$q := 1$ to n
$k := 0$ to l_{pq} (for matrix A) or m_{pq} (for matrix B)
$i := 1$ to $N+1$
$j := 1$ to $N+1$

$$A_{[(p-1)(N+1)+i][(q-1)(N+1)+j]} := A_{[(p-1)(N+1)+i][(q-1)(N+1)+j]} + D_{ij}^{(k)} h_k^{pq}(x_{i-1})$$

$$B_{[(p-1)(N+1)+i][(q-1)(N+1)+j]} := B_{[(p-1)(N+1)+i][(q-1)(N+1)+j]} + D_{ij}^{(k)} g_k^{pq}(x_{i-1})$$

We now enter the rows of the matrices A and B that correspond to the boundary conditions. First, we initialise all elements in the rows of A and B that will occupy these boundary conditions to zero. The algorithm that generates the rows of matrix A for the lower boundary conditions is given by

$p := 1$ to n
$q := 1$ to n
$r := 1$ to ℓ_p
$k := 0$ to γ_{pqr}
$j := 1$ to $N+1$

$$A_{[(p-1)(N+1)+r][(q-1)(N+1)+j]} := A_{[(p-1)(N+1)+r][(q-1)(N+1)+j]} + D_{1j}^{(k)} \alpha_{kr}^{pq}(a)$$

and the algorithm that generates the rows of matrix A for the upper boundary conditions is given by

$p := 1$ to n
$q := 1$ to n
$r := u_p - 1$ to 0
$k := 0$ to δ_{pqr}
$j := 1$ to $N+1$

$$A_{[p(N+1)-r][(q-1)(N+1)+j]} := A_{[p(N+1)-r][(q-1)(N+1)+j]} + D_{(N+1)j}^{(k)} \beta_{kr}^{pq}(b)$$

The elements of the corresponding rows of matrix B are zero.

We have thus derived the algebraic eigenvalue problem given by

$$A\mathbf{Y} = \lambda B\mathbf{Y}, \tag{4.8}$$

for eigenvalues λ and eigenvectors

$$\mathbf{Y} = (Y_{10}, Y_{11}, \ldots, Y_{1N}, Y_{20}, \ldots, Y_{2N}, \ldots, Y_{n0}, \ldots, Y_{nN})^T. \tag{4.9}$$

Figures 4.1 and 4.2 provide a summary of the structure of the matrices A and B respectively. The eigenvalues (and eigenvectors if required) are then found by the QZ algorithm described by Wilkinson [58], implemented using NAG routine F02GJF. The computational cost of this method is $O(N_{AB}^3)$ where N_{AB} is the order of the matrices A and B. Doubling the number of grid points approximately octuples the runtime of the code since the majority of runtime is taken up by the QZ algorithm rather than obtaining the matrices A and B. Note that the differential equation coefficients h_s^{ij} and g_s^{ij} as well as the eigenvalue λ and eigenfunctions $Y_1, \ldots, Y_n$ are assumed to be complex in general and we must decompose the matrices A and B into their real and imaginary parts to implement NAG routine F02GJF.

4.3 Test Problems

In order to test the code and gain some idea of the influence of the various numerical parameters at the user's disposal, such as number of grid nodes, accuracy of approximation to the derivatives and grid point distribution for example, we first use the code to solve various problems with analytic or known numerical solution, before tackling an entirely new problem.

4.3.1 Example 1: The Harmonic Equation

The first and simplest test problem is given by the harmonic equation

$$\frac{\mathrm{d}^2 Y}{\mathrm{d}x^2} = -\lambda^2 Y, \tag{4.10}$$

DESCRIPTION	ROW
1st lower b.c. corresponding to 1st eq.	1
2nd lower b.c. corresponding to 1st eq.	2
⋮	⋮
ℓ_1th lower b.c. corresponding to 1st eq.	ℓ_1
V_1 approximated at $x = x_{\ell_1}$	$\ell_1 + 1$
V_1 approximated at $x = x_{\ell_1+1}$	$\ell_1 + 2$
⋮	⋮
V_1 approximated at $x = x_{N-u_1}$	$N + 1 - u_1$
1st upper b.c. corresponding to 1st eq.	$N + 2 - u_1$
2nd upper b.c. corresponding to 1st eq.	$N + 3 - u_1$
⋮	⋮
u_1th upper b.c. corresponding to 1st eq.	$N + 1$
⋮	⋮
1st lower b.c. corresponding to ith eq.	$(i-1)(N+1) + 1$
2nd lower b.c. corresponding to ith eq.	$(i-1)(N+1) + 2$
⋮	⋮
ℓ_ith lower b.c. corresponding to ith eq.	$(i-1)(N+1) + \ell_i$
V_i approximated at $x = x_{\ell_i}$	$(i-1)(N+1) + \ell_i + 1$
V_i approximated at $x = x_{\ell_i+1}$	$(i-1)(N+1) + \ell_i + 2$
⋮	⋮
V_i approximated at $x = x_{N-u_i}$	$i(N+1) - u_i$
1st upper b.c. corresponding to ith eq.	$i(N+1) - u_i + 1$
2nd upper b.c. corresponding to ith eq.	$i(N+1) - u_i + 2$
⋮	⋮
u_ith upper b.c. corresponding to ith eq.	$i(N+1)$
⋮	⋮
1st lower b.c. corresponding to nth eq.	$(n-1)(N+1) + 1$
2nd lower b.c. corresponding to nth eq.	$(n-1)(N+1) + 2$
⋮	⋮
ℓ_nth lower b.c. corresponding to nth eq.	$(n-1)(N+1) + \ell_n$
V_n approximated at $x = x_{\ell_n}$	$(n-1)(N+1) + \ell_n + 1$
V_n approximated at $x = x_{\ell_n+1}$	$(n-1)(N+1) + \ell_n + 2$
⋮	⋮
V_n approximated at $x = x_{N-u_n}$	$n(N+1) - u_n$
1st upper b.c. corresponding to nth eq.	$n(N+1) - u_n + 1$
2nd upper b.c. corresponding to nth eq.	$n(N+1) - u_n + 2$
⋮	⋮
u_nth upper b.c. corresponding to nth eq.	$n(N+1)$

Figure 4.1: A summary of the structure of the matrix A.

DESCRIPTION	ROW
0	1
⋮	⋮
0	ℓ_1
W_1 approximated at $x = x_{\ell_1}$	$\ell_1 + 1$
W_1 approximated at $x = x_{\ell_1+1}$	$\ell_1 + 2$
⋮	⋮
W_1 approximated at $x = x_{N-u_1}$	$N + 1 - u_1$
0	$N + 2 - u_1$
⋮	⋮
0	$N + 1$
⋮	⋮
0	$(i-1)(N+1) + 1$
⋮	⋮
0	$(i-1)(N+1) + \ell_i$
W_i approximated at $x = x_{\ell_i}$	$(i-1)(N+1) + \ell_i + 1$
W_i approximated at $x = x_{\ell_i+1}$	$(i-1)(N+1) + \ell_i + 2$
⋮	⋮
W_i approximated at $x = x_{N-u_i}$	$i(N+1) - u_i$
0	$i(N+1) - u_i + 1$
⋮	⋮
0	$i(N+1)$
⋮	⋮
0	$(n-1)(N+1) + 1$
⋮	⋮
0	$(n-1)(N+1) + \ell_n$
W_n approximated at $x = x_{\ell_n}$	$(n-1)(N+1) + \ell_n + 1$
W_n approximated at $x = x_{\ell_n+1}$	$(n-1)(N+1) + \ell_n + 2$
⋮	⋮
W_n approximated at $x = x_{N-u_n}$	$n(N+1) - u_n$
0	$n(N+1) - u_n + 1$
⋮	⋮
0	$n(N+1)$

Figure 4.2: A summary of the structure of the matrix B.

$$A = \begin{pmatrix} 1 & 0 & & & & \\ 1 & -2 & 1 & & & \\ & 1 & -2 & 1 & & \\ & & \ddots & \ddots & \ddots & \\ & & & 1 & -2 & 1 \\ & & & & 0 & 1 \end{pmatrix}, \quad B = \begin{pmatrix} 0 & 0 & & & & \\ 0 & 1 & 0 & & & \\ & 0 & 1 & 0 & & \\ & & \ddots & \ddots & \ddots & \\ & & & 0 & 1 & 0 \\ & & & & 0 & 0 \end{pmatrix}.$$

Figure 4.3: The structure of the matrices A and B for the discretised version of the harmonic equation.

subject to the boundary conditions

$$Y(0) = Y(1) = 0. \tag{4.11}$$

This yields a second-order eigenvalue problem which is easily solved to give eigenvalues $\lambda = n\pi$ corresponding to eigenfunctions $Y_n(x) = A_n \sin(n\pi x)$ for $n = 1, 2, \ldots$. For this problem we have only one equation to solve. If we adopt a second-order approximation to the derivative ($I = 2$) then on a regular grid (with node spacing h) we have

$$\frac{\mathrm{d}^2 Y(x_i)}{\mathrm{d}x^2} = \frac{Y(x_{i-1}) - 2Y(x_i) + Y(x_{i+1})}{h^2},$$

at the nodes $x = x_i$ for $i = 1, \ldots, N-1$. The boundary conditions are simply given as

$$Y(x_0) = Y(x_N) = 0.$$

We therefore yield the scheme

$$Y_0 = 0, \tag{4.12}$$

$$\frac{Y_{i+1} - 2Y_i + Y_{i-1}}{h^2} = -\lambda^2 Y_i, \quad i = 1, \ldots, N-1, \tag{4.13}$$

$$Y_N = 0, \tag{4.14}$$

where Y_i is our approximation to $Y(x_i)$ at x_i and $Nh = 1$. Written out in the matrix form described in Sec. 4.2.2 we have $A\mathbf{Y} = \nu B\mathbf{Y}$ where A and B are shown in Fig. 4.3 and $\nu = -\lambda^2 h^2$. Some results for this second-order scheme

N	Eigenvalues λ/π
5	0.984, 1.871, 2.575, 3.027
6	0.989, 1.910, 2.701, 3.310, 3.690
7	0.991, 1.933, 2.778, 3.484, 4.015, 4.345
10	0.996, 1.967, 2.890, 3.742, 4.502, 5.150, 5.672, 6.055, 6.288
15	0.998, 1.985, 2.951, 3.884, 4.775, 5.613, 6.390, 7.097, 7.726, 8.270, 8.724, 9.082, 9.341, 9.500

Table 4.3: Numerical results for the harmonic equation.

($I = 2$) for various values of N are given in Table 4.3. In general, we find that increasing N for a given order always leads to more accurate results. Since the matrix B contains two purely zero rows, two of the $N+1$ eigenvalues that NAG routine F02GJF returns will be spurious. These are omitted from the table.

4.3.2 Example 2: A Complex-valued Eigenvalue Problem

A less elementary complex-valued test problem is given by the fourth-order differential equation

$$\frac{\mathrm{d}^4u}{\mathrm{d}x^4} + a\frac{\mathrm{d}^2u}{\mathrm{d}x^2} + bu = \lambda\left[\frac{\mathrm{d}^2u}{\mathrm{d}x^2} + cu\right], \tag{4.15}$$

where a, b and c are constants, subject to the boundary conditions

$$\begin{aligned} u(0) &= u''(0) = 0, \\ u(1) &= u''(1) = 0, \end{aligned} \tag{4.16}$$

where the prime denotes differentiation with respect to x. It is straightforward to show that a solution set is given by $u(x) = \sin(n\pi x)$ for $n = 1, 2, \ldots$, with eigenvalues given by

$$\lambda_n = \frac{(n\pi)^4 - a(n\pi)^2 + b}{c - (n\pi)^2}, \quad n = 1, 2, \ldots. \tag{4.17}$$

In the case $n = 1$ and $a = 2 + i$, $b = 3 + 2i$ and $c = 1 + i$ we find from Eq. (4.17) that $\lambda_1 = -9.079711517 - 0.136433041i$ to 9 decimal places. Table 4.4 gives the numerical solution in this case for $N = 14$ and $N = 40$ for different orders of accuracy I on a regular grid. Again we find that, in general, increasing the

	$N = 14$		$N = 40$	
I	$\mathrm{Re}(\lambda_1)$	$\mathrm{Im}(\lambda_1)$	$\mathrm{Re}(\lambda_1)$	$\mathrm{Im}(\lambda_1)$
2	-9.187772160	-0.153325847	-9.081383932	-0.137267577
4	-9.068372056	-0.135191553	-9.079640290	-0.136425543
8	-9.079678362	-0.136429365	-9.079711524	-0.136433064
10	-9.079713133	-0.136433217	-9.079711615	-0.136433127
12	N/A	N/A	-9.079711583	-0.136433108
14	N/A	N/A	-9.079711489	-0.136432305
24	N/A	N/A	-9.077741329	-0.136453991

Table 4.4: Numerical results for Example 2. The exact value for this example is $\lambda_1 = -9.079711517 - 0.136433041i$ to 9 decimal places. For $I \geq 12$ when $N = 14$ there are insufficient grid points to allow these orders of approximation.

number of grid points increases the accuracy of the solution for a given order of approximation I. Note, however, that there appears to be an optimum value of I for a given number of grid points (in this case $I = 10$ for $N = 14$ and $I = 8$ for $N = 40$).

4.3.3 Example 3: Stability of a Ridge of Fluid

This test problem introduces non-constant coefficients in the governing equation and was derived by Hocking & Miksis [23] who considered the linear stability of a ridge of fluid of finite width on an inclined plane with constant but different contact angles at the leading and trailing edges. Specifically, we require the solution of the ordinary differential equation

$$\begin{aligned} &h_0^2(h_0+\lambda)h_1'''' + h_0h_0'(3h_0+2\lambda)h_1''' - 2q^2h_0^2(h_0+\lambda)h_1'' \\ &-q^2h_0h_0'(3h_0+2\lambda)h_1' + h_0^2(h_0+\lambda)q^4h_1 = -\omega h_1, \end{aligned} \tag{4.18}$$

subject to the boundary conditions

$$\begin{aligned} (1-k)h_1'(-1) + (1-3k)h_1(-1) &= 0, \\ (1+k)h_1'(1) - (1+3k)h_1(1) &= 0, \end{aligned} \tag{4.19}$$

where λ, ω, q and h_1 represent the slip coefficient, growth parameter, disturbance wavenumber and disturbance ridge height respectively, and a prime denotes differentiation with respect to x. The basic state is given by $h_0 = \frac{3}{4}(1-x^2)(1+$

c	ω	c	ω	c	ω
0.5	0.49299354	3	0.46632354	5.5	0.45134691
1	0.48929054	3.5	0.46173050	6	0.45011131
1.5	0.48394491	4	0.45805246	6.5	0.44919708
2	0.47784518	4.5	0.45519104	7	0.44853050
2.5	0.47178626	5	0.45300162	7.5	0.44805120

Table 4.5: Numerical results for Example 3 for $k = 0.5$, $q = 0.975$, $\lambda = 10^{-2}$ and the numerical parameter values $N = 200$ and $I = 16$. Hocking & Miksis [23] obtained $\omega = 0.451$.

kx) where k is a non-dimensional measure of gravity. In the special case $q = 0$ (but *not* otherwise) we must also impose the additional condition

$$\int_{-1}^{1} h_1 \mathrm{d}x = 0, \tag{4.20}$$

to ensure that the volume of the ridge is conserved. The eigenvalue problem is formed by fixing k, q and λ and solving the system for the eigenvalues ω and eigenfunctions h_1. It is found to be beneficial to use an irregular grid x_i for $i = 0, \ldots, N$, in order to cluster the grid points in the neighbourhood of the contact lines, $x = \pm 1$. This grid is obtained from the regular grid u_i for $i = 0, \ldots, N$, (where $u_0 = 0$ and $u_N = 1$) through the mapping

$$x_i = \frac{\tanh[(u_i - 1/2)c]}{\tanh(c/2)}, \quad \text{for } i = 0, \ldots, N, \tag{4.21}$$

first used by Vinokur [57]. The larger the value of the stretching parameter c the more the grid points are clustered towards the contact lines.

Table 4.5 gives the results for the eigenvalue ω with the largest real part for varying values of the stretching parameter c with $k = 0.5$, $q = 0.975$ and $\lambda = 10^{-2}$ with the numerical parameter values $N = 200$ and $I = 16$. We find that the results are in good agreement with those of Hocking & Miksis [23] (who obtained $\omega = 0.451$) and that $c = 5.5$ yields the most accurate comparison. Using this optimum value of c, Table 4.6 examines the influence of varying N and I on the most positive eigenvalue for $\lambda = 10^{-2}$ and $\lambda = 10^{-4}$ with $k = 0.5$ and $q = 0.975$. This table suggests that in most cases an approximate relation

$\lambda = 10^{-2}$								
N	I	ω	N	I	ω	N	I	ω
60	2	0.52238978	80	2	0.49574334	200	14	0.45141806
60	4	0.43989426	80	4	0.44970131	200	16	0.45134691
60	6	0.47433027	80	6	0.46157770	200	18	0.45130048
60	8	0.44949832	80	8	0.45536027	200	20	0.45125405
60	10	0.47573979	80	10	0.45948762	200	22	0.45122018
$\lambda = 10^{-4}$								
N	I	ω	N	I	ω	N	I	ω
60	2	0.48945727	80	2	0.45686759	200	14	0.38015269
60	4	0.38570580	80	4	0.39318247	200	16	0.37974491
60	6	0.44165088	80	6	0.41639644	200	18	0.37953581
60	8	0.39188148	80	8	0.39981776	200	20	0.37927074
60	10	0.45454969	80	10	0.41315678	200	22	0.37911126

Table 4.6: Numerical results for Example 3 for $k = 0.5$, $q = 0.975$, $c = 5.5$, $\lambda = 10^{-2}$ and $\lambda = 10^{-4}$. Hocking & Miksis [23] obtained $\omega = 0.451$ for $\lambda = 10^{-2}$ and $\omega = 0.377$ for $\lambda = 10^{-4}$.

for the optimum value of I is given by $I \approx N/10$ which will be used in the remaining test problems and Chapters 5 and 6.

Figure 4.4 plots the most unstable eigenvalue ω against wavenumber q for $k = 0.25$, 0.5 and 0.75 when $\lambda = 10^{-2}$ and $\lambda = 10^{-4}$. The neutral stability curves were calculated by Hocking & Miksis [23] and are given by the relation

$$k^2 = \frac{(1+q^2)\tanh(2q) - 2q}{(9+q^2)\tanh(2q) - 6q}, \tag{4.22}$$

which is independent of λ, as confirmed by Fig. 4.4. For reference, Fig. 4.5 plots the eigenfunctions corresponding to the most positive (most unstable) eigenvalue for various values of q when $k = 0.5$ and $\lambda = 10^{-2}$.

4.3.4 Example 4: Stability of a Capillary Ridge

The motivation for the choice of this example is to use the code to solve a problem where the basic-state solution must be obtained numerically. Such a problem was studied by Troian *et al.* [53] who considered the linear stability of a thin film of fluid flowing down an inclined plane. In a frame of reference moving

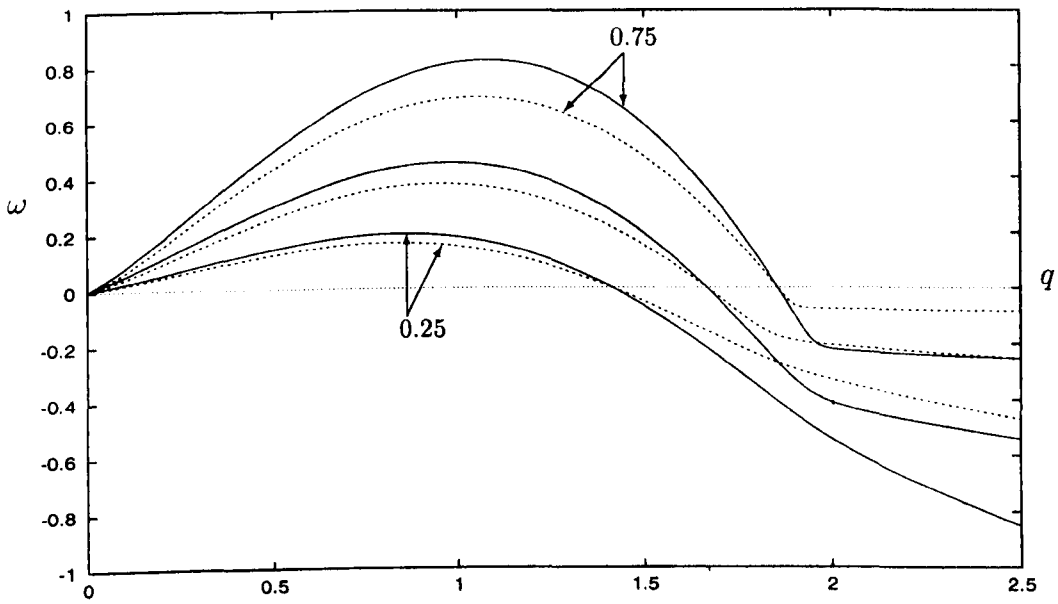

Figure 4.4: Plot of the most unstable eigenvalue ω against wavenumber q for $k = 0.25$, 0.5 and 0.75 when $\lambda = 10^{-2}$ (——) and $\lambda = 10^{-4}$ (- - -) in Example 3.

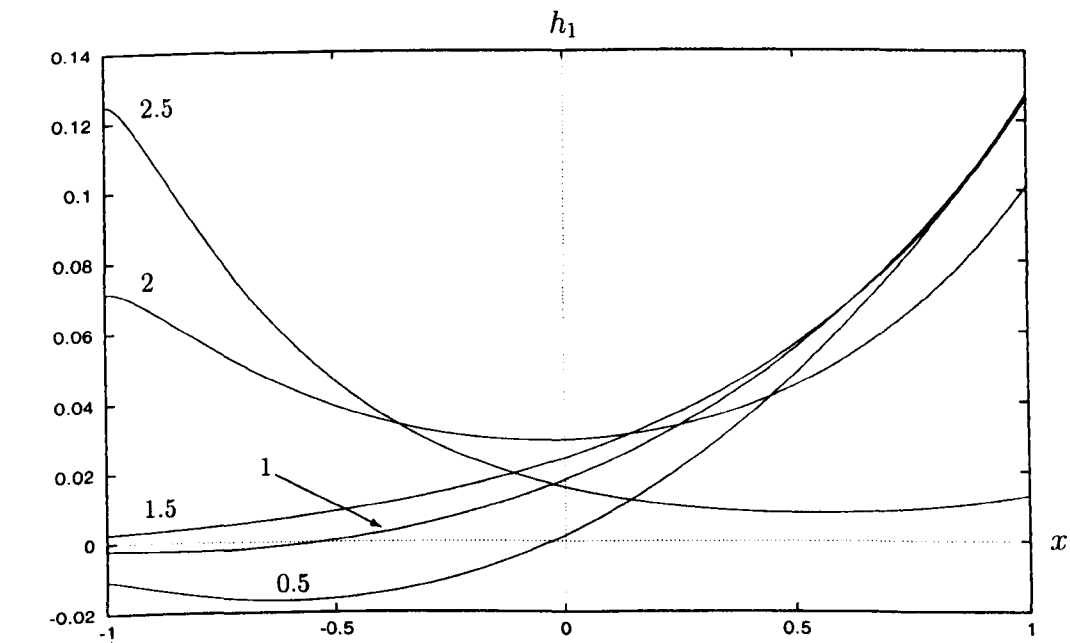

Figure 4.5: Eigenfunctions corresponding to the most unstable mode for various values of q when $k = 0.5$ and $\lambda = 10^{-2}$ with the numerical values $N = 200$, $I = 22$ and $c = 5.5$.

with the capillary ridge the governing equation for the basic-state profile $h_0(x)$ is given by

$$h_0''' = -1 + \frac{b^2+b+1}{h_0^2} - \frac{b(b+1)}{h_0^3}, \tag{4.23}$$

where a prime denotes differentiation with respect to x, and b is the thickness of the precursor layer at the leading edge of the fluid film. The boundary conditions are given by

$$\begin{aligned} h_0 &\to b \quad \text{as} \quad x \to \infty, \\ h_0', h_0'', \ldots &\to 0 \quad \text{as} \quad x \to -\infty. \end{aligned} \tag{4.24}$$

Linearising Eq. (4.23) about the asymptotic value $h_0 \to 1$ as $x \to -\infty$ and solving the resulting differential equation yields

$$h_0 \to 1 + ae^{\beta x}\cos(\sqrt{3}\beta x) \quad \text{as} \quad x \to -\infty, \tag{4.25}$$

where a is a constant of integration and $\beta = (2-b-b^2)^{1/3}/2$. We solve Eq. (4.23) as an initial value problem on a truncated domain $[0:16]$ using NAG routine D02PDF, specifying h_0, h_0' and h_0'' at the left-hand edge using Eq. (4.25). We choose a to be a small parameter about which the solution is iterated until convergence is achieved so that $h_0 \to b$ as $x \to \infty$. Figure 4.6 plots basic-state profiles for $b = 0.05$, 0.075 and 0.1.

We are now in a position to analyse the linear stability of these basic states. The governing equation is given by

$$\begin{aligned} &\sigma h_1 + (h_0^3)h_1'''' + (3h_0^2h_0')h_1''' - (2q^2h_0^3)h_1'' \\ &+ \left[2(1+b+b^2) - \frac{3b(1+b)}{h_0} - 3q^2h_0^2h_0'\right]h_1' + \left[\frac{3b(1+b)h_0'}{h_0^2} + q^4h_0^3\right]h_1 = 0, \end{aligned} \tag{4.26}$$

where q, σ and h_1 represent the disturbance wavenumber, growth parameter and disturbance ridge height respectively. The boundary conditions are given by

$$h_1,\ h_1' \to 0 \quad \text{as} \quad x \to \pm\infty. \tag{4.27}$$

Figure 4.7 plots the most unstable eigenvalue σ against wavenumber q for $b = 0.05$, 0.075 and 0.1, and Fig. 4.8 plots the eigenfunctions h_1 corresponding to the most unstable eigenvalue for $b = 0.1$ when $q = 0.1$, 0.3, 0.5 and 0.7. Similar

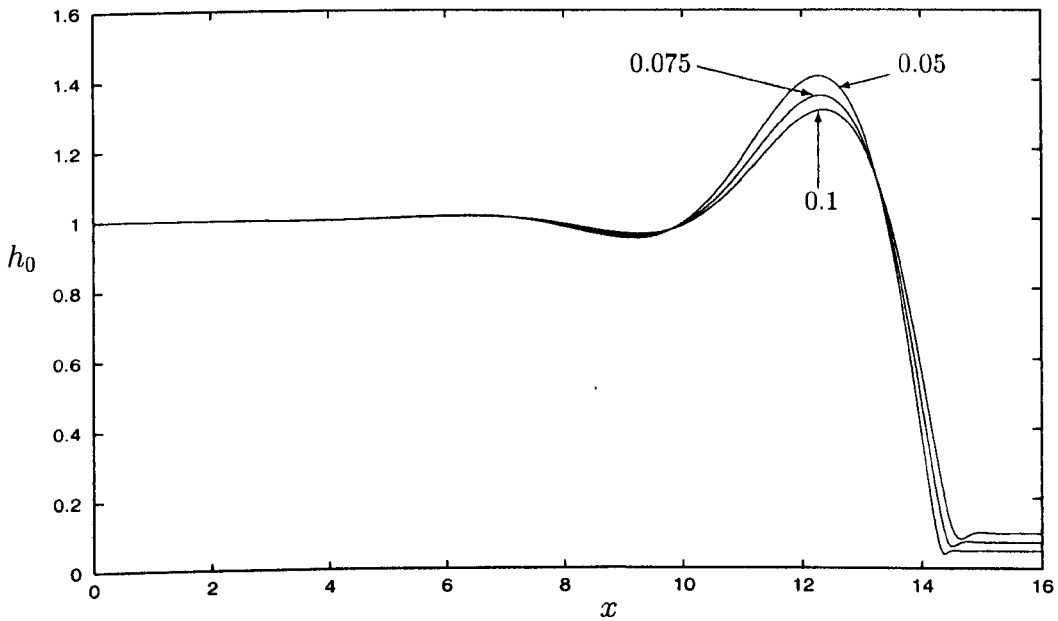

Figure 4.6: Basic-state profiles for $b = 0.05$, 0.075 and 0.1 for Example 4.

results have been given by Troian *et al.* [53], Kataoka & Troian [25] and Spaid & Homsy [49] and show excellent agreement with the present example.

4.3.5 Example 5: Flow in a Wedge

Up until now, all the test problems have consisted of only one equation. Here we use the code to solve three coupled linear differential equations that arise in studying the stability of a fluid with non-uniform density in a wedge with angle A. The geometry of the problem is shown in Fig. 4.9. This example has recently arisen as a simple model for the dynamics of swimming micro-organisms. We require the solution of the system

$$\frac{\partial^4 \hat{U}_\eta}{\partial \eta^4} - 2\alpha^2 \frac{\partial^2 \hat{U}_\eta}{\partial \eta^2} + \alpha^4 \hat{U}_\eta - \alpha^2 \sin A \; \hat{R} = \sigma R_e \left[\frac{\partial^2 \hat{U}_\eta}{\partial \eta^2} - \alpha^2 \hat{U}_\eta \right], \tag{4.28}$$

$$R_e \frac{\partial U}{\partial \eta} \hat{U}_\eta - \frac{\partial^2 \hat{U}_\xi}{\partial \eta^2} + \alpha^2 \hat{U}_\xi - \cos A \; \hat{R} = -\sigma R_e \hat{U}_\xi, \tag{4.29}$$

$$P_e \left(C \sin A + \frac{\partial R}{\partial \eta} \right) \hat{U}_\eta + P_e C \cos A \; \hat{U}_\xi - \frac{\partial^2 \hat{R}}{\partial \eta^2} + \alpha^2 \hat{R} = -\sigma P_e \hat{R}, \tag{4.30}$$

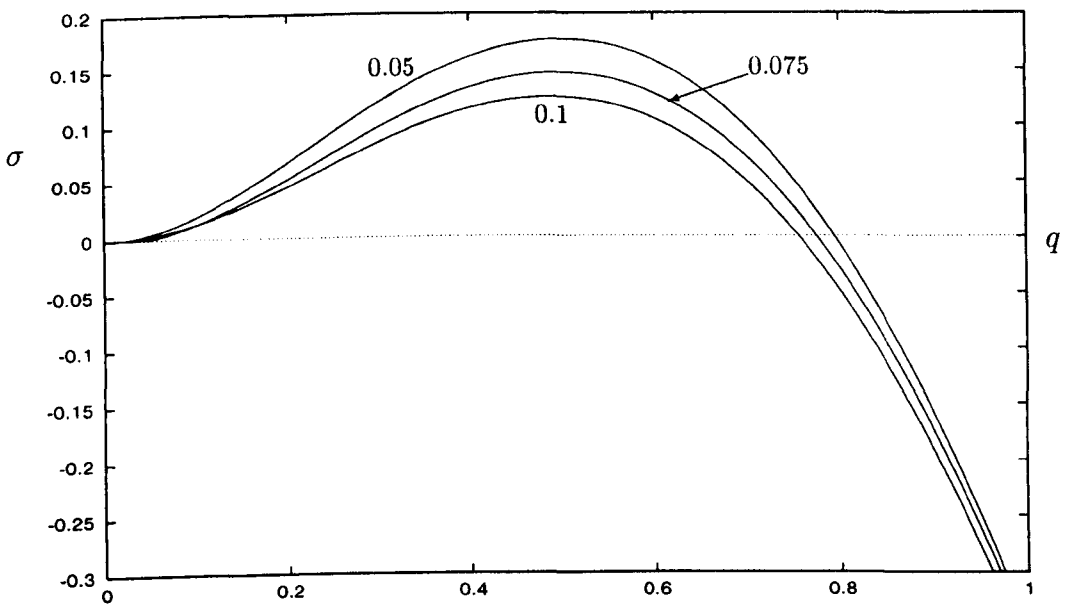

Figure 4.7: Plot of the most unstable eigenvalue σ against wavenumber q for $b = 0.05$, 0.075 and 0.1 in Example 4.

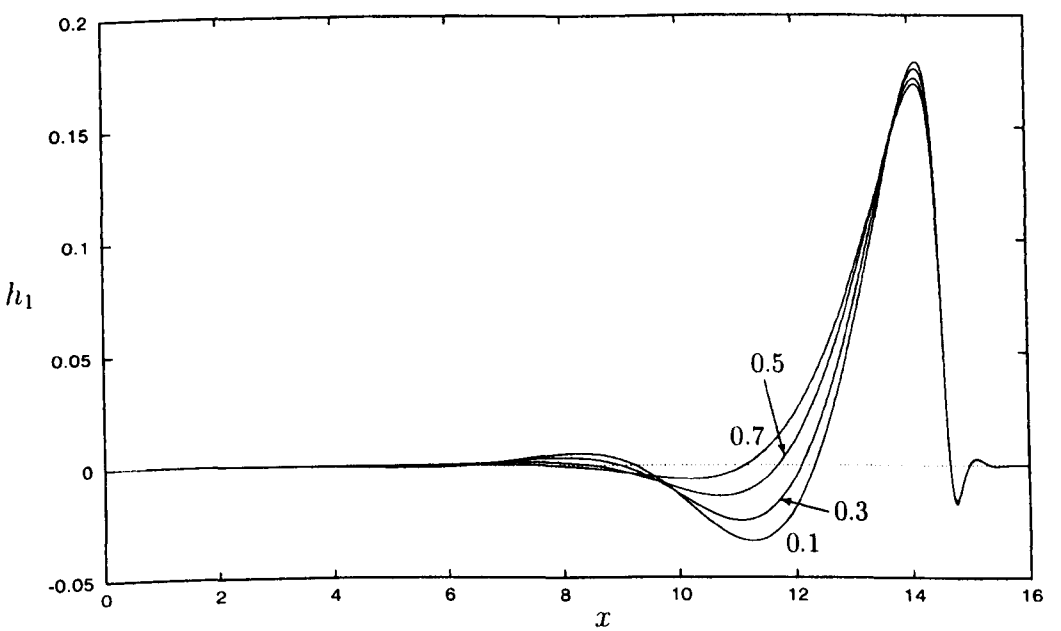

Figure 4.8: Plot of the eigenfunctions corresponding to the most unstable mode for $b = 0.1$ when $q = 0.1$, 0.3, 0.5 and 0.7 in Example 4.

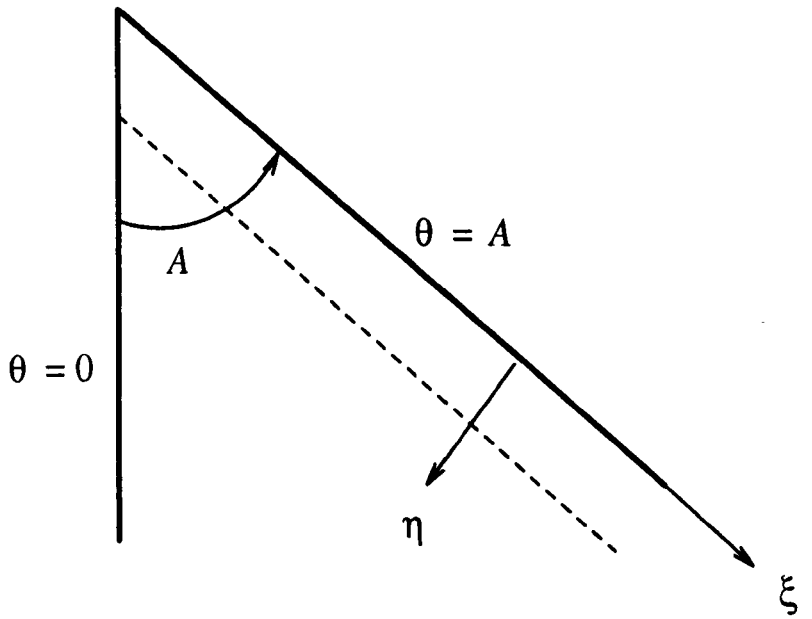

Figure 4.9: Geometry of the problem in Example 5.

which are valid in the boundary layer near $\theta = A$, where R and U are given by

$$R = \frac{C \sin A}{\gamma} e^{-\gamma\eta} \cos(\gamma\eta), \tag{4.31}$$

$$U = 2\gamma \tan A \; e^{-\gamma\eta} \sin(\gamma\eta), \tag{4.32}$$

and

$$\gamma = \left(\frac{P_e C \cos^2 A}{4} \right)^{\frac{1}{4}}, \tag{4.33}$$

where $\hat{U}_\eta$ and $\hat{U}_\xi$ are the disturbance velocities in the η and ξ directions respectively, $\hat{R}$ is the perturbation to the density, R and U are the basic-state density and velocity respectively, R_e is the Reynolds number, P_e is the Peclet number, C is the vertical density gradient, α is the disturbance wavenumber and σ is the growth parameter. Figure 4.10 plots typical basic-state profiles of the density R and the velocity U as functions of η for parameter values $C = 1$, $P_e = 1$ and $A = \pi/4$. The boundary conditions for this system are

$$\begin{aligned} &\hat{U}_\eta = \frac{\partial \hat{U}_\eta}{\partial \eta} = \hat{U}_\xi = \frac{\partial \hat{R}}{\partial \eta} = 0 \quad \text{at} \quad \eta = 0, \\ &\hat{U}_\eta, \; \frac{\partial \hat{U}_\eta}{\partial \eta}, \; \hat{U}_\xi, \; \hat{R} \to 0 \quad \text{as} \quad \eta \to \infty. \end{aligned} \tag{4.34}$$

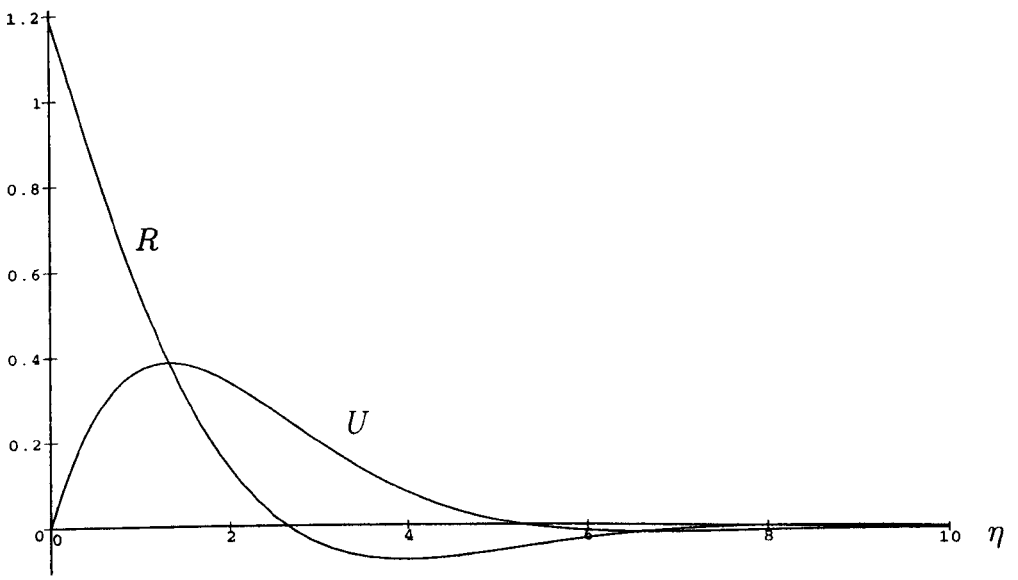

Figure 4.10: Typical basic-state profiles of the density R and the velocity U as functions of η for parameter values $C = 1$, $P_e = 1$ and $A = \pi/4$ in Example 5.

Preliminary experimental results by Prof. John Kessler of Arizona State University suggest the parameter values $R_e = 1$, $P_e = 2 \times 10^4$ and $C = 7.41 \times 10^{-7}$ with a wedge angle $A = \pi/4$. We solve this system on a truncated domain $[0 : L]$ for the eigenvalues σ and the eigenfunctions $\hat{U}_\eta$, $\hat{U}_\xi$ and $\hat{R}$.

Figure 4.11 plots the largest eigenvalue σ against wavenumber α for various values of C. Unlike the previous two examples, here $\sigma < 0$ for all α which corresponds to universally stable solutions. Partial verification of this can be made analytially in the special case $C = 0$.

Substituting $C = 0$ into Eq. (4.30) yields

$$\frac{\partial^2 \hat{R}}{\partial \eta^2} - (\alpha^2 + \sigma P_e)\hat{R} = 0, \tag{4.35}$$

subject to

$$\begin{aligned} &\frac{\partial \hat{R}}{\partial \eta} = 0 \quad \text{at} \quad \eta = 0, \\ &\hat{R} \to 0 \quad \text{as} \quad \eta \to \infty. \end{aligned} \tag{4.36}$$

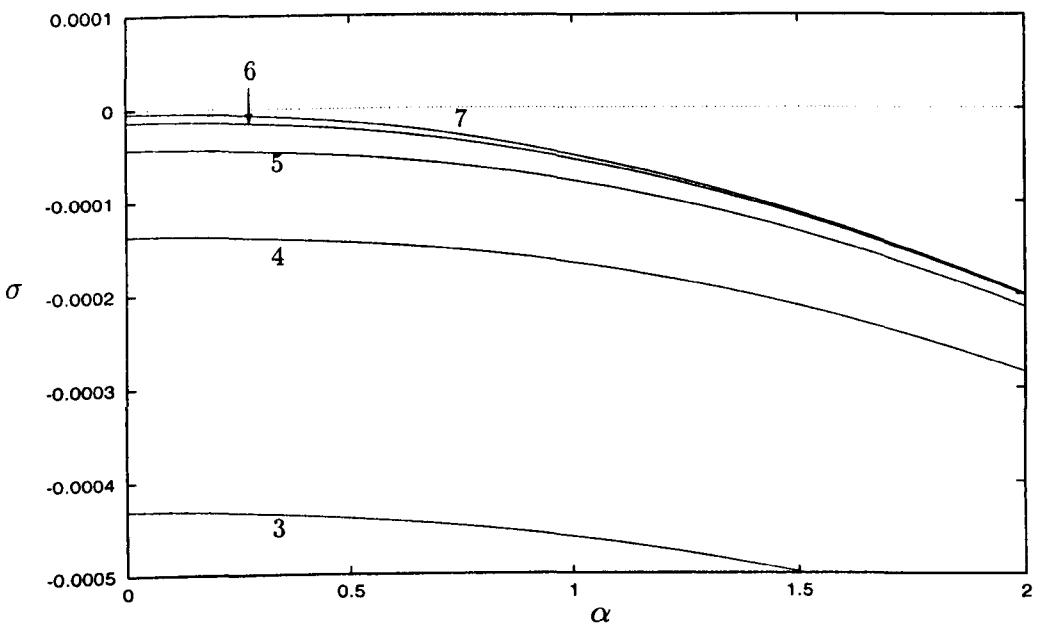

Figure 4.11: Plot of largest eigenvalue σ against wavenumber α for $C = 7.41 \times 10^{-i}$ where $i = 3$, 4, 5, 6 and 7 as indicated, for Example 5 with the numerical values $N = 90$, $I = 12$ and $c = 5.5$.

The general solution of Eq. (4.35) is given by

$$\hat{R} = C_1 \sin\left[-(\alpha^2 + \sigma P_e)^{\frac{1}{2}}\eta\right] + C_2 \cos\left[-(\alpha^2 + \sigma P_e)^{\frac{1}{2}}\eta\right],$$

where C_1 and C_2 are constants. If we change the boundary condition at infinity in Eq. (4.36) to $\hat{R}(L) = 0$ we find that $C_1 = 0$ and for $C_2 \neq 0$ we require

$$\sigma = -\left[\alpha^2 + \left(\frac{\pi}{2L}\right)^2\right] P_e^{-1}. \tag{4.37}$$

Table 4.7 compares numerical results with analytic results from Eq. (4.37) for varying values of α, L and P_e where agreement is excellent. Note that $\sigma \to -\alpha^2/P_e < 0$ as $L \to \infty$ i.e. the flow is stable for $C = 0$.

Figure 4.12 plots the eigenfunctions $\hat{U}_\eta$, $\hat{U}_\xi$ and $\hat{R}$ for the parameter values $C = 0$, $A = \pi/4$, $R_e = 1$, $P_e = 2 \times 10^4$, $\alpha = 0.5$ and $L = 40$.

α	L	P_e	Eq. (4.37)	Code
0	20	20	-0.000308425	-0.000308414
1	30	200	-0.005013707	-0.005013707
2	40	2000	-0.002000771	-0.002000771
0.5	50	20000	-0.000012549	-0.000012549
0.5	100	20000	-0.000012512	-0.000012512

Table 4.7: Comparison between numerical results and Eq. (4.37) for $C = 0$, $A = \pi/4$ and $R_e = 1$ in Example 5 with the numerical values $N = 90$, $I = 12$ and $c = 5.5$.

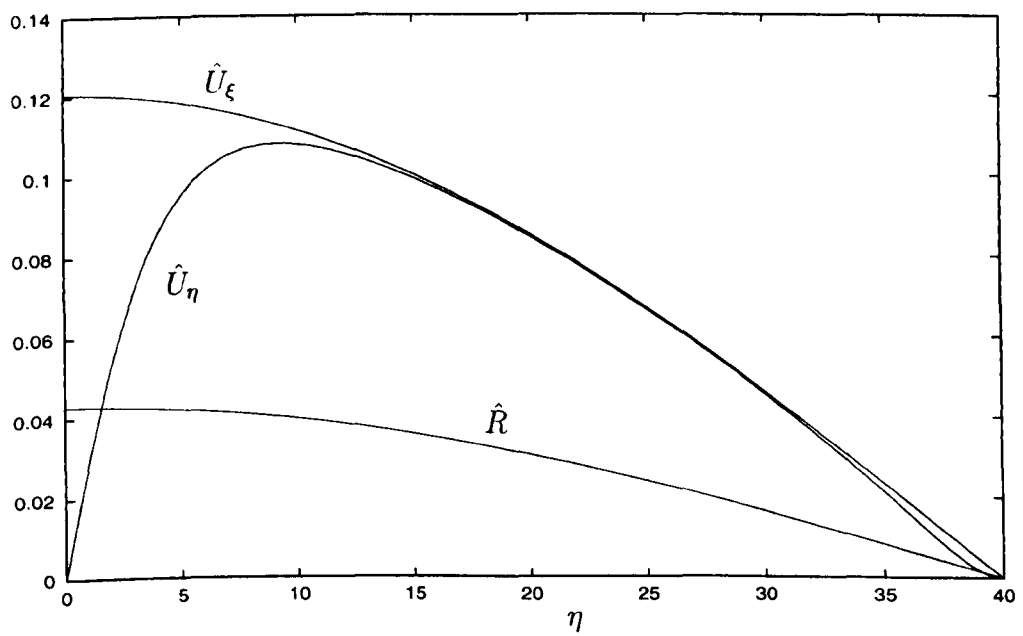

Figure 4.12: Plot of the eigenfunctions $\hat{U}_\eta$, $\hat{U}_\xi$ and $\hat{R}$ for the parameter values $C = 0$, $A = \pi/4$, $R_e = 1$, $P_e = 2 \times 10^4$, $\alpha = 0.5$ and $L = 40$ in Example 5.

Chapter 5

Linear Stability of a Ridge of Fluid

5.1 Introduction

In Chapters 2 and 3 the stability analysis was restricted to uniform perturbations for the two-dimensional cases and axisymmetric perturbations for the three-dimensional cases. In this Chapter we investigate the linear stability to perturbations with variation in the transverse direction of an initially two-dimensional thin ridge of Newtonian fluid of finite width on a horizontal planar substrate acting under the influence of a jet of air normal to the substrate. Two problems are considered: the special case when the jet acts at the centre of the ridge (which in two dimensions corresponds to the planar non-annular problem studied in Chapter 2) and the more general case when the jet acts off-centre (which in two dimensions corresponds to the planar annular problem studied in Chapter 3). For both problems we confirm and extend the corresponding analytical results of Chapters 2 and 3 in the special case of quasi-static motion (corresponding to zero capillary number) and investigate numerically the general case of non-zero capillary number using the numerical code described in Chapter 4. The linear stability of an initially axisymmetric thin drop to both axisymmetric and non-axisymmetric perturbations is considered in Chapter 6.

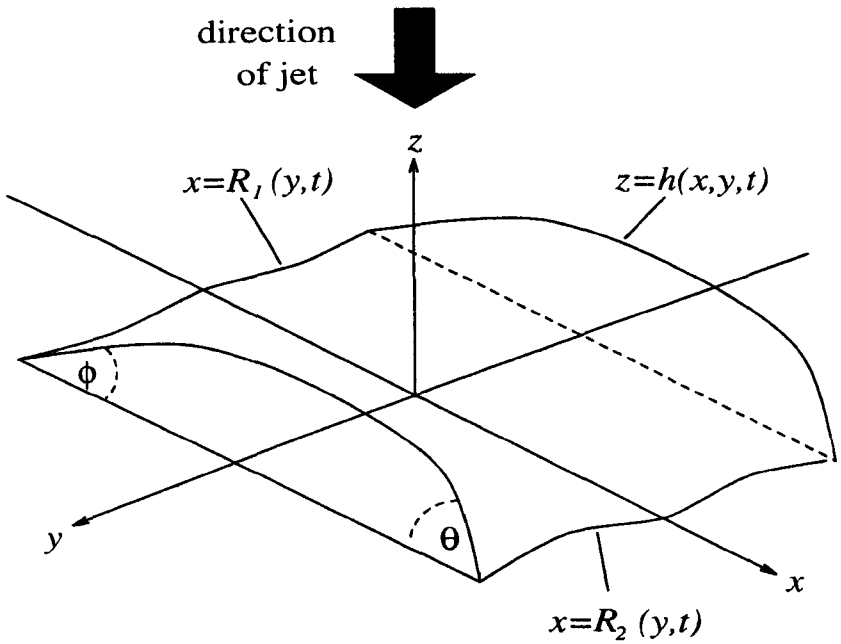

Figure 5.1: Geometry of the problem.

5.2 Problem Formulation

Consider a ridge of incompressible Newtonian fluid of finite width with constant viscosity μ, density ρ and surface tension τ on a solid horizontal planar substrate in the presence of a jet of air. We employ Cartesian coordinates (x, y, z), chosen so that the substrate is given by $z = 0$, the thickness of the fluid film is denoted by $z = h(x, y, t)$ and the velocity of the fluid is denoted by $\mathbf{u} = \mathbf{u}(x, y, z, t)$. The positions of the contact lines are denoted by $x = R_1(y, t)$ at which the contact angle is $\phi = \phi(t)$ and $x = R_2(y, t) > R_1$ at which the contact angle is $\theta = \theta(t)$, where t denotes time. We model the jet as before with a parabolic pressure distribution in the air given by $P = p_0 - kx^2/2$, where P denotes the pressure, p_0 is the maximum value of the air pressure at $x = 0$ and k is a positive constant. The shear stress at the free surface caused by the jet is again neglected. The geometry of the problem is shown in Fig. 5.1.

As in Chapters 2 and 3 we follow the approach pioneered by Greenspan [16] and Ehrhard & Davis [10] and assume that the speeds of the contact lines are

related to their contact angles by the Tanner Laws

$$(R_1)_t = \kappa(\phi_0^m - \phi^m), \tag{5.1}$$

$$(R_2)_t = \kappa(\theta^m - \theta_0^m), \tag{5.2}$$

where ϕ_0 and θ_0 are the equilibrium contact angles and κ is an empirically-determined positive constant with dimensions of velocity. More general Tanner Laws are used in Chapters 2 and 3.

From the results given in Chapter 1 the familiar lubrication approximation to the governing Navier-Stokes and mass conservation equations yield

$$0 = p_z + \rho g, \tag{5.3}$$

$$\mu u_{zz} = p_x, \tag{5.4}$$

$$\mu v_{zz} = p_y, \tag{5.5}$$

$$u_x + v_y + w_z = 0, \tag{5.6}$$

where g denotes acceleration due to gravity, subject to the boundary conditions

$$u = \lambda u_z, \quad v = \lambda v_z \quad \text{on} \quad z = 0, \tag{5.7}$$

$$\mu u_z = 0, \quad \mu v_z = 0 \quad \text{on} \quad z = h, \tag{5.8}$$

$$p = p_0 - \frac{kx^2}{2} - \tau\nabla^2 h \quad \text{on} \quad z = h, \tag{5.9}$$

$$w = h_t + uh_x + vh_y \quad \text{on} \quad z = h, \tag{5.10}$$

where the fluid velocity has been written $\mathbf{u}=(u, v, w)$. Equation (5.7) is the slip condition that mitigates the stress singularity at the contact line. In the simple Navier slip model used here the slip coefficient λ is a (small) positive constant with the dimensions of length. Equation (5.8) represents zero tangential stress at the free surface and Eq. (5.9) is the normal stress condition which includes both the effects of surface tension and the non-uniform external pressure loading caused by the jet of air. Equation (5.10) is the kinematic free-surface condition which can be used with Eq. (5.6) to derive the flux condition

$$h_t + (Q_1)_x + (Q_2)_y = 0, \tag{5.11}$$

where Q_1 and Q_2 denote the fluxes in the x and y directions respectively defined by

$$Q_1 = \int_0^h u\,\mathrm{d}z, \qquad Q_2 = \int_0^h v\,\mathrm{d}z. \tag{5.12}$$

Solving Eqs. (5.3) – (5.9) for u and v allows Q_1 and Q_2 to be evaluated explicitly, and substituting these expressions into Eq. (5.11) gives the governing equation for h.

We non-dimensionalise the problem using a characteristic horizontal length scale L (to be defined subsequently) and κ as the characteristic horizontal velocity scale. The corresponding non-dimensional variables are defined by $x = Lx'$, $y = Ly'$, $h = \theta_0 Lh'$, $R_1 = \theta_0^m LR_1'$, $R_2 = \theta_0^m LR_2'$, $t = Lt'/\kappa$, $\phi = \theta_0\phi'$, $\phi_0 = \theta_0\phi_0'$ and $\theta = \theta_0\theta'$. Dropping the primes at once for simplicity we obtain the non-dimensional version of the governing equation for h, namely

$$\begin{aligned} Ch_t + \left[h^2\left(\frac{h}{3}+\lambda\right)\left((\nabla^2 h)_x - G^2 h_x + Jx\right)\right]_x \\ + \left[h^2\left(\frac{h}{3}+\lambda\right)\left((\nabla^2 h)_y - G^2 h_y\right)\right]_y = 0, \end{aligned} \tag{5.13}$$

together with the non-dimensional versions of Eqs. (5.1) and (5.2), namely,

$$(R_1)_t = \phi_0^m - \phi^m, \tag{5.14}$$

$$(R_2)_t = \theta^m - 1, \tag{5.15}$$

where the constants J, C and G are as defined previously. The appropriate boundary conditions for Eq. (5.13) are

$$h(R_1, y, t) = 0, \tag{5.16}$$

$$h(R_2, y, t) = 0, \tag{5.17}$$

$$(h_x - (R_1)_y h_y)(1 + (R_1)_y^2)^{-\frac{1}{2}}|_{x=R_1} = \phi, \tag{5.18}$$

$$(h_x - (R_2)_y h_y)(1 + (R_2)_y^2)^{-\frac{1}{2}}|_{x=R_2} = -\theta, \tag{5.19}$$

which must be satisfied together with appropriate initial conditions for h, R_1 and R_2. Note that if we set $h = h(x)$ and $\lambda = 0$ in Eq. (5.13) we recover Eq. (2.11)(p) from Chapter 2. Equations (5.16) and (5.17) require the free surface to have zero

height at the contact lines while Eqs. (5.18) and (5.19) ensure that the contact angles take the correct values. The volume of fluid in a width $2d$ of the ridge is given by

$$2dV = \int_{-d}^{d}\int_{R_1}^{R_2} h\,\mathrm{d}x\mathrm{d}y. \tag{5.20}$$

Without loss of generality we can choose $L = (\tau\theta_0/k)^{1/3}$ (corresponding to setting $J = 1$). For clarity we shall retain J explicitly in all of our analytical calculations but set $J = 1$ in all of our numerical calculations.

In what follows we shall restrict our attention to the special case $G = 0$ when gravity effects are negligible. In addition we follow Greenspan [16] and Hocking & Miksis [23] and adopt a linear Tanner Law, obtained by setting $m = 1$ in Eqs. (5.14) and (5.15).

5.2.1 Basic State

In equilibrium $h(x,y,t) = h_0(x)$, $R_1(y,t) = R_1^0$, $R_2(y,t) = R_2^0$, $\theta = 1$ and $\phi = \phi_0$. Substituting these expressions into Eqs. (5.13), (5.16), (5.17) and (5.19) with $G = 0$ yields the governing equation for the basic state, namely

$$h_0''' + Jx = 0, \tag{5.21}$$

where the prime denotes differentiation with respect to x, subject to the boundary conditions

$$h_0(R_1^0) = 0, \tag{5.22}$$

$$h_0(R_2^0) = 0, \tag{5.23}$$

$$h_0'(R_2^0) = -1. \tag{5.24}$$

The solution for h_0 is given by

$$h_0 = (R_2^0 - x)(x - R_1^0)\left\{\frac{J}{24}[x^2 + (R_1^0 + R_2^0)x - R_2^0(2R_2^0 + R_1^0)] + \frac{1}{R_2^0 - R_1^0}\right\}. \tag{5.25}$$

From Eq. (5.20) the volume of the ridge is given by

$$V = \frac{1}{6}(R_2^0 - R_1^0)^2 - \frac{J}{360}(R_2^0 - R_1^0)^4(2R_1^0 + 3R_2^0), \tag{5.26}$$

while from the remaining boundary condition Eq. (5.18) we obtain the relationship between ϕ_0, R_1^0 and R_2^0, namely

$$\phi_0 = 1 - \frac{J}{12}(R_2^0 + R_1^0)(R_2^0 - R_1^0)^2. \tag{5.27}$$

Note that Eq. (5.27) implies that solutions are possible only if $0 \leq \phi_0 \leq 1$.

5.2.2 Linear Stability Problem

In order to analyse the linear stability of the ridge to small perturbations in the transverse direction with wavenumber q we write $h = h_0(x) + h_1(x)\exp(iqy + \sigma t)$, $R_1 = R_1^0 + R_1^1 \exp(iqy + \sigma t)$ and $R_2 = R_2^0 + R_2^1 \exp(iqy + \sigma t)$, where $h_1(x)$ is the perturbation to the basic-state profile, R_1^1 and R_2^1 are the perturbations to the positions of the contact lines and σ is the unknown (complex) growth coefficient. Substituting these expressions into Eqs. (5.13) – (5.19) and retaining only first-order terms in the perturbations yields the governing equation for h_1:

$$C\sigma h_1 + \left[h_0^2\left(\frac{h_0}{3} + \lambda\right)(h_1'' - q^2 h_1)'\right]' - q^2 h_0^2\left(\frac{h_0}{3} + \lambda\right)(h_1'' - q^2 h_1) = 0, \tag{5.28}$$

which is subject to the boundary conditions

$$R_1^1 = -\frac{1}{\phi_0} h_1(R_1^0), \tag{5.29}$$

$$R_2^1 = h_1(R_2^0), \tag{5.30}$$

$$h_1'(R_1^0) + h_0''(R_1^0)R_1^1 = -\sigma R_1^1, \tag{5.31}$$

$$h_1'(R_2^0) + h_0''(R_2^0)R_2^1 = -\sigma R_2^1. \tag{5.32}$$

Eliminating R_1^1 and R_2^1 from Eqs. (5.29) – (5.32) and using Eq. (5.25) yields

$$\phi_0 h_1'(R_1^0) - f_1(J, R_1^0, R_2^0)h_1(R_1^0) = \sigma h_1(R_1^0), \tag{5.33}$$

$$h_1'(R_2^0) + f_2(J, R_1^0, R_2^0)h_1(R_2^0) = -\sigma h_1(R_2^0), \tag{5.34}$$

where the functions $f_1(J, R_1^0, R_2^0)$ and $f_2(J, R_1^0, R_2^0)$ are given by

$$f_1(J, R_1^0, R_2^0) = \frac{J}{12}(R_2^0 - R_1^0)(5R_1^0 + 3R_2^0) - \frac{2}{R_2^0 - R_1^0}, \tag{5.35}$$

$$f_2(J, R_1^0, R_2^0) = \frac{J}{12}(R_1^0 - R_2^0)(R_1^0 + 3R_2^0) - \frac{2}{R_2^0 - R_1^0}. \tag{5.36}$$

As Hocking & Miksis [23] point out, in the special case $q = 0$ (but *not* otherwise) it is also necessary to impose the volume condition

$$\int_{R_1^0}^{R_2^0} h_1 \mathrm{d}x = 0, \tag{5.37}$$

as an additional condition.

5.3 The Centred Jet ($\phi_0 = 1$)

Substituting $\phi_0 = 1$ into Eq. (5.27) yields the solution $R_1^0 = -R_2^0$. Hence the special case of equal contact angles corresponds to the case when the jet acts at the centre of the ridge.

5.3.1 Basic State

Setting $R_0 = -R_1^0 = R_2^0$ in Eq. (5.25) we obtain the basic state solution

$$h_0 = \frac{1}{24R_0}(x^2 - R_0^2)\left[JR_0(R_0^2 - x^2) - 12\right], \tag{5.38}$$

and from Eq. (5.26) the volume of the ridge is given by

$$V = \frac{2}{45}R_0^2(15 - JR_0^3). \tag{5.39}$$

Figure 5.2 plots basic-state profiles for $R_0 = 0.6$, 1, 1.4, 1.8 and 2.2. These solutions are exactly the two-dimensional non-annular solutions described in Chapter 2. Note that "physical" solutions (i.e. solutions for which $h_0 \geq 0$ over the entire interval $-R_0 \leq x \leq R_0$) exist only when R_0 lies in the range $0 \leq R_0 \leq (12/J)^{1/3}$.

5.3.2 Linear Stability Problem

The governing equation for h_1 is given by Eq. (5.28) subject to the boundary conditions

$$h_1'(-R_0) + \left(\frac{JR_0^3 + 3}{3R_0}\right) h_1(-R_0) = \sigma h_1(-R_0), \tag{5.40}$$

$$h_1'(R_0) - \left(\frac{JR_0^3 + 3}{3R_0}\right) h_1(R_0) = -\sigma h_1(R_0). \tag{5.41}$$

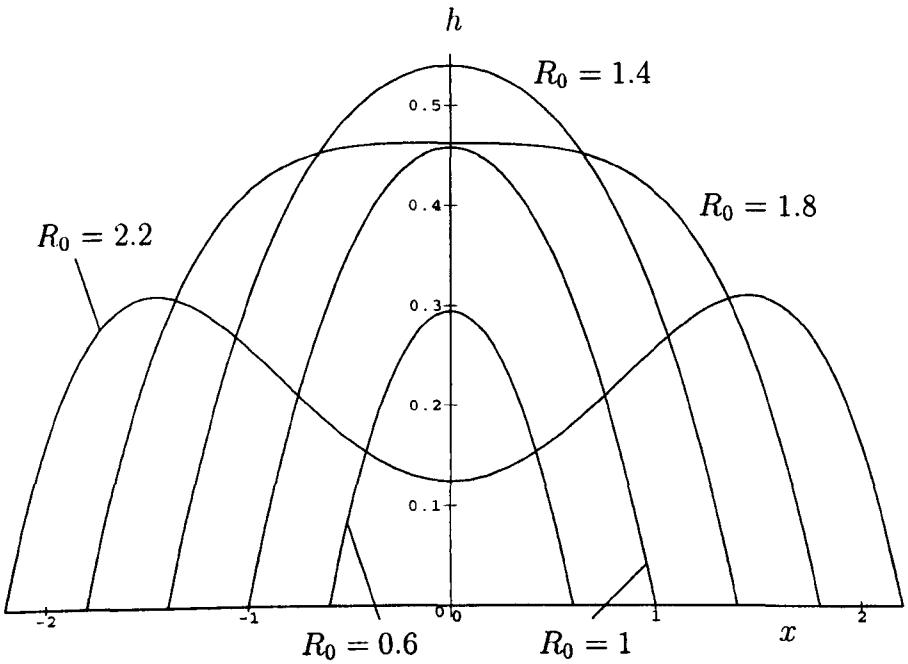

Figure 5.2: Basic-state profiles of the ridge for the centred-jet problem for $R_0 = 0.6$, 1, 1.4, 1.8 and 2.2.

As we have already seen, in the special case $q = 0$ it is also necessary to impose the volume condition

$$\int_{-R_0}^{R_0} h_1 \mathrm{d}x = 0. \tag{5.42}$$

5.3.3 Quasi-static Motion $C = 0$

We can make considerable analytical progress in the special case of quasi-static motion, corresponding to $C = 0$. Note that all the analytical results presented here have been confirmed by numerical calculations of the kind described in the next section.

Two-dimensional Perturbations $q = 0$

Substituting $C = 0$ and $q = 0$ into Eq. (5.28) and integrating once yields

$$h_0^2(h_0 + 3\lambda)h_1''' = Q^*, \tag{5.43}$$

where Q^* is a constant. The general solution of Eq. (5.43) can be written in the form

$$h_1 = Q^* f(x, J, R_0) + \alpha x^2 + \beta x + \gamma, \tag{5.44}$$

where α, β and γ are constants and the function $f(x, J, R_0)$ is not given here explicitly for brevity. Since $f(x, J, R_0) \sim (R_0 - x)\ln(R_0 - x)/3\lambda$ as $x \to R_0^-$ solutions for h_1 that do not have a singularity at $x = R_0$ are possible only if $Q^* = 0$. Thus the appropriate solution for h_1 is simply

$$h_1 = \alpha x^2 + \beta x + \gamma, \tag{5.45}$$

and imposing the volume condition (5.42) on Eq. (5.45) yields $\alpha = -3\gamma/R_0^2$. Evidently the solutions for h_1 can be either symmetric or antisymmetric. For symmetric solutions ($\beta = 0$) applying the boundary condition (5.41) to Eq. (5.45) yields $\sigma = \sigma_{s0}$, where

$$\sigma_{s0} = \frac{JR_0^3 - 6}{3R_0}, \tag{5.46}$$

recovering the expression for the growth rate of symmetric modes obtained in Chapter 2. For antisymmetric solutions ($\alpha = \gamma = 0$) applying the boundary condition (5.41) to Eq. (5.45) yields $\sigma = \sigma_{a0}$, where

$$\sigma_{a0} = \frac{JR_0^2}{3} > 0. \tag{5.47}$$

Figure 5.3 plots σ_{s0} and σ_{a0} as functions of R_0. Note that since $\sigma_{a0} > \sigma_{s0}$ and $\sigma_{a0} > 0$ the conditionally stable symmetric mode considered in Chapter 2 is always more stable than the unconditionally unstable antisymmetric mode considered here for the first time.

Three-dimensional Perturbations $q > 0$

In the general case $q > 0$ a solution of Eq. (5.28) for h_1 with $C = 0$ that does not have a singularity at $x = R_0$ is given by

$$h_1 = \alpha\cosh(qx) + \beta\sinh(qx), \tag{5.48}$$

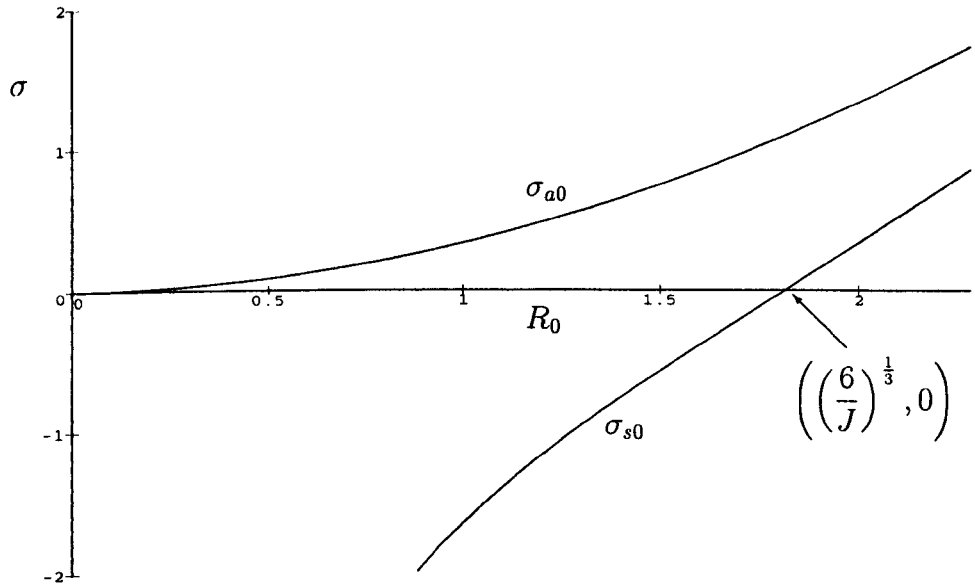

Figure 5.3: Plot of the growth rates of symmetric (σ_{s0}) and antisymmetric (σ_{a0}) perturbations as functions of R_0 for the centred-jet problem in the case $q = 0$ and $C = 0$.

where α and β are constants. Again, the solutions for h_1 can be either symmetric or antisymmetric. The growth rate of symmetric modes ($\beta = 0$) is given by

$$\sigma_s = \frac{JR_0^3 + 3}{3R_0} - q\tanh(qR_0). \tag{5.49}$$

Note that $\sigma_s \to \hat{\sigma}_{s0}$ as $q \to 0$, where $\hat{\sigma}_{s0} = (JR_0^3 + 3)/3R_0 \neq \sigma_{s0}$, i.e. because these solutions do not satisfy the volume condition (5.42) we do not recover the solution obtained previously in the case $q = 0$ in the limit $q \to 0$. The growth rate of antisymmetric modes ($\alpha = 0$) is given by

$$\sigma_a = \frac{JR_0^3 + 3}{3R_0} - q\coth(qR_0). \tag{5.50}$$

Note that $\sigma_a \to \hat{\sigma}_{a0}$ as $q \to 0$, where $\hat{\sigma}_{a0} = JR_0^2/3 = \sigma_{a0}$, i.e. because these solutions do satisfy the volume condition (5.42) we recover the solution obtained previously in the case $q = 0$ in the limit $q \to 0$. The neutral stability curves for $q > 0$ obtained by setting $\sigma_s = 0$ and $\sigma_a = 0$ in Eqs. (5.49) and (5.50) respectively are plotted in Fig. 5.4.

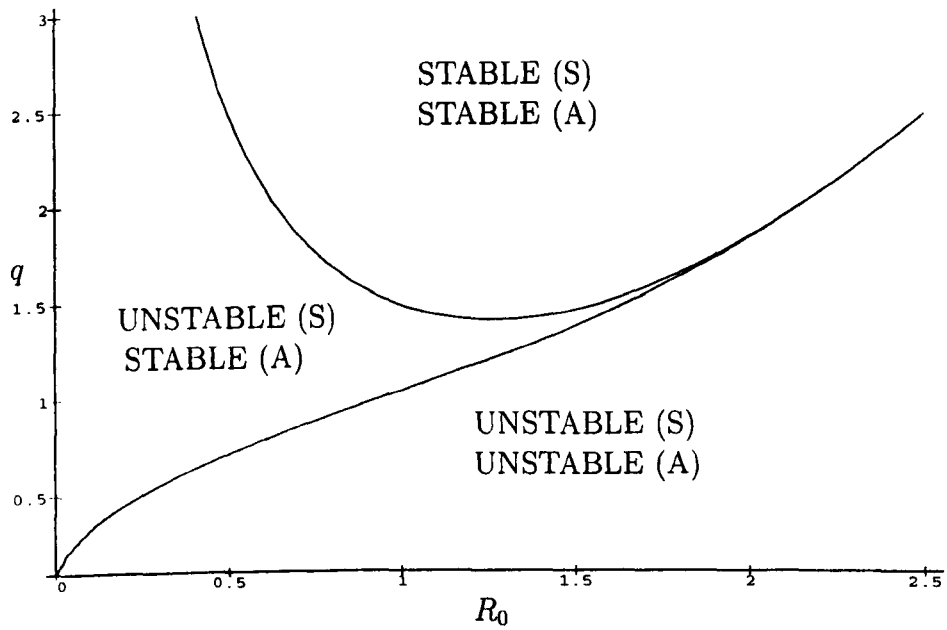

Figure 5.4: Neutral stability curves for symmetric ($\sigma_s = 0$) and antisymmetric ($\sigma_a = 0$) perturbations in the (q,R_0) plane for the centred-jet problem in the case $q > 0$ and $C = 0$. Here (A) denotes antisymmetric modes and (S) symmetric modes.

Figures 5.5(a) – (e) plot the growth rates σ_s and σ_a as functions of $q \geq 0$ for $R_0 = 0.6$, 1, 1.4, 1.8 and 2.2 respectively. Symmetric modes are denoted by solid lines and antisymmetric modes by dashed lines. At $q = 0$, a filled circle denotes a solution, an empty circle no solution. Note that the lower filled circle corresponds to σ_{s0}, i.e. to the symmetric mode obtained in Chapter 2. Since $\sigma_s > \sigma_a$ for $q > 0$, both σ_s and σ_a are monotonically-decreasing functions of q for all $q > 0$, $\hat{\sigma}_{s0} > \hat{\sigma}_{a0} = \sigma_{a0} > \sigma_{s0}$ and $\hat{\sigma}_{s0} > 0$, we deduce that long-wavelength symmetric modes with growth rate approaching $\hat{\sigma}_{s0}$ in the limit $q \to 0$ are always the most unstable when $C = 0$.

5.3.4 The General Case $C \neq 0$

To obtain the neutral stability curves for $C \neq 0$ we set $\sigma = 0$ in Eq. (5.28) and the boundary conditions (5.40) and (5.41). This procedure yields the same neutral stability curves as those calculated previously in the case $C = 0$ as shown in Fig. 5.4. When $\sigma \neq 0$ we must proceed numerically.

Results

Figures 5.6(a) – (e) plot the largest eigenvalues as functions of $q \geq 0$ for R_0=0.6, 1, 1.4, 1.8 and 2.2 respectively in the case $C = 1$. Symmetric modes are denoted by solid lines and antisymmetric modes by dashed lines. At $q = 0$, a filled circle denotes a solution, an empty circle no solution. In all the numerical computations we found that only the two largest eigenvalues ever take positive values, and that one of these eigenvalues always corresponds to symmetric modes and the other always corresponds to antisymmetric modes. Typically both modes are unstable in certain ranges of q, but the nature and location of the most unstable mode (with $\sigma = \sigma^*$ at $q = q^*$) changes as R_0 is varied. As Fig. 5.6(a) shows, when $R_0 = 0.6$ the most unstable mode is symmetric with $\sigma^* \approx 0.0171$ at $q^* \approx 1.41$, but when R_0 increased to 1 the most unstable mode is antisymmetric with $\sigma^* \approx 0.0231$ at $q^* = 0$ (Fig. 5.6(b)). As R_0 is increased further to 1.4 and 1.8 the most unstable mode is still antisymmetric with $\sigma^* \approx 0.0357$ when $R_0 = 1.4$ and $\sigma^* \approx 0.0375$ when $R_0 = 1.8$ at $q^* = 0$ (Figs. 5.6(c) and

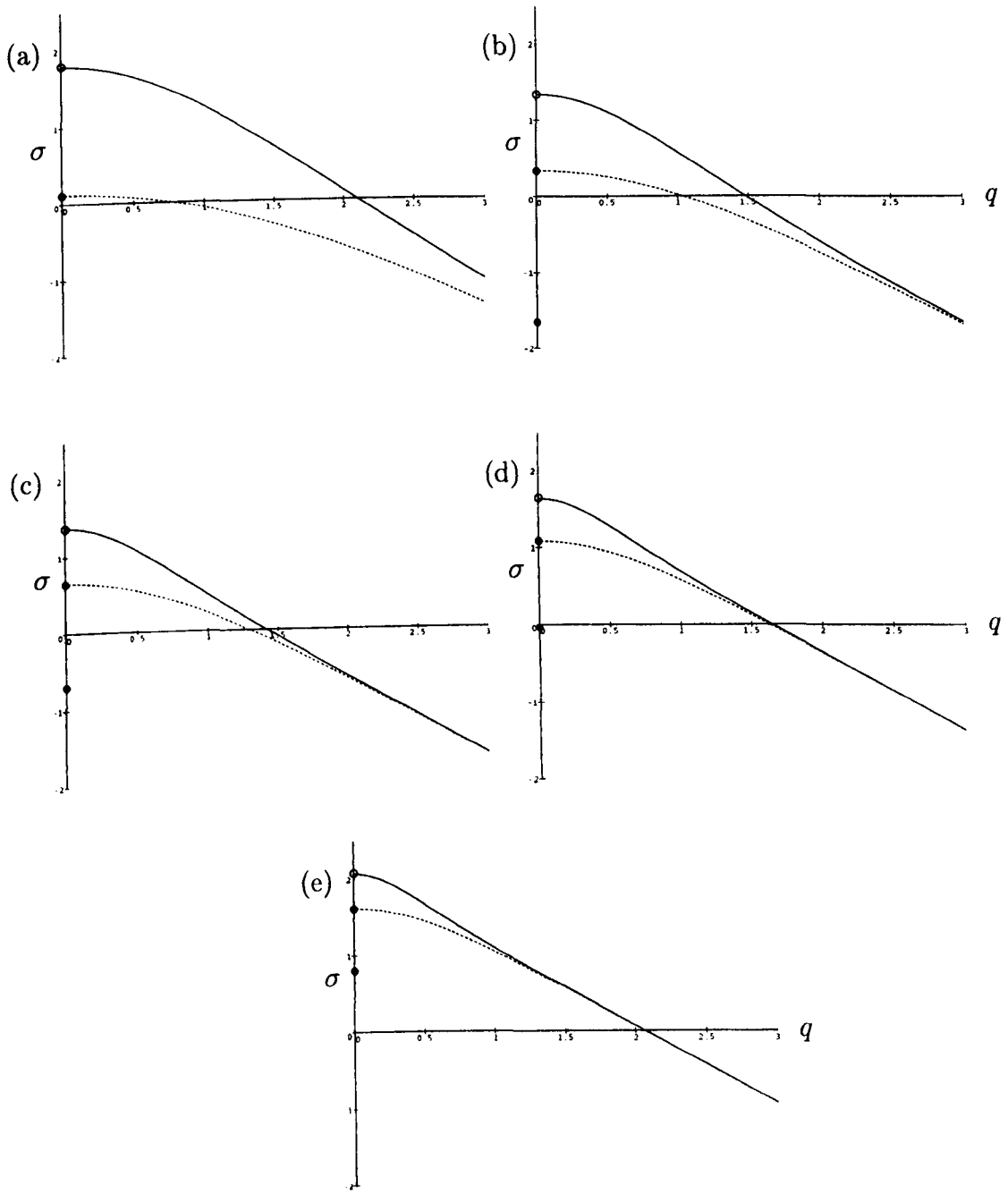

Figure 5.5: (a) (e): Plot of the growth rates of symmetric (σ_s) and antisymmetric (σ_a) perturbations as functions of $q \geq 0$ for the centred-jet problem for $R_0 = 0.6$, 1, 1.4, 1.8 and 2.2 respectively in the case $C = 0$. Symmetric modes are denoted by solid lines and antisymmetric modes by dashed lines. At $q = 0$, a filled circle denotes a solution, an empty circle no solution. Note that the lower solution at $q = 0$ is outwith the range of the plot in (a).

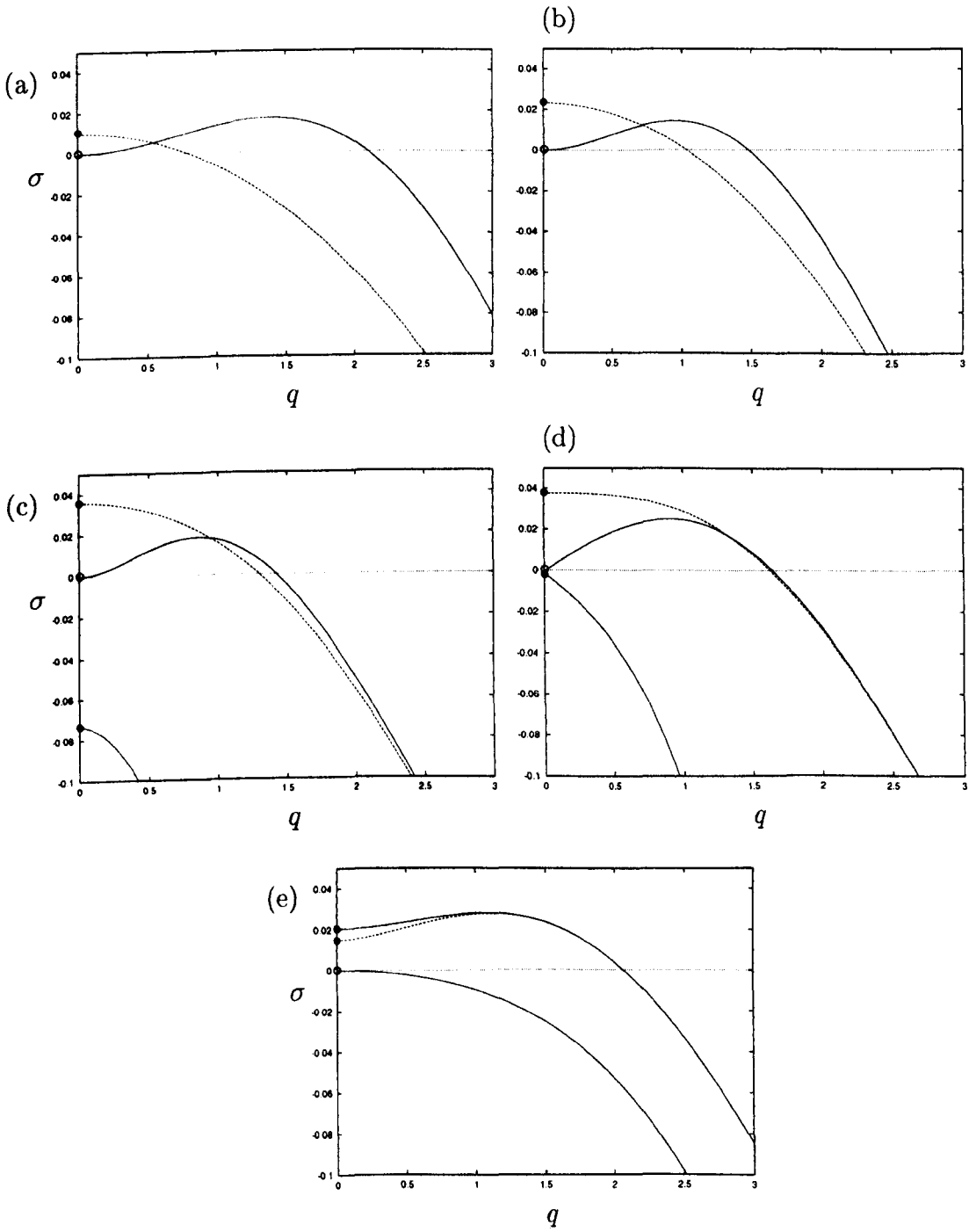

Figure 5.6: (a) (e): Plot of the largest eigenvalues as functions of $q \geq 0$ for the centred-jet problem for $R_0 = 0.6$, 1, 1.4, 1.8 and 2.2 respectively in the case $C = 1$. Symmetric modes are denoted by solid lines and antisymmetric modes by dashed lines. At $q = 0$, a filled circle denotes a solution, an empty circle no solution.

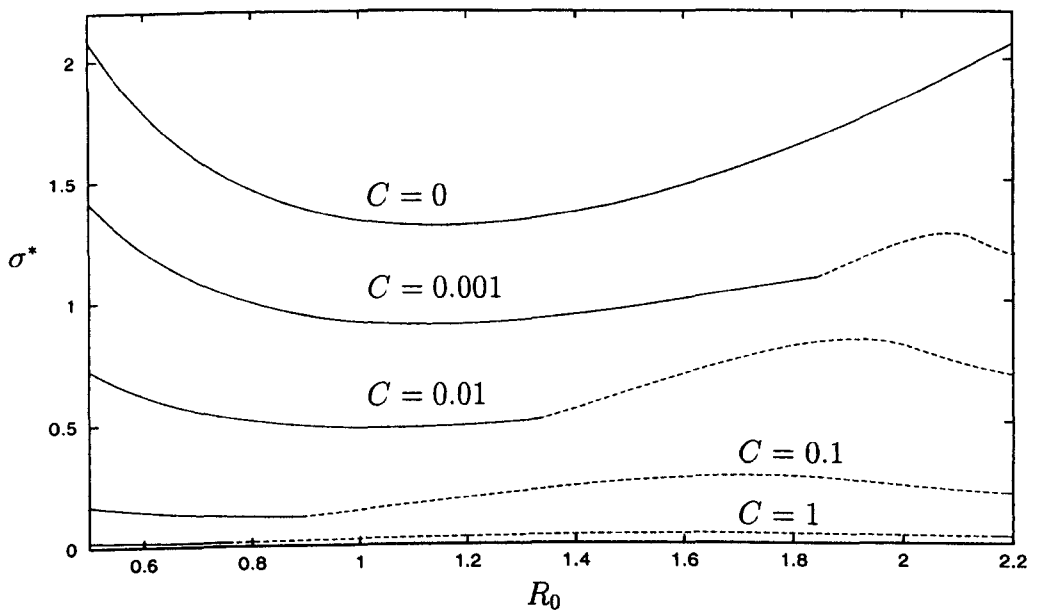

Figure 5.7: Plot of σ^* as a function of R_0 for the centred-jet problem for $C = 1$, 0.1, 0.01, 0.001 and $C = 0$. Symmetric modes are denoted by solid lines and antisymmetric modes by dashed lines.

5.6(d)). However, as Fig. 5.6(e) shows, as R_0 is increased still further to 2.2 the symmetric mode once again becomes the most unstable with $\sigma^* \approx 0.0279$ at $q^* \approx 1.08$. This "switching" between symmetric and antisymmetric modes as R_0 is increased is summarised in Figs. 5.7 and 5.8 which plot σ^* and q^* as functions of R_0 for a range of values of C. For completeness Fig. 5.7 also shows the curve for $\sigma^* = \hat{\sigma}_{s0}$ in the case $C = 0$ which is achieved in the limit $q \to 0$. Note that in both Figs. 5.7 and 5.8 there is a small region near $R_0 = 2.2$ on the curves for $C = 1$ and $C = 0.1$ that corresponds to symmetric modes, but that this region is absent from the curves for $C = 0.01$ and $C = 0.001$. Figure 5.9 plots the largest eigenvalues when $q = 0$ as functions of R_0 for a range of values of C together with the solutions $\sigma_{a0} = JR_0^2/3$ and $\sigma_{s0} = (JR_0^3 - 6)/3R_0$ appropriate in the case $C = 0$. In particular, Fig. 5.9 shows how the numerically-calculated values of σ when $q = 0$ approach σ_{a0} and σ_{s0} in the limit $C \to 0$.

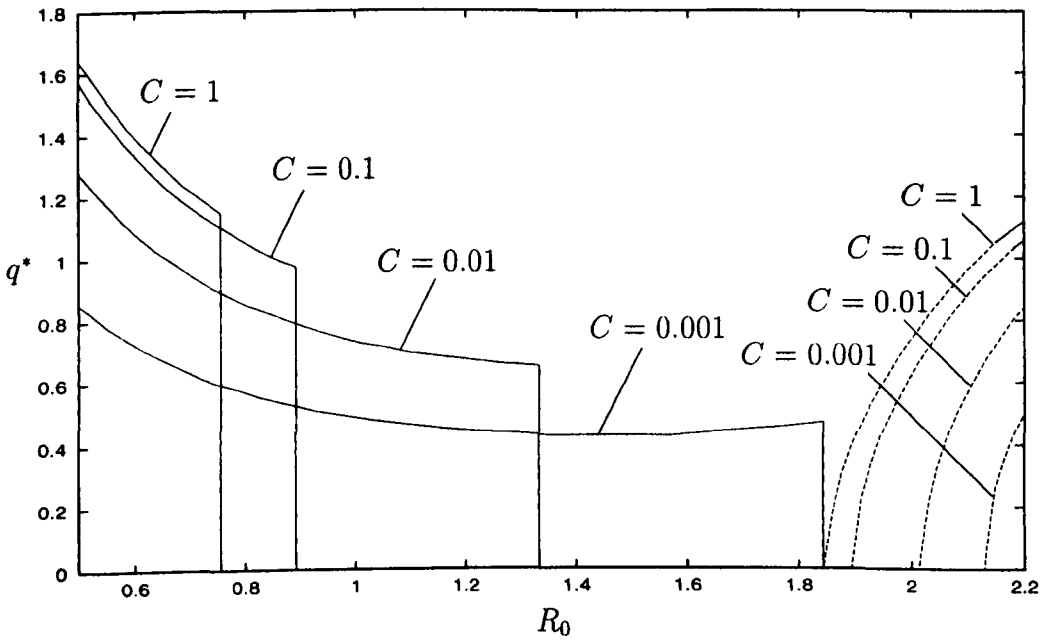

Figure 5.8: Plot of q^* as a function of R_0 for the centred-jet problem for $C = 1$, 0.1, 0.01 and 0.001. Symmetric modes are denoted by solid lines and antisymmetric modes by dashed lines.

5.4 The Off-Centred Jet $0 \leq \phi_0 < 1$

The general case of unequal contact angles ($0 \leq \phi_0 < 1$) corresponds to the case when the jet acts off centre. Since $\phi_0 \neq 1$, solutions of this kind are only possible when the two contact angles in the basic state are different i.e. when the nature of the substrate is different near the two contact lines.

5.4.1 Basic State

The basic-state solution is given by Eq. (5.25) and the volume of the ridge by Eq. (5.26). Figure 5.10 plots basic-state profiles for $R_2^0 = 2$, 2.4, 2.8 and 3.2 in the case $\phi_0 = 0.6$. These solutions are exactly the two-dimensional annular solutions described in Chapter 3. Note that for a given value of ϕ_0 ($0 \leq \phi_0 < 1$), solutions exist only for values of R_2^0 greater than a critical value corresponding to the limiting case in which $R_1^0 = 0$.

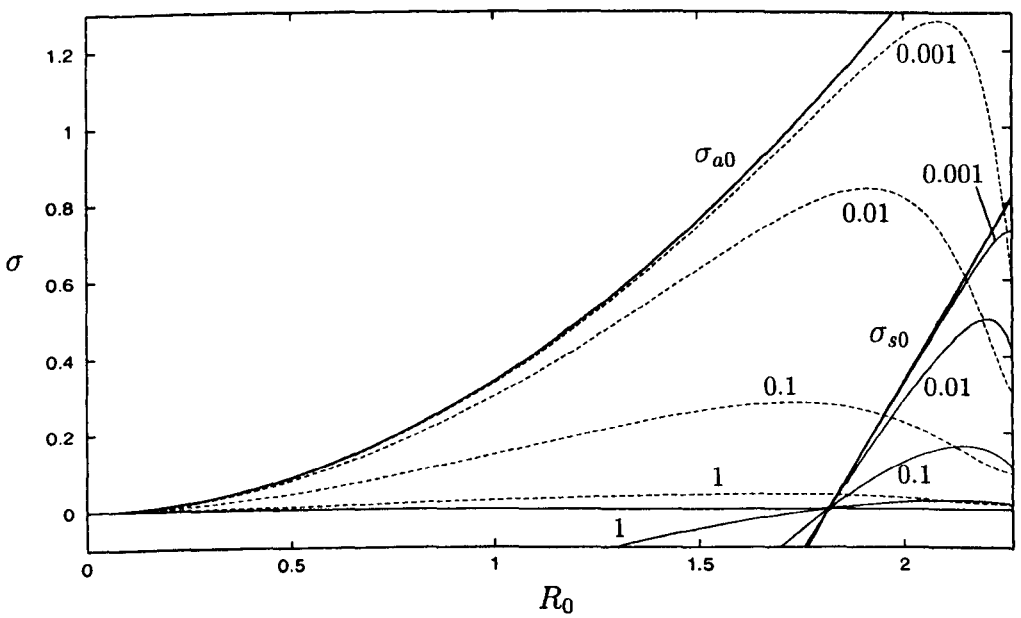

Figure 5.9: Plot of the largest eigenvalues when $q = 0$ as functions of R_0 for the centred-jet problem for $C = 1$, 0.1, 0.01 and 0.001. Symmetric modes are denoted by solid lines and antisymmetric modes by dashed lines. The thin curves denote the eigenvalues obtained numerically when $C \neq 0$ and the thick curves denote the eigenvalues $\sigma_{s0} = (JR_0^3 - 6)/3R_0$ and $\sigma_{a0} = JR_0^2/3$ appropriate in the case $C = 0$.

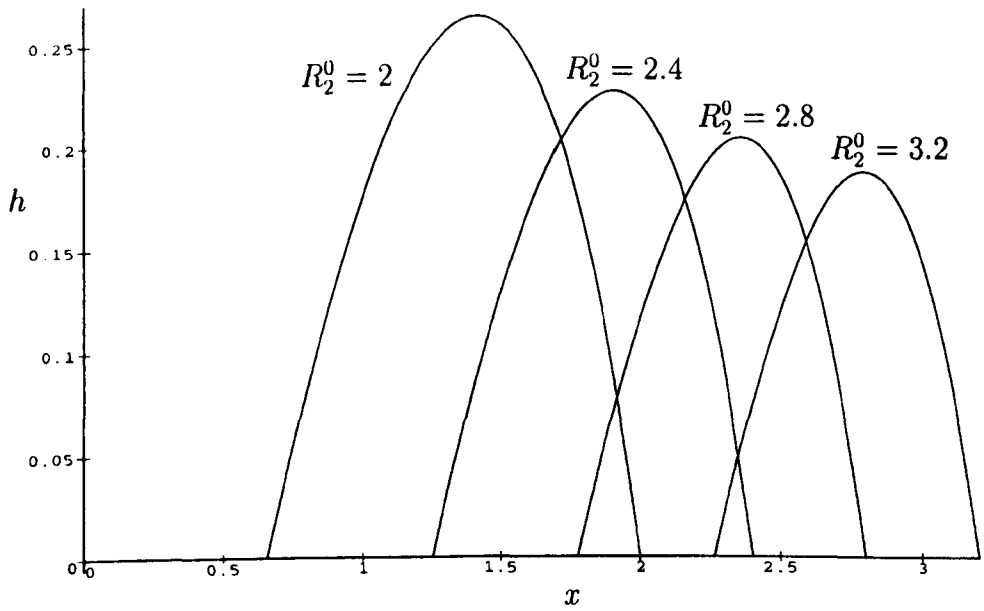

Figure 5.10: Basic-state profiles of the ridge for the off-centred-jet problem for $R_2^0 = 2$, 2.4, 2.8 and 3.2 in the case $\phi_0 = 0.6$.

5.4.2 Linear Stability Problem

The governing equation for h_1 is given by Eq. (5.28) subject to the boundary conditions (5.33) and (5.34). Again in the special case $q = 0$ it is also necessary to impose the volume condition (5.37). Note that in this case all the eigenfunctions are asymmetric.

5.4.3 Quasi-static Motion $C = 0$

As before, we can make considerable analytical progress in the special case of quasi-static motion ($C = 0$). Again all the analytical results presented here have been confirmed by numerical calculations.

Two-dimensional Perturbations $q = 0$

From Sec. 5.3.3 the solution for h_1 when $C = 0$ and $q = 0$ is given by Eq. (5.45). Applying boundary conditions (5.33) and (5.34) and the volume condition (5.37) yields the expressions for the growth rates obtained in Chapter 3, namely $\sigma =$

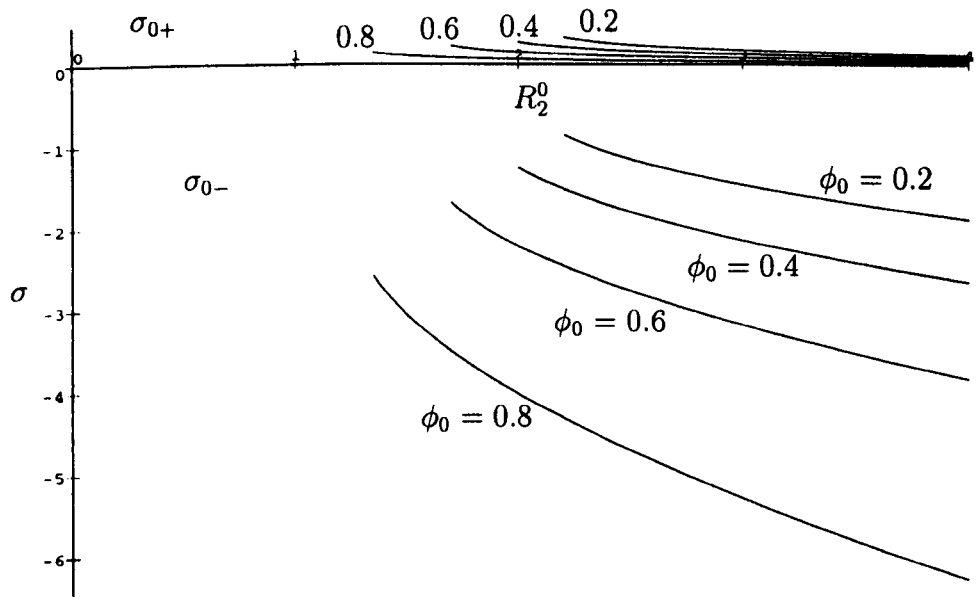

Figure 5.11: Plot of the growth rates σ_{0+} and σ_{0-} as functions of R_2^0 for the off-centred-jet problem for $\phi_0 = 0.2$, 0.4, 0.6 and 0.8 in the case $q = 0$ and $C = 0$.

σ_{0+} and $\sigma = \sigma_{0-}$ where

$$\sigma_{0+} = \frac{J}{12}(R_2^0 - R_1^0)^2 > 0, \tag{5.51}$$

$$\sigma_{0-} = \frac{J}{12}(R_2^0 - R_1^0)(R_1^0 + 3R_2^0) - \frac{4}{R_2^0 - R_1^0}. \tag{5.52}$$

Figure 5.11 plots σ_{0+} and σ_{0-} as functions of R_2^0 for $\phi_0 = 0.2$, 0.4, 0.6 and 0.8. Since $\sigma_{0+} > 0$ the ridge is always unstable when $C = 0$ and $q = 0$. Note that, unlike in the centred-jet case, the analysis in Chapter 3 includes both of the possible modes in this case.

Three-dimensional Perturbations $q > 0$

From Sec. 5.3.3 the solution for h_1 in this case is given by Eq. (5.48) subject to the boundary conditions (5.33) and (5.34). Solving this system yields two expressions for σ, namely σ_{q+} and σ_{q-}, given by

$$\sigma_{q\pm} = \frac{4\zeta(12 - \zeta^2 J R_1^0)\sinh(q\zeta) - 12q\zeta^2(\phi_0 + 1)\cosh(q\zeta) \pm 3\zeta^2 X^{\frac{1}{2}}}{24\zeta^2 \sinh(q\zeta)}, \tag{5.53}$$

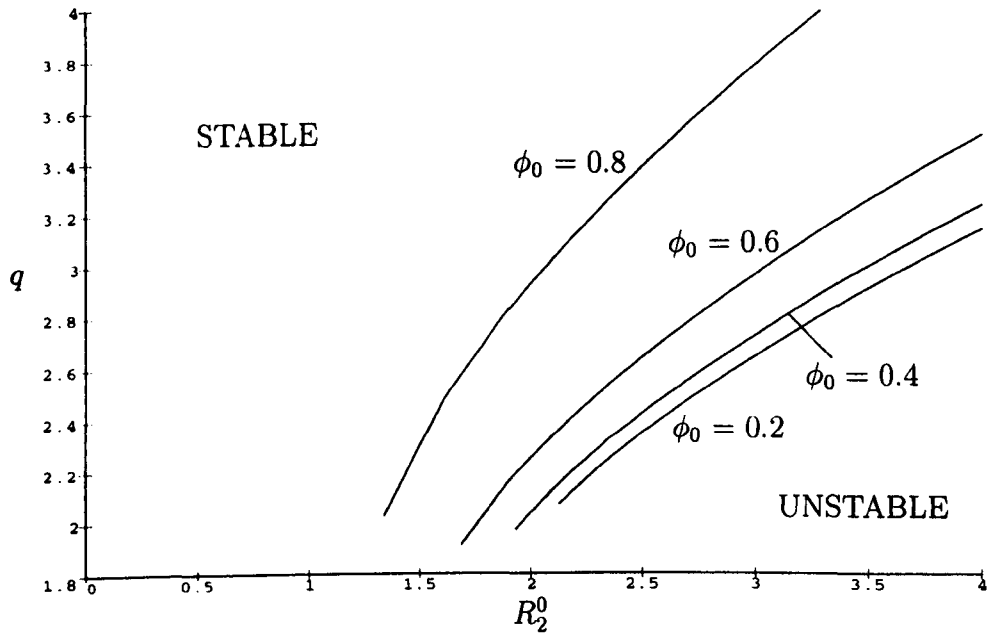

Figure 5.12: Neutral stability curves in the (q,R_2^0) plane corresponding to $\sigma_{q+} = 0$ for the off-centred-jet problem for $\phi_0 = 0.2$, 0.4, 0.6 and 0.8 in the case $q > 0$ and $C = 0$.

where we have written $R_2^0 = R_1^0 + \zeta$ and X is defined to be

$$X = 8q^2(\phi_0^2 + 6\phi_0 + 1) - 2J^2\zeta^2(\zeta + 2R_1^0)^2 + 2[4q^2(\phi_0 - 1)^2 + J^2\zeta^2(\zeta + 2R_1^0)^2]\cosh(2q\zeta) + Jq\zeta(\zeta + 2R_1^0)(\phi_0 - 1)\sinh(2q\zeta). \tag{5.54}$$

In particular, as $q \to 0$ we have $\sigma_{q\pm} \to \hat{\sigma}_{0\pm}$ where

$$\hat{\sigma}_{0\pm} = \frac{6(3 - \phi_0) - 2JR_1^0\zeta^2 \pm 3Y^{\frac{1}{2}}}{12\zeta}, \tag{5.55}$$

where Y is defined to be

$$Y = 4(1 + \phi_0)^2 + 4J\zeta^2(\zeta + 2R_1^0)(\phi_0 - 1) + J^2\zeta^4(\zeta + 2R_1^0)^2. \tag{5.56}$$

Note that $\hat{\sigma}_{0+} \neq \sigma_{0+}$ and $\hat{\sigma}_{0-} \neq \sigma_{0-}$, i.e. because neither of these solutions satisfy the volume condition (5.37) we do not recover the expressions obtained previously in the case $q = 0$ in the limit $q \to 0$. The neutral stability curves for $q > 0$ obtained by setting $\sigma_{q+} = 0$ in Eq. (5.53) are plotted in Fig. 5.12 for $\phi_0 = 0.2$, 0.4, 0.6 and 0.8.

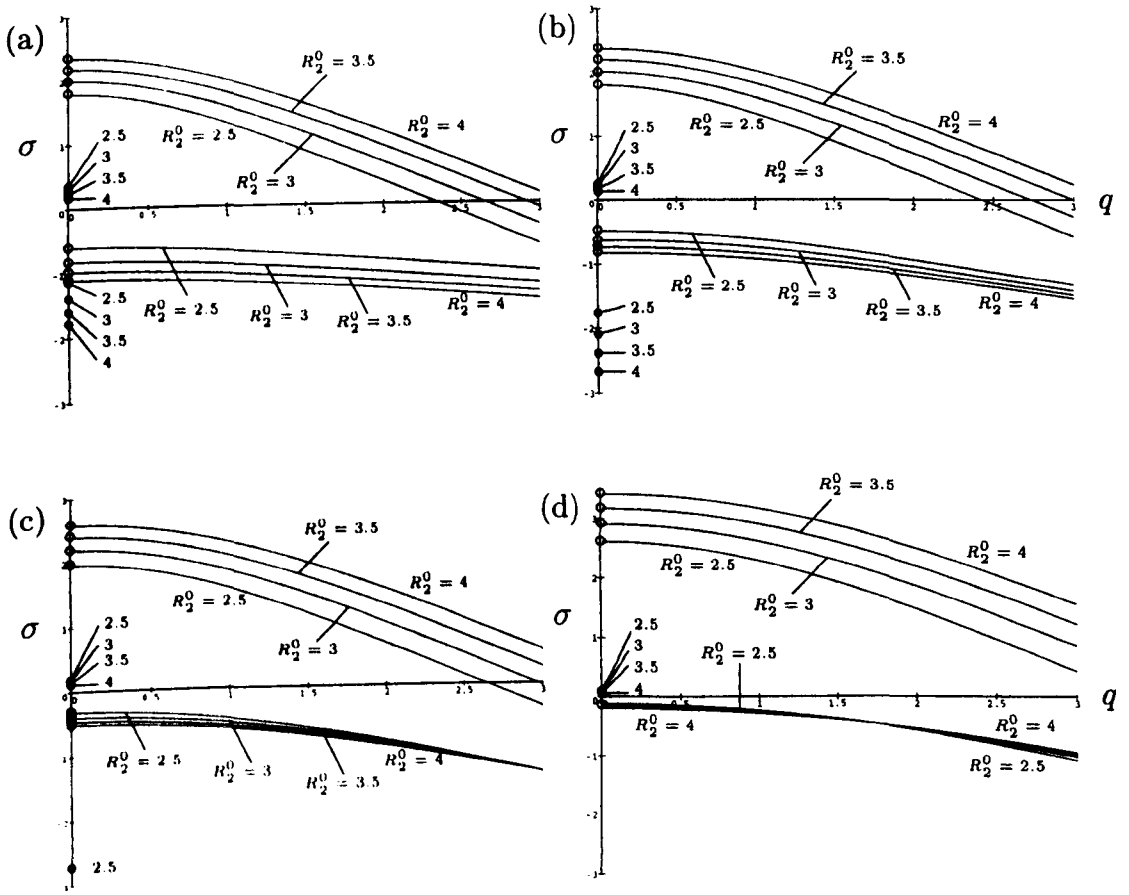

Figure 5.13: (a) (d): Plot of the growth rates σ_{q+} and σ_{q-} as functions of $q \geq 0$ for the off-centred-jet problem for $R_2^0 = 2.5$, 3, 3.5 and 4 for $\phi_0 = 0.2$, 0.4, 0.6 and 0.8 respectively in the case $C = 0$. At $q = 0$, a filled circle denotes a solution, an empty circle no solution.

Figures 5.13(a) – (d) plot the growth rates σ_{q+} and σ_{q-} as functions of $q \geq 0$ for $R_2^0 = 2.5$, 3, 3.5 and 4 for $\phi_0 = 0.2$, 0.4, 0.6 and 0.8 respectively. Note that the filled circles at $q = 0$ correspond to $\sigma_{0\pm}$, i.e. to the modes obtained in Chapter 3. Since $\sigma_{q+} > \sigma_{q-}$ for $q > 0$, both σ_{q+} and σ_{q-} are monotonically-decreasing functions of q for all $q > 0$, $\hat{\sigma}_{0+} > \sigma_{0+} > \hat{\sigma}_{0-} > \sigma_{0-}$ and $\hat{\sigma}_{0+} > 0$, we deduce that long-wavelength symmetric modes with growth rate approaching $\hat{\sigma}_{0+}$ in the limit $q \to 0$ are always the most unstable when $C = 0$.

5.4.4 The General Case $C \neq 0$

To obtain the neutral stability curves when $C \neq 0$ we set $\sigma = 0$ in Eq. (5.28) and the boundary conditions (5.33) and (5.34). This procedure yields the same neutral stability curves as those calculated previously in the case $C = 0$ as shown in Fig. 5.12. Again, when $\sigma \neq 0$ we must proceed numerically.

Figures 5.14(a) – (d) plot the largest eigenvalues as functions of $q \geq 0$ for $R_2^0 = 2.5$, 3, 3.5 and 4 for $\phi_0 = 0.2$, 0.4, 0.6 and 0.8 respectively in the case $C = 1$. As Fig. 5.14 shows, as R_0 is increased the values of $\sigma^* > 0$ and q^* increase and so the ridge is again unconditionally unstable. However, the switching between modes seen in the centred-jet case does not occur in this case. This behaviour is summarised in Figs. 5.15 and 5.16 which plot σ^* and q^* as functions of R_2^0 for a range of values of C. For completeness Fig. 5.15 also shows the curve for $\sigma^* = \hat{\sigma}_{0+}$ in the case $C = 0$ which is achieved in the limit $q \to 0$. Figure 5.17 plots the largest eigenvalues when $q = 0$ as functions of R_2^0 for a range of values of C together with the solutions σ_{0+} and σ_{0-} appropriate in the case $C = 0$. In particular, Fig. 5.17 shows how the numerically-calculated values of σ when $q = 0$ approach σ_{0+} and σ_{0-} in the limit $C \to 0$.

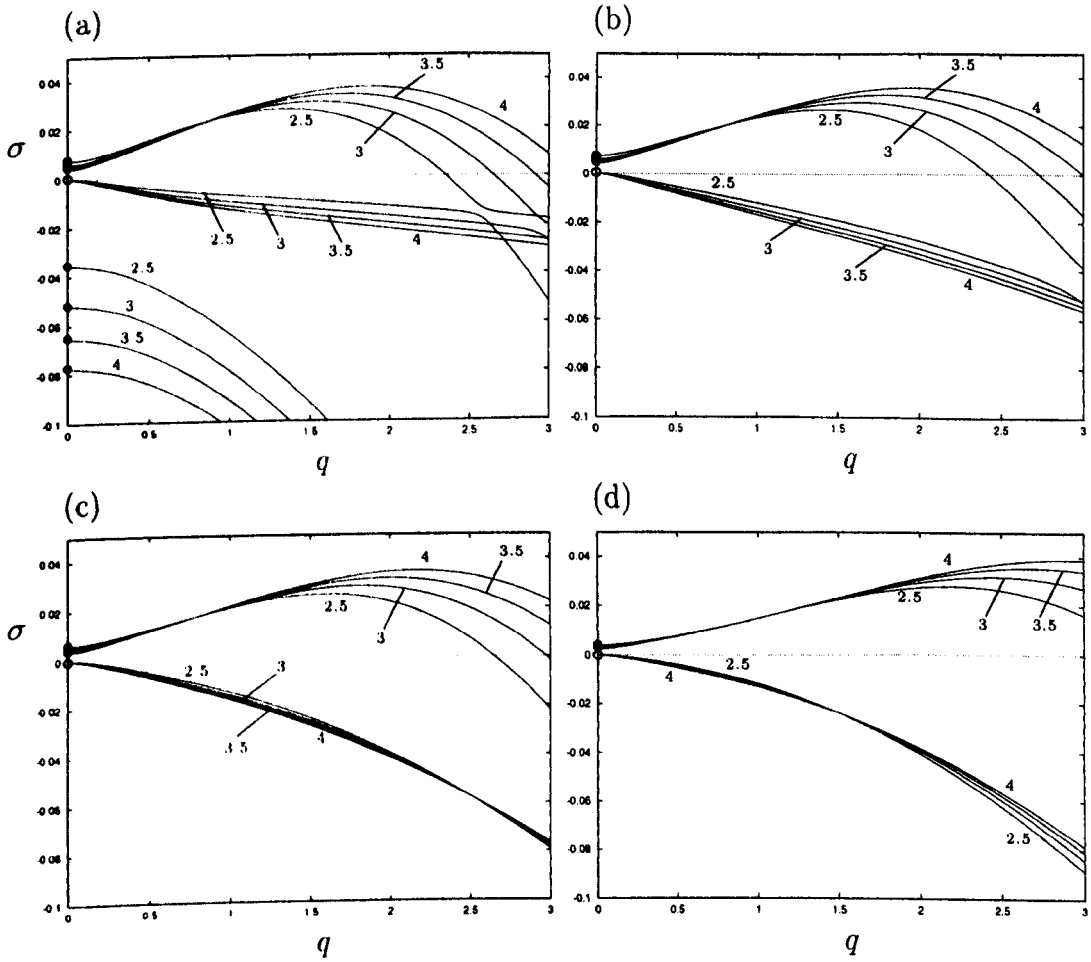

Figure 5.14: (a) (d): Plot of the largest eigenvalues as functions of $q \geq 0$ for the off-centred-jet problem for $R_2^0 = 2.5$, 3, 3.5 and 4 for $\phi_0 = 0.2$, 0.4, 0.6 and 0.8 respectively in the case $C = 1$. At $q = 0$, a filled circle denotes a solution, an empty circle no solution.

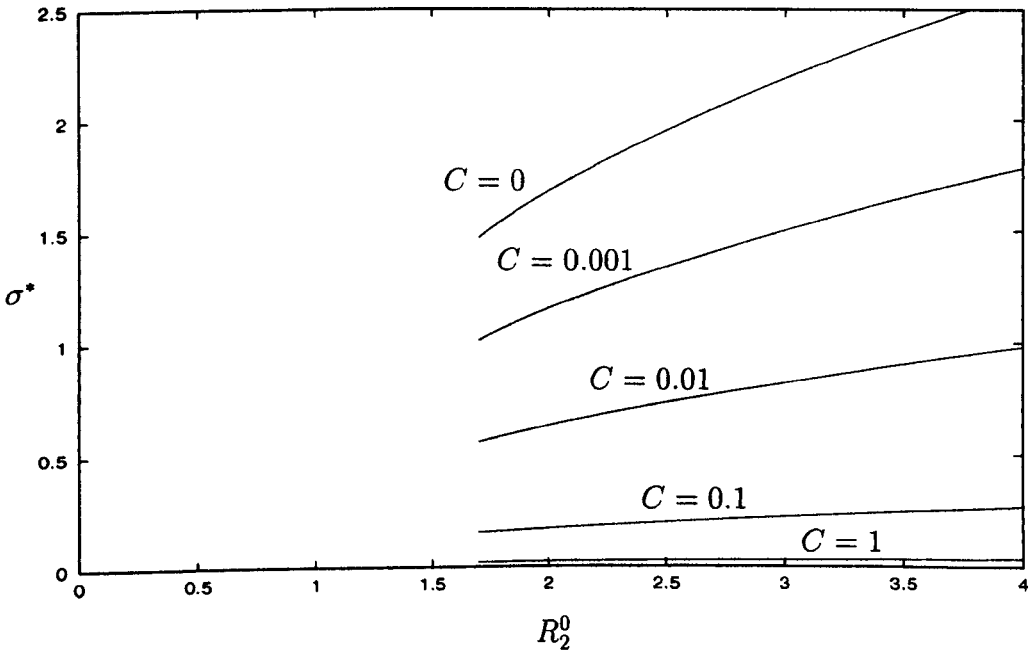

Figure 5.15: Plot of σ^* as a function of R_2^0 for the off-centred-jet problem for $C = 1$, 0.1, 0.01, 0.001 and $C = 0$ in the case $\phi_0 = 0.6$.

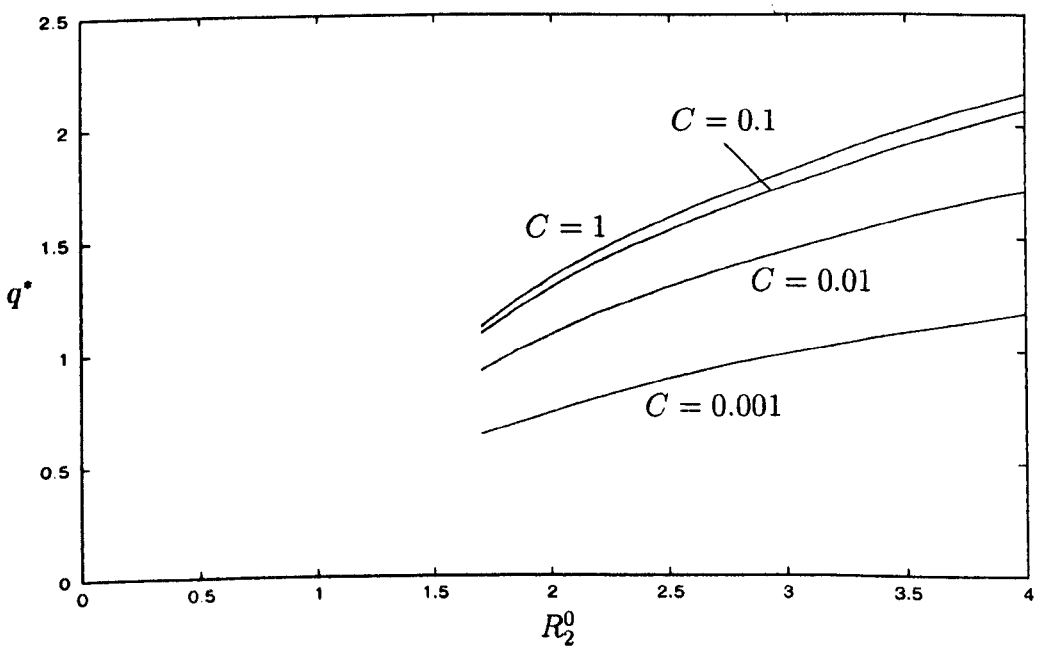

Figure 5.16: Plot of q^* as a function of R_2^0 for the off-centred-jet problem for $C = 1$, 0.1, 0.01 and 0.001 in the case $\phi_0 = 0.6$.

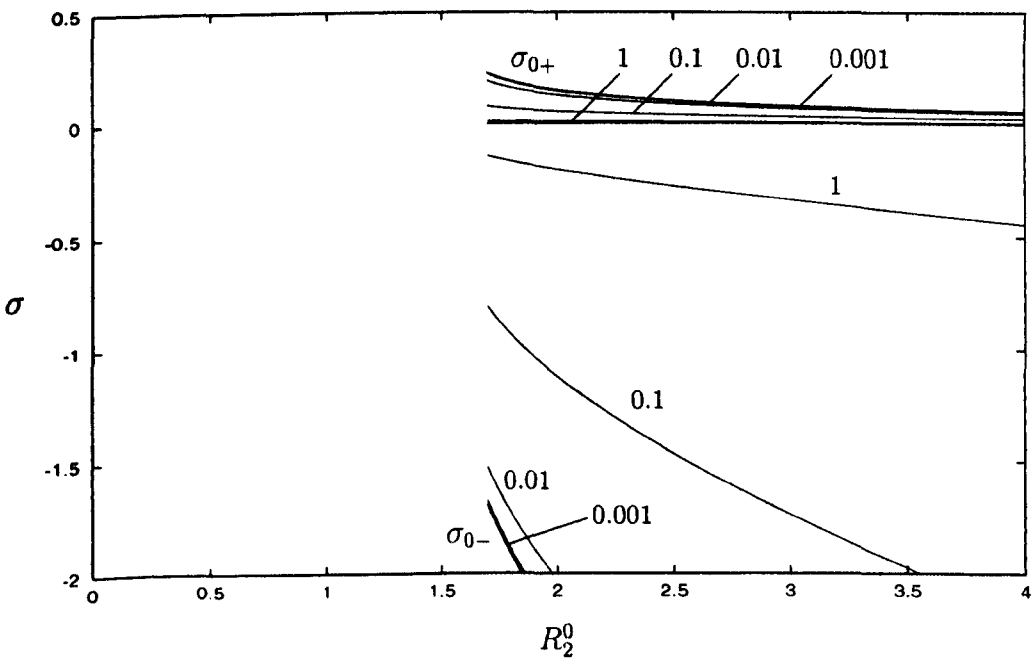

Figure 5.17: Plot of the largest eigenvalues when $q = 0$ as functions of R_2^0 for the off-centred-jet problem for $C = 1$, 0.1, 0.01 and 0.001 in the case $\phi_0 = 0.6$. The thin curves denote the eigenvalues obtained numerically when $C \neq 0$ and the thick curves denote the eigenvalues $\sigma_{0\pm}$ appropriate in the case $C = 0$.

Chapter 6

Linear Stability of a Drop of Fluid

6.1 Introduction

In this Chapter we investigate the linear stability to both axisymmetric and non-axisymmetric perturbations of an initially axisymmetric thin drop of Newtonian fluid either on a uniformly rotating substrate or under the influence of a jet of air directed normally towards a stationary substrate. Following the pattern of Chapter 5, two problems are considered: one in which the drop has no dry patch (a non-annular drop) and one in which the drop has a dry patch at its centre (an annular drop). For each problem we confirm and extend the corresponding analytical results of Chapters 2 and 3 in the special case of quasi-static motion (zero capillary number) and investigate numerically the general case of non-zero capillary number using the numerical code developed in Chapter 4.

6.2 Non-annular Drops

6.2.1 Problem Formulation

Consider a non-annular drop of incompressible Newtonian fluid with constant viscosity μ, density ρ and surface tension τ on a solid horizontal planar substrate in the presence of a jet of air. We employ cylindrical polar coordinates (r, φ, z), chosen so that the substrate is given by $z = 0$, the thickness of the

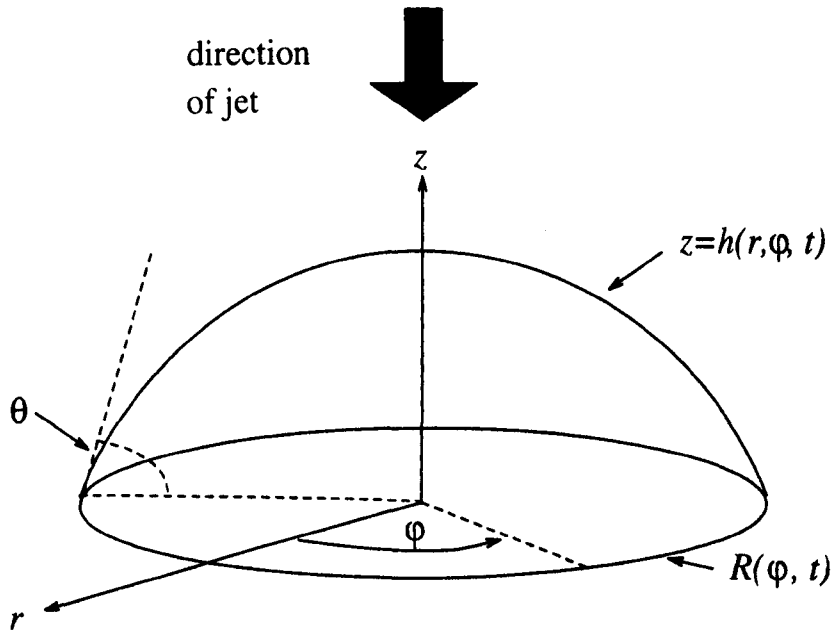

Figure 6.1: Geometry of the non-annular problem.

drop is denoted by $z = h(r, \varphi, t)$ and the velocity of the fluid is denoted by $\mathbf{u} = \mathbf{u}(r, \varphi, z, t)$, where t denotes time. The position of the contact line is denoted by $r = R(\varphi, t)$ at which the contact angle is $\theta = \theta(t)$. We again model the jet with a parabolic pressure distribution in the air given by $P = p_0 - kr^2/2$, where P denotes the pressure, p_0 is the maximum value of the air pressure at $r = 0$ and k is a positive constant. The shear stress at the free surface caused by the jet is again neglected. The geometry of the non-annular problem is shown in Fig. 6.1.

We follow the approach pioneered by Greenspan [16] and Ehrhard & Davis [10] and assume that the speed of the contact line is related to the contact angle by the Tanner Law

$$R_t = \kappa(\theta^m - \theta_0^m), \tag{6.1}$$

where θ_0 is the equilibrium contact angle and κ is an empirically-determined positive constant with dimensions of velocity. More general Tanner Laws are used in Chapters 2 and 3.

From the results given in Chapter 1 the familiar lubrication approximation

to the governing Navier-Stokes and mass conservation equations yield

$$0 = p_z + \rho g, \tag{6.2}$$

$$\mu u_{zz} = p_r, \tag{6.3}$$

$$\mu v_{zz} = \frac{1}{r} p_\varphi, \tag{6.4}$$

$$\frac{1}{r}(ru)_r + \frac{1}{r} v_\varphi + w_z = 0, \tag{6.5}$$

where g denotes acceleration due to gravity, subject to the boundary conditions

$$u = \lambda u_z, \quad v = \lambda v_z \quad \text{on} \quad z = 0, \tag{6.6}$$

$$\mu u_z = 0, \quad \mu v_z = 0 \quad \text{on} \quad z = h, \tag{6.7}$$

$$p = p_0 - \frac{kr^2}{2} - \tau \nabla^2 h \quad \text{on} \quad z = h, \tag{6.8}$$

$$w = h_t + u h_r + \frac{v}{r} h_\varphi \quad \text{on} \quad z = h, \tag{6.9}$$

where the fluid velocity has been written $\mathbf{u}=(u, v, w)$. Equation (6.6) is the slip condition that mitigates the stress singularity at the contact line. In the simple Navier slip model used here the slip coefficient λ is a (small) positive constant with the dimensions of length. Equation (6.7) represents zero tangential stress at the free surface and Eq. (6.8) is the normal stress condition which includes both the effects of surface tension and the non-uniform external pressure loading caused by the jet of air. Equation (6.9) is the kinematic free-surface condition which can be used with Eq. (6.5) to derive the flux condition

$$h_t + \frac{1}{r}\Big[(rQ_1)_r + (Q_2)_\varphi\Big] = 0, \tag{6.10}$$

where Q_1 and Q_2 denote the fluxes in the r and φ directions respectively defined by

$$Q_1 = \int_0^h u \, dz, \qquad Q_2 = \int_0^h v \, dz. \tag{6.11}$$

Solving Eqs. (6.2) (6.8) for u and v allows Q_1 and Q_2 to be evaluated explicitly, and substituting these expressions into Eq. (6.10) gives the governing equation for h.

We non-dimensionalise the problem using a characteristic radial length scale L (to be defined subsequently) and κ as the characteristic horizontal velocity

scale. The corresponding non-dimensional variables are defined by $r = Lr'$, $\varphi = \varphi'$, $h = \theta_0 L h'$, $R = \theta_0^m L R'$, $t = Lt'/\kappa$, and $\theta = \theta_0 \theta'$. Dropping the primes at once for simplicity we obtain the non-dimensional version of the governing equation for h, namely

$$\begin{aligned} Ch_t + \frac{1}{r}\left[rh^2\left(\frac{h}{3}+\lambda\right)\left((\nabla^2 h)_r - G^2 h_r + Jr\right)\right]_r \\ + \frac{1}{r^2}\left[h^2\left(\frac{h}{3}+\lambda\right)\left((\nabla^2 h)_\varphi - G^2 h_\varphi\right)\right]_\varphi = 0, \end{aligned} \tag{6.12}$$

together with the non-dimensional version of Eq. (6.1), namely,

$$R_t = \theta^m - 1, \tag{6.13}$$

where the constants J, C and G are as defined previously. Note that if we set $h = h(r)$ and $\lambda = 0$ in Eq. (6.12) we recover Eq. (2.11)(a) from Chapter 2. Without loss of generality we can choose $L = (\tau\theta_0/k)^{1/3}$ (corresponding to setting $J = 1$). As in Chapter 5 we shall retain J explicitly in all of our analytical calculations but set $J = 1$ in all of our numerical calculations.

Note that if we identify the dimensional jet strength k with $\rho\omega^2$ then Eq. (6.12) is identical to the equation describing the spin coating of a thin drop on a horizontal substrate rotating with constant angular speed ω. Hence all the results presented here apply to both spin-coating and air-jet-blowing problems.

The appropriate boundary conditions for Eq. (6.12) are

$$h(R, \varphi, t) = 0, \tag{6.14}$$

$$\left(h_r - \frac{1}{R^2} R_\varphi h_\varphi\right)\left(1 + \frac{R_\varphi^2}{R^2}\right)^{-\frac{1}{2}}\Bigg|_{r=R} = -\theta, \tag{6.15}$$

together with the regularity conditions

$$h_r(0, \varphi, t) = 0, \tag{6.16}$$

$$Q_1(0, \varphi, t) = 0, \tag{6.17}$$

which must be satisfied together with appropriate initial conditions for h and R. Equation (6.14) requires the free surface to have zero height at the contact

line and Eq. (6.15) ensures that the contact angle takes the correct value. The volume of the drop is given by

$$2\pi V = \int_0^{2\pi} \int_0^R hr \, dr d\varphi. \tag{6.18}$$

In what follows we shall restrict our attention to the special case $G = 0$ when gravity effects are negligible. In addition, we follow Greenspan [16] and adopt the linear Tanner Law obtained by setting $m = 1$ in Eq. (6.13).

6.2.2 Basic State

In equilibrium $h(r, \varphi, t) = h_0(r)$, $R(\varphi, t) = R_0$ and $\theta = \theta_0$. Substituting these solutions into Eqs. (6.12) and (6.14) - (6.16) and using Eq. (6.17) with $G = 0$ yields the governing equation for the basic state, namely

$$h_0''' + \frac{1}{r} h_0'' - \frac{1}{r^2} h_0 + Jr = 0, \tag{6.19}$$

where the prime denotes differentiation with respect to r, subject to the boundary conditions

$$h_0(R_0) = 0, \tag{6.20}$$

$$h_0'(R_0) = -1, \tag{6.21}$$

$$h_0'(0) = 0. \tag{6.22}$$

The solution for h_0 is given by

$$h_0 = \frac{1}{32}(r^2 - R_0^2)\left[JR_0(R_0^2 - r^2) - 16\right]. \tag{6.23}$$

From Eq. (6.18) the volume of the drop is given by

$$V = \frac{1}{192} R_0^3 (24 - JR_0^3). \tag{6.24}$$

Figure 6.2 plots the basic-state profiles for $R_0 = 1$, 1.5, 2 and 2.5. These solutions are exactly the axisymmetric non-annular solutions described in Chapter 2. Note that "physical" solutions (i.e. solutions for which $h_0 \geq 0$ over the entire interval $0 \leq r \leq R_0$) exist only when R_0 lies in the range $0 \leq R_0 \leq (16/J)^{1/3}$.

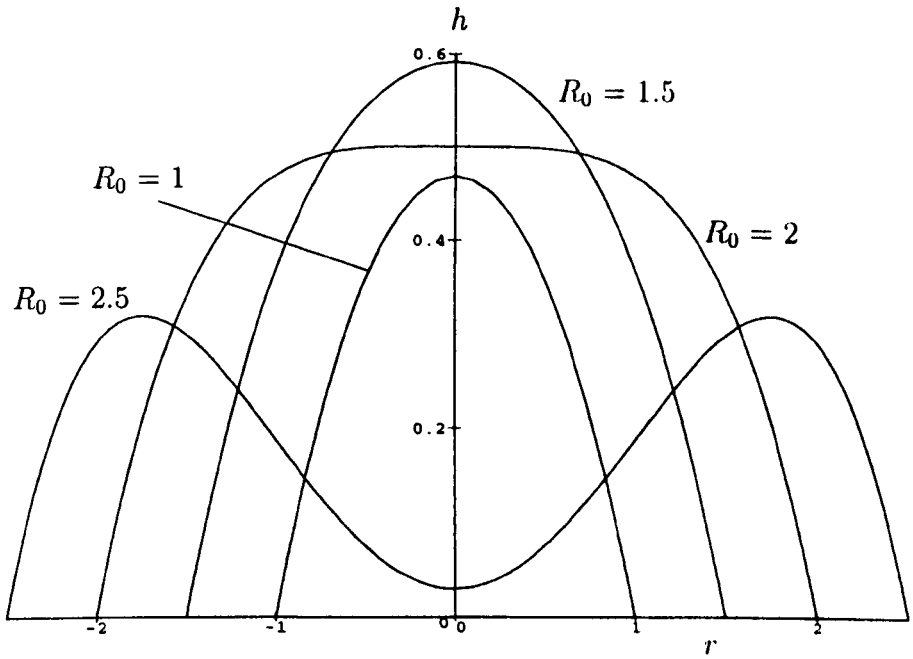

Figure 6.2: Basic-state profiles of a non-annular drop for $R_0 = 1$, 1.5, 2 and 2.5.

6.2.3 Linear Stability Problem

In order to analyse the linear stability of the drop to small perturbations with azimuthal wavenumber $q \geq 0$ we write $h = h_0(r) + h_1(r)\exp(iq\varphi + \sigma t)$ and $R = R_0 + R_1 \exp(iq\varphi + \sigma t)$, where $h_1(r)$ is the perturbation to the basic-state profile, R_1 is the perturbation to the position of the contact line and σ is the unknown (complex) growth coefficient. Note that the wavenumber q must be an integer to ensure physically-sensible solutions. Substituting these expressions into Eqs. (6.12) - (6.17) and retaining only first-order terms in the perturbations yields the governing equation for h_1:

$$\begin{aligned} C\sigma h_1 + \frac{1}{r}\left[rh_0^2\left(\frac{h_0}{3}+\lambda\right)\left(h_1'' + \frac{1}{r}h_1' - \frac{q^2}{r^2}h_1\right)'\right]' \\ - \frac{q^2}{r^2}h_0^2\left(\frac{h_0}{3}+\lambda\right)\left(h_1'' + \frac{1}{r}h_1' - \frac{q^2}{r^2}h_1\right) = 0, \end{aligned} \tag{6.25}$$

which is subject to the boundary conditions

$$R_1 = h_1(R_0), \tag{6.26}$$

$$R_1 = h_1(-R_0), \tag{6.27}$$

$$h_1'(R_0) + h_0''(R_0)R_1 = -\sigma R_1. \tag{6.28}$$

$$h_1'(-R_0) - h_0''(-R_0)R_1 = \sigma R_1. \tag{6.29}$$

Eliminating R_1 from Eqs. (6.26) – (6.29) and using Eq. (6.23) yields

$$h_1'(-R_0) + \left(\frac{JR_0^3 + 4}{4R_0}\right) h_1(-R_0) = \sigma h_1(-R_0), \tag{6.30}$$

$$h_1'(R_0) - \left(\frac{JR_0^3 + 4}{4R_0}\right) h_1(R_0) = -\sigma h_1(R_0). \tag{6.31}$$

In the special case $q = 0$ (but *not* otherwise) it is also necessary to impose the volume condition

$$\int_0^{R_0} h_1 r \, dr = 0, \tag{6.32}$$

as an additional condition.

6.2.4 Quasi-static Motion $C = 0$

We can make considerable analytical progress in the special case of quasi-static motion, corresponding to $C = 0$. Note that all the analytical results presented here have been confirmed by numerical calculations of the kind described in the next section.

Axisymmetric Perturbations $q = 0$

The general solution when $C = 0$ and $q = 0$ can be written in the form

$$h_1 = Q^* f(r, J, R_0) + \alpha r^2 + \beta + \gamma \ln r, \tag{6.33}$$

where Q^*, α, β and γ are constants and the function $f(r, J, R_0)$ is not given here for brevity. Since $f \sim \ln(R_0/r)\ln(R_0 - r)/3\lambda$ as $r \to R_0^-$, solutions for h_1 that do not have a singularity at $r = R_0$ are possible only if $Q^* = 0$. Thus the appropriate solution for h_1 is simply

$$h_1 = \alpha r^2 + \beta + \gamma \ln r. \tag{6.34}$$

For solutions that are bounded at the origin we set $\gamma = 0$. Using boundary condition (6.31) and volume condition (6.32) yields $\sigma = \sigma_0$, where

$$\sigma_0 = \frac{JR_0^3 - 12}{4R_0}, \tag{6.35}$$

recovering the conditionally stable growth rate obtained in Chapter 2.

Non-axisymmetric Perturbations $q \geq 1$

A solution of Eq. (6.25) for h_1 when $C = 0$ that does not have a singularity at $r = R_0$ is

$$h_1 = \alpha r^q + \frac{\beta}{r^q}, \tag{6.36}$$

where α and β are constants. For solutions that are bounded at the origin we require $\beta = 0$ and using the boundary condition (6.31) yields $\sigma = \sigma_q$, where

$$\sigma_q = \frac{JR_0^3 + 4(1-q)}{4R_0}, \tag{6.37}$$

for $q = 1, 2, 3, \ldots$. Note that, because these solutions do not satisfy the volume condition (6.32), substituting $q = 0$ into Eq. (6.37) does not recover the expression obtained previously for σ_0. The neutral stability curves are obtained by setting $\sigma_q = 0$ in Eq. (6.37) and are given by

$$R_0 = \left(\frac{4(q-1)}{J}\right)^{\frac{1}{3}}, \tag{6.38}$$

for $q = 1, 2, 3, \ldots$.

General Perturbations $q \geq 0$

Figure 6.3 plots the growth rate σ_q as a function of R_0 for $q = 0$, 1, 2, ..., 7. Since the largest eigenvalue is $\sigma_1 = JR_0^3/4 > 0$ the drop is unconditionally unstable via the $q = 1$ mode. Note that $\sigma_4 = \sigma_0$ and so both $q = 0$ and $q = 4$ modes correspond to exactly the same curve in Fig. 6.3. Furthermore, the neutral stability curve for $q = 5$ is identical to the curve where the basic-state solutions become unphysical, namely $R_0 = (16/J)^{1/3}$. For $q \geq 5$ Fig. 6.3 shows that $\sigma_q < 0$ for all values of R_0 corresponding to physical solutions, and hence these modes are always stable.

6.2.5 The General Case $C \neq 0$

To obtain the neutral stability curves for $C \neq 0$ we set $\sigma = 0$ in Eq. (6.25) and the boundary conditions (6.30) and (6.31). This procedure yields exactly the

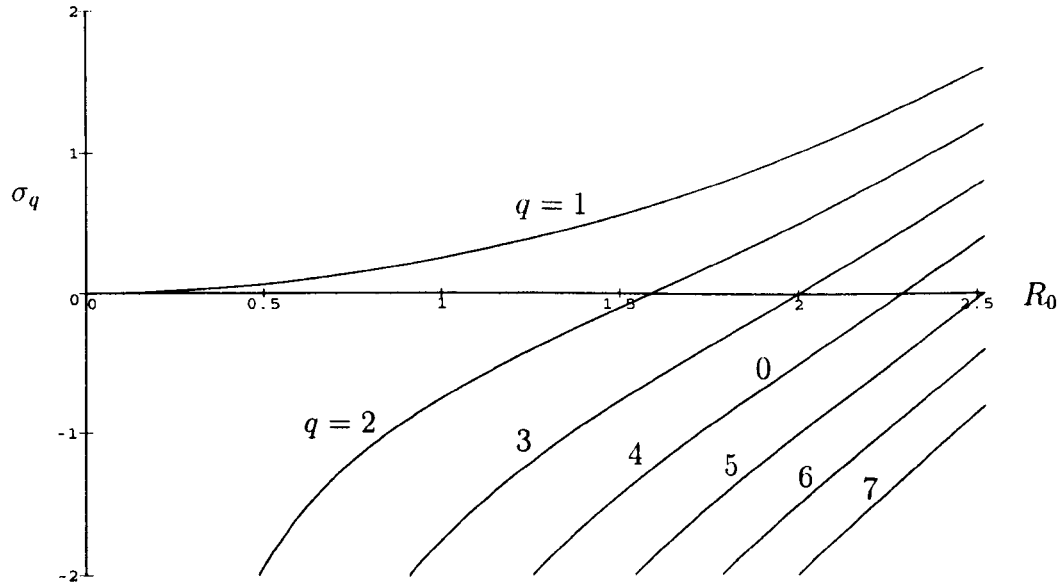

Figure 6.3: Plot of the growth rates σ_q for $q = 0, 1, 2, 3, \ldots, 7$ as a function of R_0 for a non-annular drop in the case $C = 0$.

same neutral stability curves as those calculated previously in the case $C = 0$ as given by $R_0 = (12/J)^{1/3}$ for the $q = 0$ mode, and by Eq. (6.38) for the $q \geq 1$ modes. When $\sigma \neq 0$ we must proceed numerically.

Results

Figure 6.4 plots the largest eigenvalue as a function of R_0 for $q = 0, 1, 2, 3, \ldots, 6$ in the case $C = 1$. The neutral stability points are given by $R_0 = (12/J)^{1/3}$ for the $q = 0$ mode, and by Eq. (6.38) for the $q \geq 1$ modes. For R_0 in the range $0 < R_0 < 2.12$ the most unstable mode corresponds to $q = 1$, while for $2.12 < R_0 < 2.46$ it corresponds to $q = 2$ and for $2.46 < R_0 \leq (16/J)^{1/3} \approx 2.52$ to $q = 3$. Note that the curves corresponding to the $q = 0$ and $q = 4$ modes are distinct for $C \neq 0$ and coincide only in the special case $C = 0$.

Figures 6.5(a) - (d) plot the largest eigenvalue as a function of R_0 for $q = 0, 1, 2, 3, \ldots, 7$ for $C = 1$, 0.1, 0.01 and 0.001 respectively. The thick curves correspond to the solutions in the special case $C = 0$ given by σ_q for $q = 0, 1, 2, 3, \ldots, 7$. The results in the case $C = 1$ (Fig. 6.5(a)) have already been

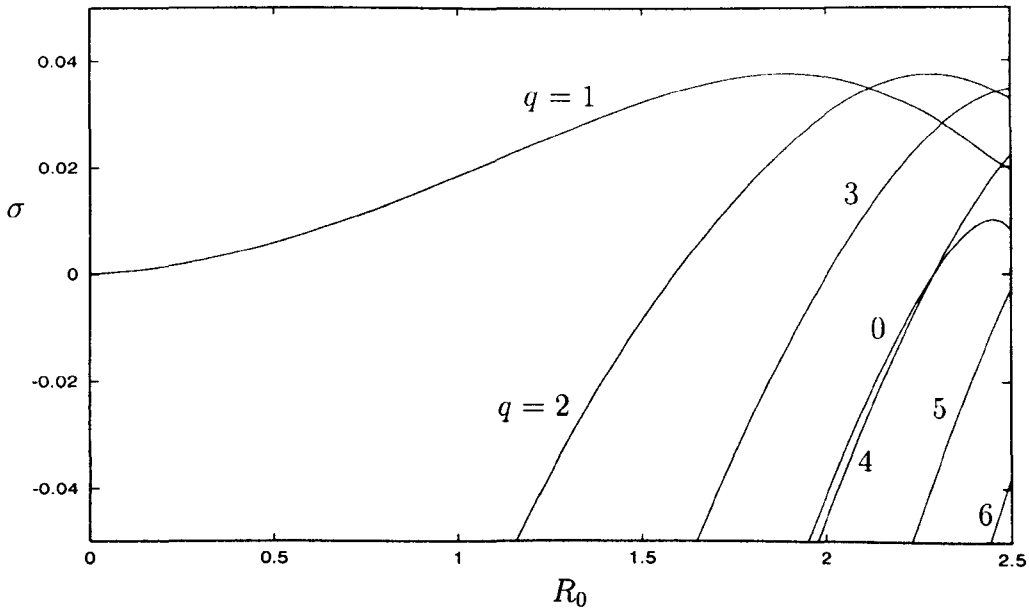

Figure 6.4: Plot of the largest eigenvalue as a function of R_0 for a non-annular drop for $q = 0, 1, 2, 3, \ldots, 6$ in the case $C = 1$.

described. For $C = 0.1$ (Fig. 6.5(b)) the most unstable mode corresponds to $q = 1$ for $0 < R_0 < 2.19$ and to $q = 2$ for $2.19 < R_0 < 2.52$. For $C = 0.01$ (Fig. 6.5(c)) the same qualitative behaviour occurs, however the value of R_0 at which the most unstable mode changes from the $q = 1$ mode to the $q = 2$ mode is $R_0 \approx 2.38$. For $C = 0.001$ (Fig. 6.5(d)) the most unstable mode corresponds to $q = 1$ for all values of R_0 corresponding to physical solutions. In particular, Fig. 6.5 shows how the numerically-calculated values of σ approach σ_q in the limit $C \to 0$.

6.3 Annular Drops

6.3.1 Problem Formulation

Clearly, the major difference between the annular drops discussed in this section and the non-annular drops discussed in the previous section is that the former have two contact lines and hence two contact angles. The positions of the "inner" and "outer" contact lines are denoted by $r = R_1(\varphi, t)$ at which the

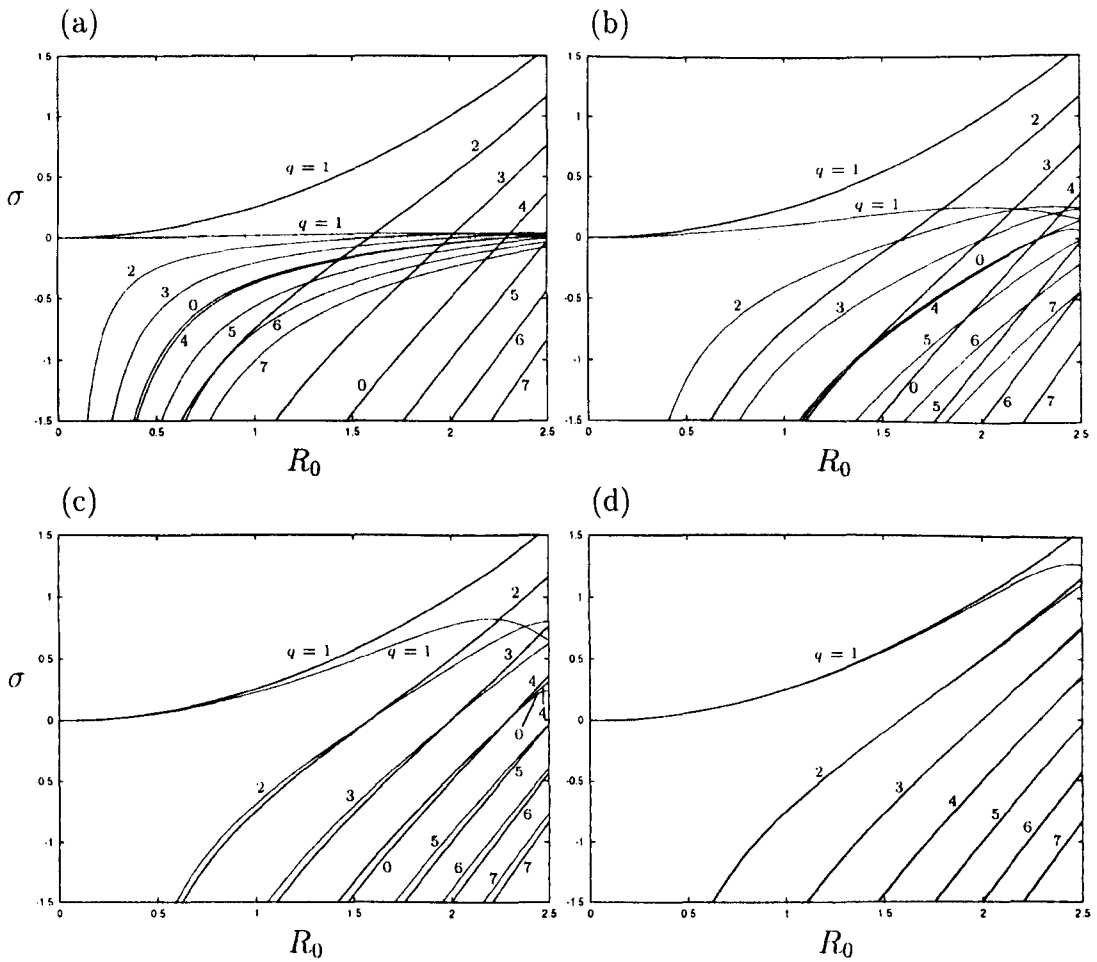

Figure 6.5: (a) (d) Plot of the largest eigenvalue as a function of R_0 for a non-annular drop for $q = 0, 1, 2, 3, \ldots, 7$ for $C = 1$, 0.1, 0.01 and 0.001. The thick curves correspond to the solutions $\sigma_0 = (JR_0^3 - 12)/4R_0$ for $q = 0$ and $\sigma_q = (JR_0^3 + 4(1-q))/4R_0$ for $q = 1, 2, 3, \ldots, 7$.

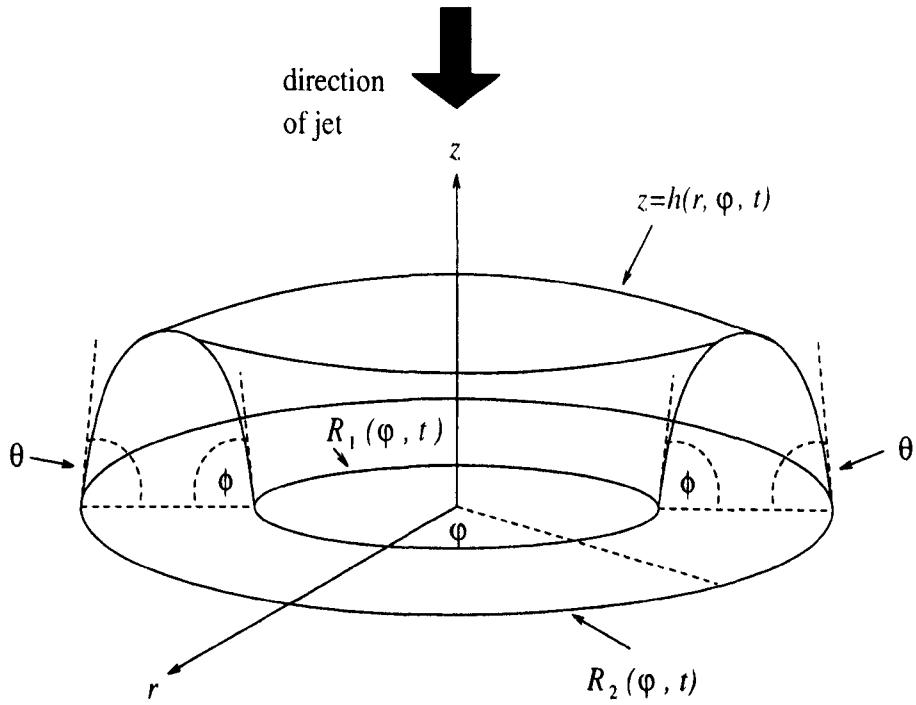

Figure 6.6: Geometry of the annular problem.

contact angle is $\phi = \phi(t)$ and $r = R_2(\varphi, t) > R_1$ at which the contact angle is $\theta = \theta(t)$, respectively. The geometry of the annular problem is shown in Fig. 6.6.

Since there are now two moving contact lines, we need to replace Eq. (6.1) by two Tanner Laws relating the speed of each contact line to its contact angle. These are given by

$$(R_1)_t = \kappa(\phi_0^m - \phi^m), \tag{6.39}$$

$$(R_2)_t = \kappa(\theta^m - \theta_0^m), \tag{6.40}$$

where ϕ_0 and θ_0 are the equilibrium values of the inner and outer contact angles respectively.

The non-dimensional governing equation for h is again given by Eq. (6.12) together with the non-dimensional versions of Eqs. (6.39) and (6.40), namely

$$(R_1)_t = \phi_0^m - \phi^m, \tag{6.41}$$

$$(R_2)_t = \theta^m - 1. \tag{6.42}$$

The appropriate boundary conditions for Eq. (6.12) in this case are

$$h(R_1, \varphi, t) = 0, \tag{6.43}$$

$$h(R_2, \varphi, t) = 0, \tag{6.44}$$

$$\left(h_r - \frac{1}{R_1^2}(R_1)_\varphi h_\varphi\right)\left(1 + \frac{(R_1)_\varphi^2}{R_1^2}\right)^{-\frac{1}{2}}\Bigg|_{r=R_1} = \phi, \tag{6.45}$$

$$\left(h_r - \frac{1}{R_2^2}(R_2)_\varphi h_\varphi\right)\left(1 + \frac{(R_2)_\varphi^2}{R_2^2}\right)^{-\frac{1}{2}}\Bigg|_{r=R_2} = -\theta, \tag{6.46}$$

which must be satisfied together with appropriate initial conditions for h, R_1 and R_2. The volume of the annular drop is given by

$$2\pi V = \int_0^{2\pi}\int_{R_1}^{R_2} hr\,\mathrm{d}r\mathrm{d}\varphi. \tag{6.47}$$

In what follows we shall again restrict our attention to the special case $G = 0$ when gravity effects are negligible, and adopt the linear Tanner Laws obtained by setting $m = 1$ in Eqs. (6.41) and (6.42).

6.3.2 Basic State

In equilibrium $h(r, \varphi, t) = h_0(r)$, $R_1(\varphi, t) = R_1^0$, $R_2(\varphi, t) = R_2^0$, $\theta = \theta_0$ and $\phi = \phi_0$. Substituting these expressions into Eqs. (6.12), (6.43), (6.44) and (6.46) with $G = 0$ yields the governing equation for the basic state given by Eq. (6.19) subject to the boundary conditions

$$h_0(R_1^0) = 0, \tag{6.48}$$

$$h_0(R_2^0) = 0, \tag{6.49}$$

$$h_0'(R_2^0) = -1. \tag{6.50}$$

The solution for h_0 is given by

$$h_0 = f(r, R_1^0, R_2^0) + Jg(r, R_1^0, R_2^0), \tag{6.51}$$

where the functions $f(r, R_1^0, R_2^0)$ and $g(r, R_1^0, R_2^0)$ are given by

$$f(r, R_1^0, R_2^0) = \Big\{R_2^0[(R_2^0)^2 - r^2]\ln R_1^0 - R_2^0[(R_1^0)^2 - r^2]\ln R_2^0 - R_2^0[(R_2^0)^2 - (R_1^0)^2]\ln r\Big\}\Big\{(R_2^0)^2 - (R_1^0)^2 + 2(R_2^0)^2\ln(R_1^0/R_2^0)\Big\}^{-1}, \tag{6.52}$$

$$g(r, R_1^0, R_2^0) = \frac{1}{32}\Big\{-2(R_2^0)^2[(R_2^0)^2 - r^2]^2 \ln R_1^0 + 2(R_2^0)^2[(R_2^0)^2 - (R_1^0)^2]^2 \ln r$$
$$+2(R_2^0)^2[(R_1^0)^2 - r^2][2(R_2^0)^2 - (R_1^0)^2 - r^2] \ln R_2^0 - [(R_1^0)^2 - r^2] \qquad (6.53)$$
$$\times[(R_2^0)^2 - r^2][(R_2^0)^2 - (R_1^0)^2]\Big\}\Big\{(R_2^0)^2 - (R_1^0)^2 + 2(R_2^0)^2 \ln(R_1^0/R_2^0)\Big\}^{-1}.$$

From Eq. (6.47) the volume of the drop is given by

$$V = S(R_1^0, R_2^0) + JT(R_1^0, R_2^0), \qquad (6.54)$$

where the functions $S = S(R_1^0, R_2^0)$ and $T = T(R_1^0, R_2^0)$ are given by

$$S(R_1^0, R_2^0) = \frac{1}{4}\Big\{R_2^0[(R_2^0)^4 - (R_1^0)^4] \ln(R_1^0/R_2^0) + R_2^0[(R_2^0)^2 - (R_1^0)^2]^2\Big\}$$
$$\times\Big\{(R_2^0)^2 - (R_1^0)^2 + 2(R_2^0)^2 \ln(R_1^0/R_2^0)\Big\}^{-1}, \qquad (6.55)$$

$$T(R_1^0, R_2^0) = -\Big\{4(R_2^0)^2[2(R_1^0)^2 + (R_2^0)^2][(R_2^0)^2 - (R_1^0)^2]^2 \ln(R_1^0/R_2^0)$$
$$+[(R_1^0)^2 + 5(R_2^0)^2][(R_2^0)^2 - (R_1^0)^2]^3\Big\} \qquad (6.56)$$
$$\times\Big\{384[(R_2^0)^2 - (R_1^0)^2 + 2(R_2^0)^2 \ln(R_1^0/R_2^0)]\Big\}^{-1}.$$

The remaining boundary condition (6.45) yields the relationship between ϕ_0, R_1^0 and R_2^0, namely

$$\phi_0 = \Big\{[(R_2^0)^2 - (R_1^0)^2][(R_2^0)^4 - (R_1^0)^4 + 4(R_1^0)^2(R_2^0)^2 \ln(R_1^0/R_2^0)]J$$
$$-16R_2^0[(R_2^0)^2 - (R_1^0)^2 + 2(R_1^0)^2 \ln(R_1^0/R_2^0)]\Big\} \qquad (6.57)$$
$$\times\Big\{16R_1^0[(R_2^0)^2 - (R_1^0)^2 + 2(R_2^0)^2 \ln(R_1^0/R_2^0)]\Big\}^{-1}.$$

Figure 6.7 plots the basic-state profiles for $R_2^0 = 2$, 2.3, 2.6 and 2.9 in the case $\phi_0 = 1$. These solutions are exactly the axisymmetric annular solutions described in Chapter 3. For $\phi_0 \leq 1$ solutions exist only for values of R_2^0 greater than a critical value, while for $\phi_0 > 1$ solutions exist only for values of R_1^0 less than a critical value. This behaviour is shown in Fig. 6.8 which plots R_1^0 against the corresponding value for R_2^0 in the cases $\phi_0 = 0.7$, 1 and 1.3.

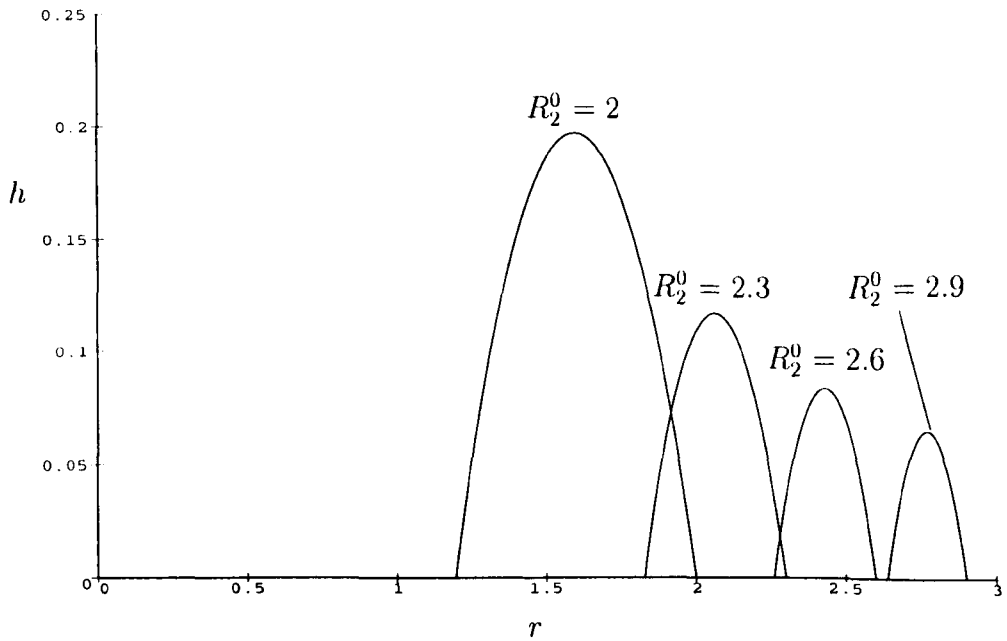

Figure 6.7: Basic-state profiles of an annular drop for $R_2^0 = 2$, 2.3, 2.6 and 2.9 in the case $\phi_0 = 1$.

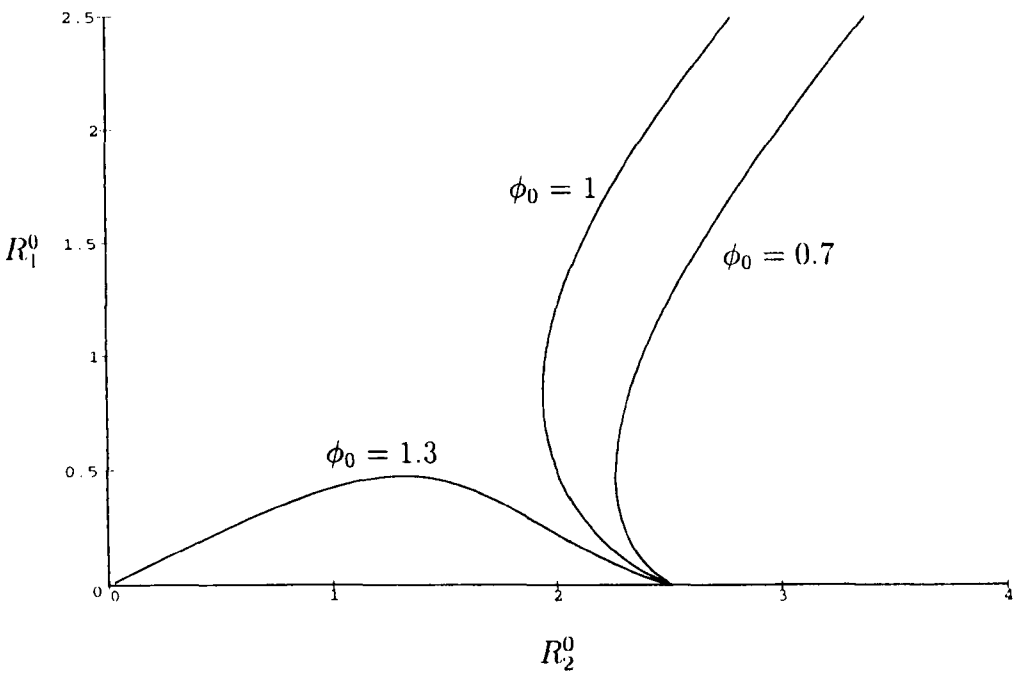

Figure 6.8: Plot of R_1^0 against R_2^0 for annular solutions corresponding to $\phi_0 = 0.7$, 1 and 1.3.

6.3.3 Linear Stability Problem

In order to analyse the linear stability of the drop we perturb h as before and write $R_1 = R_1^0 + R_1^1 \exp(iq\varphi + \sigma t)$ and $R_2 = R_2^0 + R_2^1 \exp(iq\varphi + \sigma t)$, where R_1^1 and R_2^1 are the perturbations to the positions of the contact lines. Substituting these expressions into Eqs. (6.12) and (6.41) – (6.46) yields the governing equation for h_1 given by Eq. (6.25) which is subject to the boundary conditions

$$R_1^1 = -\frac{1}{\phi_0} h_1(R_1^0), \tag{6.58}$$

$$R_2^1 = h_1(R_2^0), \tag{6.59}$$

$$h_1'(R_1^0) + h_0''(R_1^0) R_1^1 = -\sigma R_1^1, \tag{6.60}$$

$$h_1'(R_2^0) + h_0''(R_2^0) R_2^1 = -\sigma R_2^1. \tag{6.61}$$

Eliminating R_1^1 and R_2^1 from Eqs. (6.58) – (6.61) and using Eq. (6.51) yields

$$\phi_0 h_1'(R_1^0) - f_1(J, R_1^0, R_2^0) h_1(R_1^0) = \sigma h_1(R_1^0), \tag{6.62}$$

$$h_1'(R_2^0) + f_2(J, R_1^0, R_2^0) h_1(R_2^0) = -\sigma h_1(R_2^0), \tag{6.63}$$

where the functions $f_1(J, R_1^0, R_2^0)$ and $f_2(J, R_1^0, R_2^0)$ are given by

$$\begin{aligned} f_1(J, R_1^0, R_2^0) = &\Big\{ 4(R_1^0)^2 R_2^0 [3J R_2^0 ((R_1^0)^2 - (R_2^0)^2) + 8] \ln(R_1^0/R_2^0) \\ &- [(R_1^0)^2 - (R_2^0)^2][5J(R_1^0)^4 - 2J(R_1^0)^2(R_2^0)^2 + J(R_2^0)^4 - 16R_2^0] \Big\} \\ &\times \Big\{ 16(R_1^0)^2 [(R_1^0)^2 - (R_2^0)^2 - 2(R_2^0)^2 \ln(R_1^0/R_2^0)] \Big\}^{-1}, \end{aligned} \tag{6.64}$$

$$\begin{aligned} f_2(J, R_1^0, R_2^0) = &\Big\{ 4(R_2^0)^2 [J(R_2^0)^3 + 4] \ln(R_1^0/R_2^0) + [(R_1^0)^2 - (R_2^0)^2] \\ &\times [J R_2^0 ((R_1^0)^2 - (R_2^0)^2) + 8] \Big\} \Big\{ 8R_2^0 [(R_1^0)^2 - (R_2^0)^2 - 2(R_2^0)^2 \ln(R_1^0/R_2^0)] \Big\}^{-1}. \end{aligned} \tag{6.65}$$

Again in the special case $q = 0$ it is also necessary to impose the additional condition

$$\int_{R_1^0}^{R_2^0} h_1 r \, \mathrm{d}r = 0. \tag{6.66}$$

6.3.4 Quasi-static Motion $C = 0$

As before, we can make considerable analytical progress in the special case of quasi-static motion ($C = 0$). Again all the analytical results presented here have

been confirmed by numerical calculations.

Axisymmetric Perturbations $q = 0$

From Sec. 6.2.4 the solution for h_1 when $C = 0$ and $q = 0$ is given by Eq. (6.34). Applying boundary conditions (6.62) and (6.63) and the volume condition (6.66) recovers the unconditionally unstable results obtained in Chapter 3, namely $\sigma = \sigma_{0+} > 0$ and $\sigma = \sigma_{0-} < \sigma_{0+}$ The expressions for $\sigma_{0\pm}$ are not repeated here. Figures 6.9(a) and (b) plot σ_{0+} and σ_{0-} respectively as functions of R_2^0 for $\phi_0 = 0.7$, 1 and 1.3.

Non-axisymmetric Perturbations $q \geq 1$

From Sec. 6.2.4 the solution for h_1 when $C = 0$ is given by Eq. (6.36) subject to the boundary conditions (6.62) and (6.63). Solving this system yields two expressions for σ, namely $\sigma = \sigma_{q+} > 0$ and $\sigma = \sigma_{q-} < \sigma_{q+}$. The expressions for $\sigma_{q\pm}$ are not given here for brevity. As before note that, because these solutions do not satisfy the volume condition (6.66), substituting $q = 0$ into $\sigma_{q\pm}$ does not recover the expressions obtained previously for $\sigma_{0\pm}$.

General Perturbations $q \geq 0$

Figures 6.10(a) – (c) plot the growth rate σ_{q+} as a function of R_2^0 for $q = 0$, 1, 2, 3 and 4 in the cases $\phi_0 = 0.7$, 1 and 1.3 respectively. In Figs. 6.10(a) and (b) (corresponding to $\phi_0 = 0.7$ and 1 respectively) the free ends of the curves at $R_2^0 = (16/J)^{1/3} \approx 2.52$ correspond to $R_1^0 = 0$. As we move along each curve away from these ends the value of R_1^0 increases monotonically from zero. In Fig. 6.10(c) (corresponding to $\phi_0 = 1.3$) solutions lie in the range $0 < R_2^0 \leq (16/J)^{1/3} \approx 2.52$. As R_2^0 increases in this range, R_1^0 increases from zero to a maximum (less than the corresponding value of R_2^0) and then decreases back to zero.

In Fig. 6.10(a) ($\phi_0 = 0.7$) the most unstable mode corresponds to $q = 0$ for $0 < R_1^0 < 0.19$ and $q = 1$ for $R_1^0 > 0.19$. In Fig. 6.10(b) ($\phi_0 = 1$) the same qualitative behaviour occurs with the most unstable mode corresponding

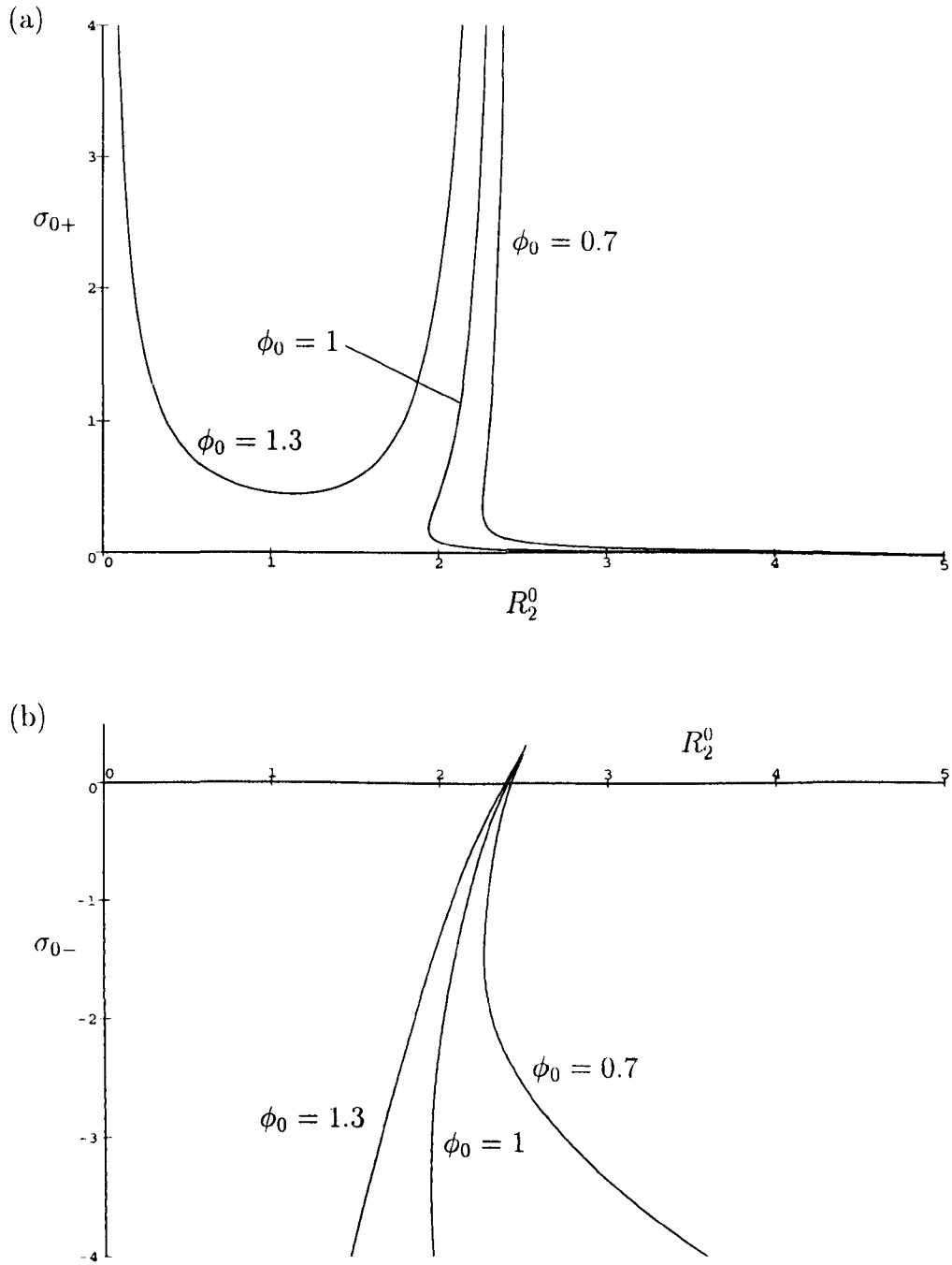

Figure 6.9: (a) - (b) Plot of the growth rates σ_{0+} and σ_{0-} as functions of R_2^0 for an annular drop for $\phi_0 = 0.7$, 1 and 1.3 in the case $q = 0$ and $C' = 0$.

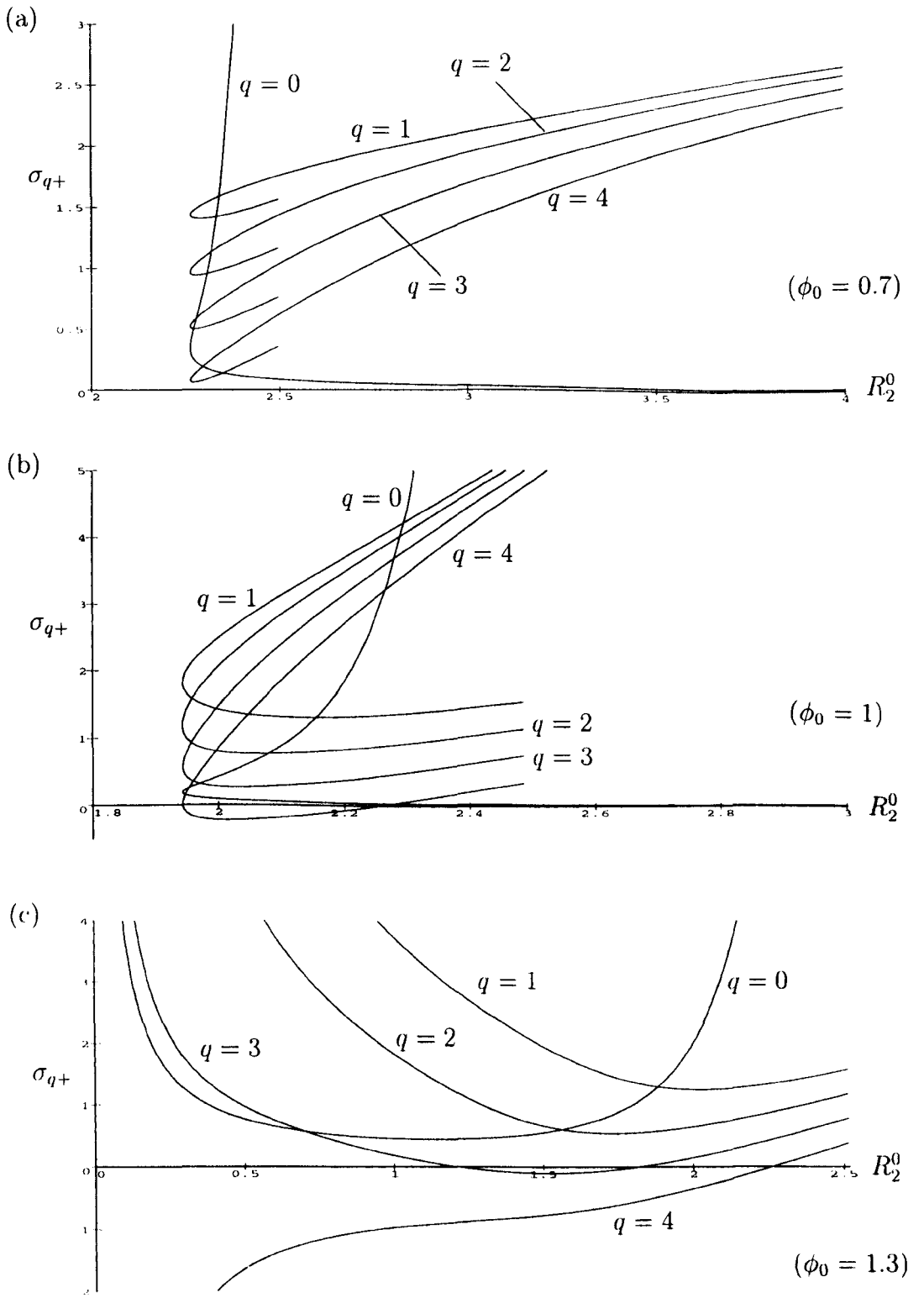

Figure 6.10: (a) - (c) Plot of the growth rates σ_{q+} for $q = 0$, 1, 2, 3 and 4 as a function of R_2^0 for an annular drop in the cases $\phi_0 = 0.7$, 1 and 1.3 for $C = 0$.

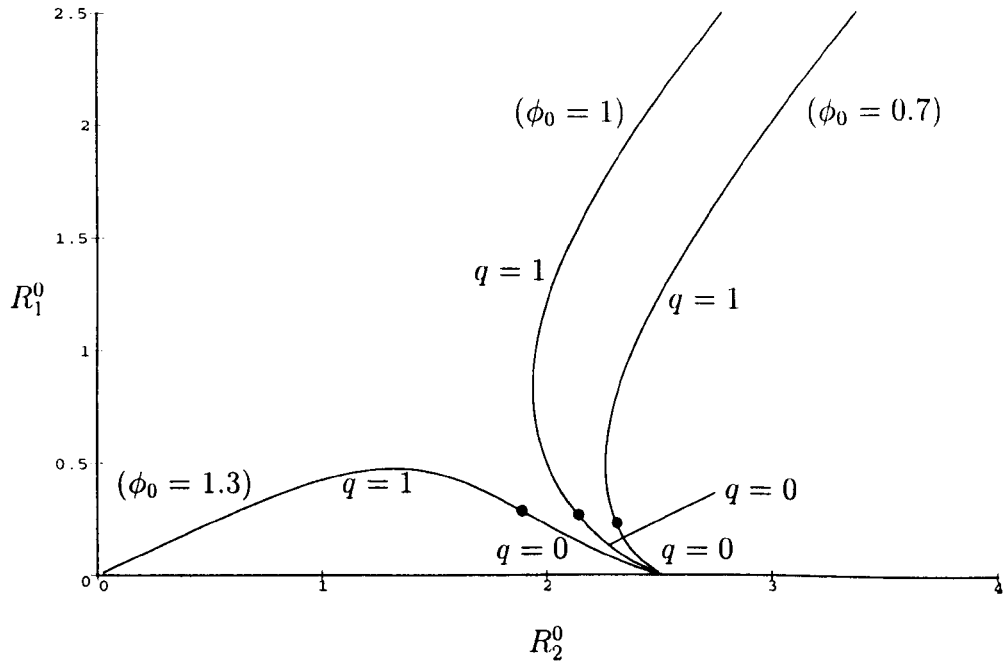

Figure 6.11: Plot of R_1^0 against R_2^0 for annular solutions corresponding to $\phi_0 = 0.7$, 1 and 1.3 showing the most unstable wavenumber for $C = 0$. The dots correspond to the values of R_1^0 and R_2^0 at which the most unstable mode jumps between $q = 0$ and $q = 1$.

to $q = 0$ for $0 < R_1^0 < 0.26$ and $q = 1$ for $R_1^0 > 0.26$. In Fig. 6.10(c) ($\phi_0 = 1.3$), however, the most unstable mode corresponds to $q = 1$ for $0 < R_2^0 < 1.86$ and to $q = 0$ for $1.86 < R_2^0 < 2.52$. These results are summarised in Fig. 6.11, which shows the wavenumber of the most unstable mode for $\phi_0 = 0.7$, 1 and 1.3. The dots on Fig. 6.11 denote the values of R_1^0 and R_2^0 at which the most unstable mode jumps between $q = 0$ and $q = 1$.

6.3.5 The General Case $C \neq 0$

Figures 6.12(a) - (d) plot the largest eigenvalue as a function of R_2^0 for $q = 0$, 1, 2,..., 9 in the case $\phi_0 = 0.7$ for $C = 1$, 0.1, 0.01 and 0.001 respectively. In Fig. 6.12 the free ends of the curves at $R_2^0 = (16/J)^{1/3} \approx 2.52$ correspond to $R_1^0 = 0$ and as we move along each curve away from these ends the value of R_1^0 increases monotonically from zero. For $C = 1$ (Fig. 6.12(a)) the most unstable mode corresponds to $q = 0$ for small values of R_1^0. As R_1^0 increases the most

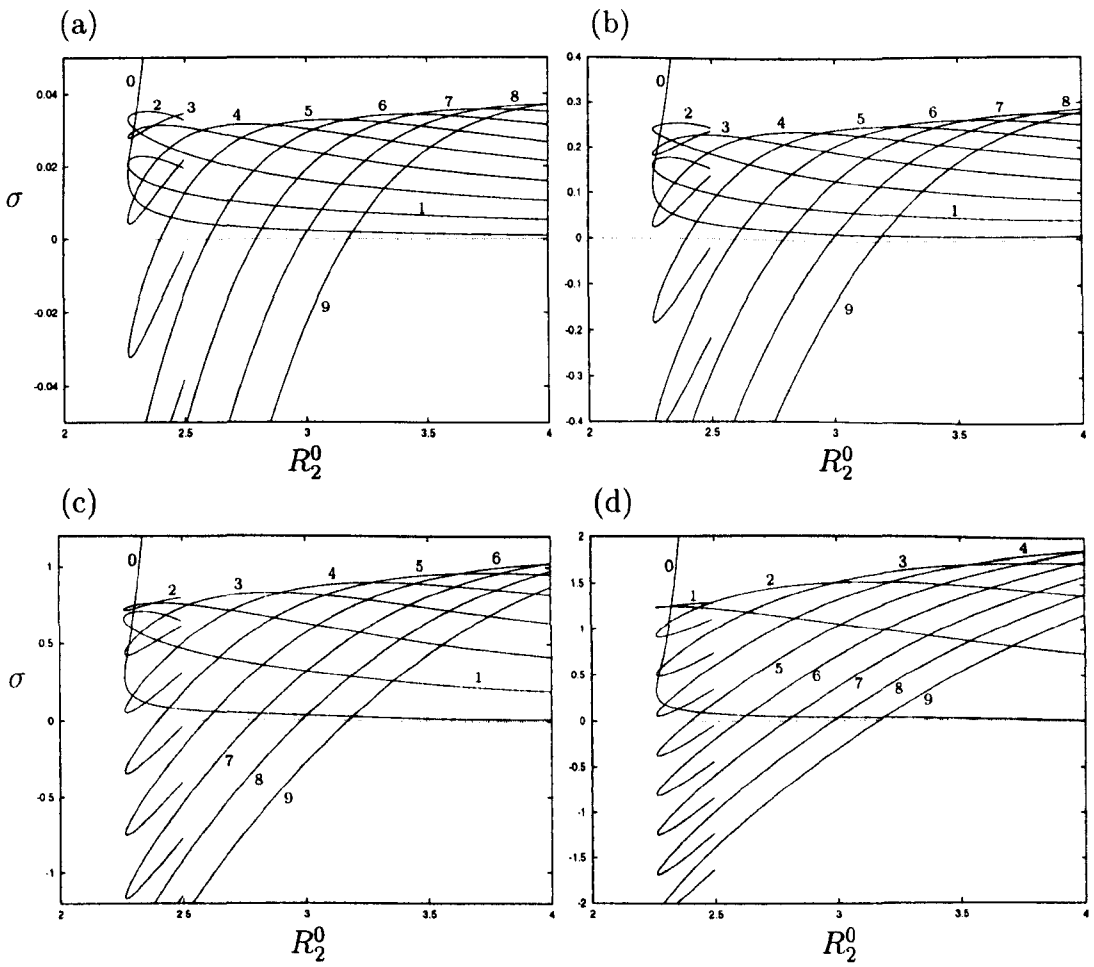

Figure 6.12: (a) – (d) Plot of the largest eigenvalue as a function of R_2^0 for an annular drop for $q = 0, 1, 2, \ldots, 9$ in the case $\phi_0 = 0.7$ for $C = 1$, 0.1, 0.01 and 0.001.

unstable mode jumps from $q = 0$ to $q = 2$ then to $q = 3$, $q = 4$ and so on. The same qualitative behaviour occurs for $C = 0.1$ and $C = 0.01$ (Figs. 6.12(b) and (c) respectively). For $C = 0.001$ (Fig. 6.12(d)) the most unstable mode corresponds to $q = 0$ for small values of R_1^0. As R_1^0 increases the most unstable mode jumps from $q = 0$ to $q = 1$ then to $q = 2$, $q = 3$ and so on.

Figures 6.13(a) - (d) plot the largest eigenvalue as a function of R_2^0 for $q = 0$, 1, 2,..., 9 in the case $\phi_0 = 1$ for $C = 1$, 0.1, 0.01 and 0.001 respectively. As in Fig. 6.12, the free ends of the curves at $R_2^0 = (16/J)^{1/3} \approx 2.52$ correspond to $R_1^0 = 0$ and as we move along each curve away from these ends the value of R_1^0 increases monotonically from zero. For $C = 1$ (Fig. 6.13(a)) the most unstable mode corresponds to $q = 0$ for small values of R_1^0. As R_1^0 increases the most unstable mode jumps from $q = 0$ to $q = 2$ then to $q = 3$, $q = 4$ and so on. The same qualitative behaviour occurs for $C = 0.1$ (Fig. 6.13(b)). For $C = 0.01$ and $C = 0.001$ (Figs. 6.13(c) and (d) respectively) the most unstable mode corresponds to $q = 0$ for small values of R_1^0. As R_1^0 increases the most unstable mode jumps from $q = 0$ to $q = 1$ then to $q = 2$, $q = 3$ and so on.

Figures 6.14(a) - (d) plot the largest eigenvalue as a function of R_2^0 for $q = 0$, 1, 2,..., 9 in the case $\phi_0 = 1.3$ for $C = 1$, 0.1, 0.01 and 0.001 respectively. In this case solutions lie in the range $0 < R_2^0 \leq (16/J)^{1/3} \approx 2.52$. As R_2^0 increases in this range, R_1^0 increases from zero to a maximum (less than the corresponding value of R_2^0) and then decreases back to zero. For $C = 1$ (Fig. 6.14(a)) the most unstable mode corresponds to $q = 2$ for small values of R_2^0. As R_2^0 increases the most unstable mode jumps from $q = 2$ to $q = 0$. For $C = 0.1$ (Fig. 6.14(b)) the most unstable mode jumps from $q = 1$ to $q = 2$ followed by $q = 0$ as R_2^0 increases from zero; however the point at which the most unstable mode corresponds to $q = 1$ is outwith the range of the plot. For $C = 0.01$ (Fig. 6.14(c)) the most unstable mode jumps from $q = 1$ to $q = 2$, then to $q = 1$ again followed by $q = 0$ as R_2^0 increases from zero. For $C = 0.001$ (Fig. 6.14(d)) the most unstable mode jumps from $q = 1$ for small values of R_2^0 to $q = 0$ as R_2^0 increases from zero.

In particular, Figs. 6.12 - 6.14 show how the numerically calculated values of σ approach σ_{q+} in the limit $C \to 0$.

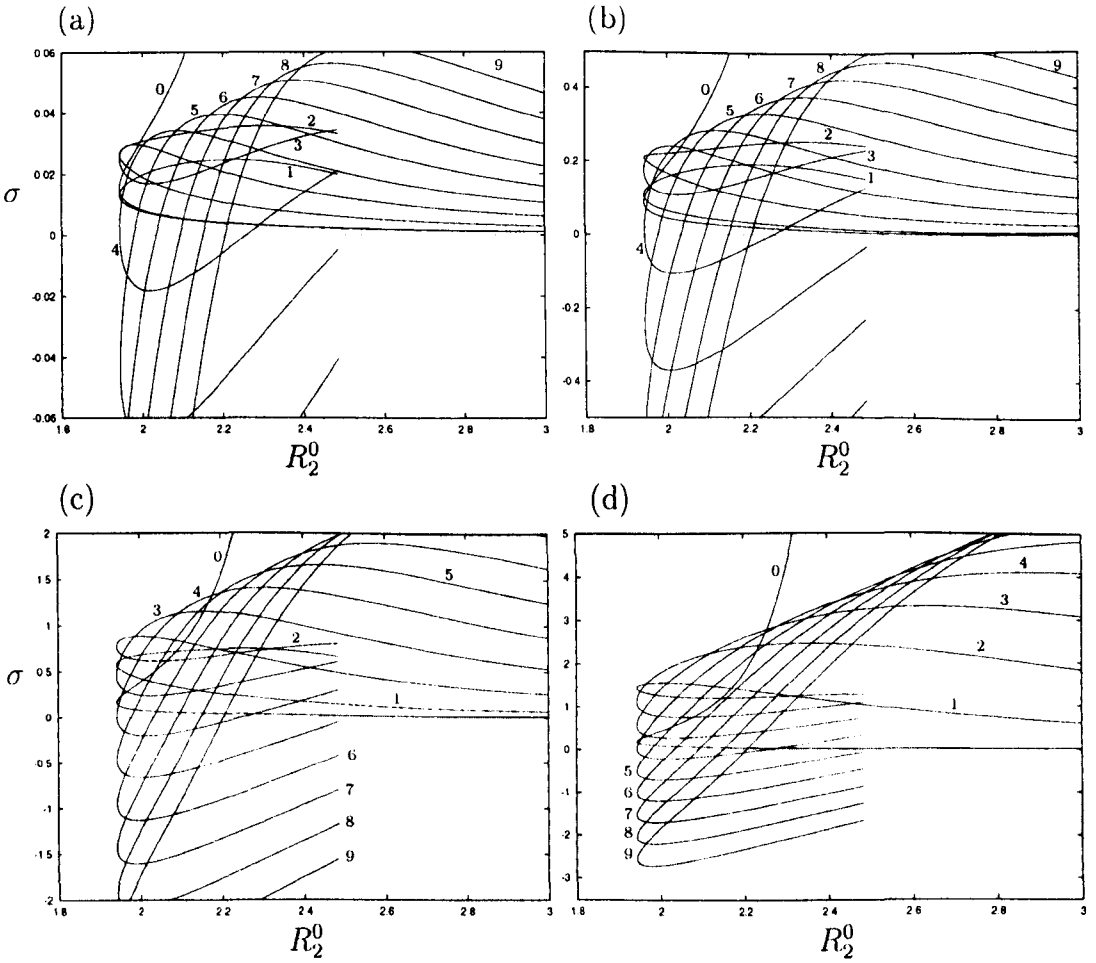

Figure 6.13: (a) – (d) Plot of the largest eigenvalue as a function of R_2^0 for an annular drop for $q = 0, 1, 2, \ldots, 9$ in the case $\phi_0 = 1$ for $C = 1$, 0.1, 0.01 and 0.001.

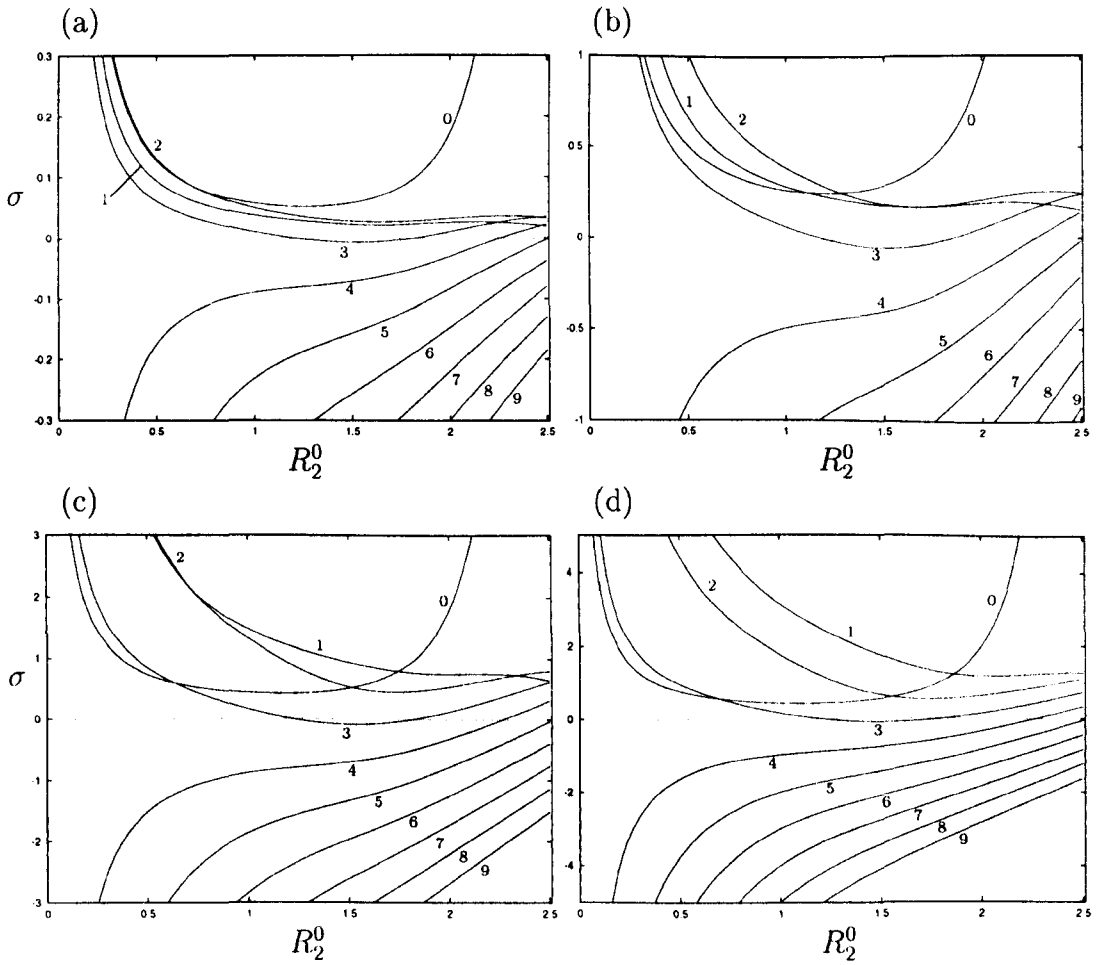

Figure 6.14: (a) (d) Plot of the largest eigenvalue as a function of R_2^0 for an annular drop for $q = 0, 1, 2, \ldots, 9$ in the case $\phi_0 = 1.3$ for $C = 1, 0.1, 0.01$ and 0.001.

These results are summarised in Figs. 6.15(a) - (d) which show the wavenumber of the most unstable mode corresponding to $\phi_0 = 0.7$, 1 and 1.3 for $C = 1$, 0.1, 0.01 and 0.001. The dots on Fig. 6.15 denote the values of R_1^0 and R_2^0 at which the most unstable mode jumps between two different values of q.

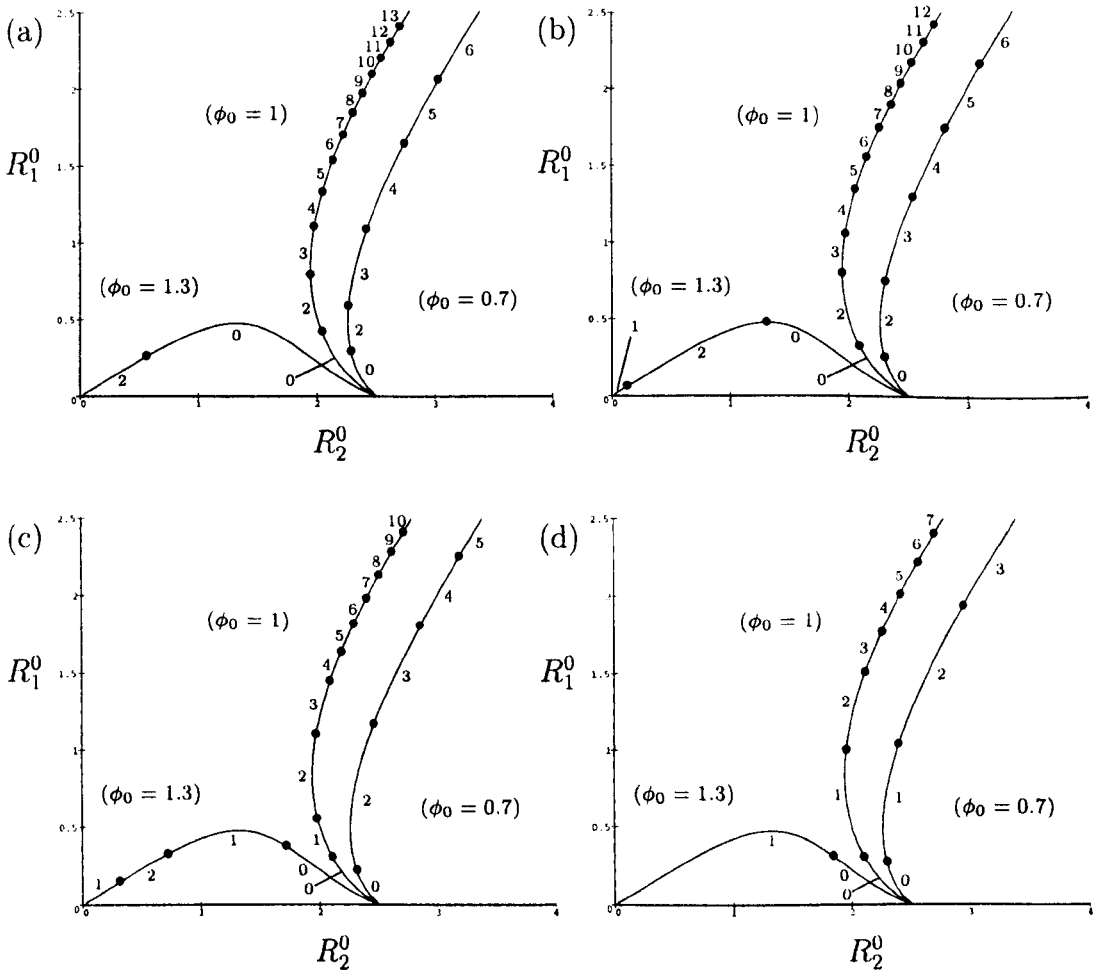

Figure 6.15: (a) – (d) Plot of R_1^0 against R_2^0 for annular solutions corresponding to $\phi_0 = 0.7$, 1 and 1.3 showing the most unstable wavenumber for $C = 1$, 0.1, 0.01 and 0.001. The dots correspond to the values of R_1^0 and R_2^0 at which the most unstable mode jumps between two different values of q.

Chapter 7

Conclusions and Further Work

7.1 Conclusions

Using the lubrication approximation to the Navier-Stokes equations we have investigated the evolution and stability of a thin film of incompressible Newtonian fluid on a planar substrate subjected to a jet of air blowing normally to the substrate. For the simple model of the air jet we adopted, the initially axisymmetric problems we studied are identical to those of a drop spreading on a turntable rotating at constant angular velocity (the simplest model for spin coating).

In Chapter 2 we investigated the quasi-static ($C = 0$) spreading of a finite-sized thin drop of incompressible, Newtonian fluid on a planar substrate in the presence of a jet of air in both symmetric two-dimensional and axisymmetric three-dimensional geometries. Three specific problems were studied in detail: a jet of air acting normally to the substrate when gravity effects are negligible, a jet of air directed vertically downwards onto a sessile drop on a horizontal substrate and a jet of air directed vertically upwards onto a pendent drop on a horizontal substrate. For each problem we determined the possible physically-realisable equilibrium solutions for the profile of the drop and investigated their stability to small perturbations with zero wavenumber. The evolution of the drop in the zero-gravity and pendent cases was also investigated. We found that for non-annular drops, the zero-gravity and sessile drop cases are qualitatively similar, and in both cases there is at most one stable and physical equilibrium solution.

Equilibrium solutions for drops with fixed volume V are possible only if the jet strength J is sufficiently small and equilibrium solutions for drops with fixed J are possible only if V is sufficiently small. Quasi-static evolutions were calculated numerically in the zero-gravity case and showed that the drop evolves to the stable equilibrium solution. In the case of a non-annular pendent drop there are finitely many (at least one and possibly more) stable and physical equilibrium solutions. Stable and physical equilibrium solutions for a drop with fixed V are possible only if J is sufficiently small, but stable and physical equilibrium solutions for a drop with fixed J are possible for all values of V. Quasi-static evolutions were calculated numerically and showed that a pendent drop evolves to a stable equilibrium solution that depends on the initial value of the drop radius.

In Chapter 3 we repeated the quasi-static ($C = 0$) analysis of Chapter 2 for annular drops with a dry patch at their centre. This analysis was restricted to the special case of zero gravity for simplicity. Unlike non-annular drops, it was found that planar and axisymmetric annular drops in zero gravity exhibit qualitatively different characteristics. In the planar case, it was shown that there are no equilibrium solutions when the inner contact angle is equal to or greater than the outer one, while in the axisymmetric case equilibrium solutions are possible for all values of the inner contact angle. As in the zero-gravity non-annular case, equilibrium annular solutions for fixed V are possible only for sufficiently small J, and for fixed J are possible only for sufficiently small V. However, in all the cases investigated it was shown that in both planar and axisymmetric geometries, all these annular solutions are unconditionally unstable. Quasi-static evolutions of an annular drop were calculated numerically and it was found in all the cases investigated that a drop with initial outer radius smaller than that of the equilibrium value closes, while a drop with initial outer radius larger than the equilibrium value opens, irrespective of the value of the initial inner radius.

In both Chapters 2 and 3 the stability analysis was restricted to uniform perturbations for the two-dimensional problems and to axisymmetric perturbations

for the three-dimensional problems in the case of zero capillary number, $C = 0$. In order to analyse the stability to general perturbations for $C \neq 0$, a numerical finite-difference code was developed in Chapter 4 capable of solving the linear differential eigenvalue problems arising from the linear stability analysis.

In Chapter 5 we investigated the linear stability to both uniform ($q = 0$) and non-uniform ($q \neq 0$) perturbations of an initially two-dimensional thin ridge of Newtonian fluid of finite width on a horizontal planar substrate acting under the influence of a jet of air normal to the substrate. Two problems were considered: one in which the jet acted at the centre of the ridge, and one in which the jet acted off-centre. For each problem we examined both the special case of quasi-static motion ($C = 0$) analytically and the general case of $C \neq 0$ numerically. In all cases the ridge was found to be unconditionally unstable, but the nature and location of the most unstable mode depend on the details of the specific problem considered.

For the case of a centred jet we found that for two-dimensional quasi-static motion the conditionally stable symmetric modes described in Chapter 2 are always more stable than the unconditionally unstable antisymmetric modes. For general quasi-static motion the ridge is always most unstable to a long-wavelength symmetric mode. When $C \neq 0$ the nature and location of the most unstable mode switch between long-wavelength and finite-wavelength symmetric and antisymmetric modes as R_0 is varied. The quasi-static results are recovered in the limit $C \to 0$.

A similar analysis was performed for the more general case of an off-centred jet, for which all the modes are asymmetric. For two-dimensional quasi-static motion we recovered the results of Chapter 3, while for general quasi-static motion the ridge is always unstable to a long-wavelength mode. When $C \neq 0$ the ridge is always most unstable to a mode with finite wavelength, and the switching between different types of modes and values of q found in the centred-jet case does not occur in this case. Again, the quasi-static results are recovered in the limit $C \to 0$.

In Chapter 6 we investigated the linear stability to both axisymmetric ($q = 0$)

and non-axisymmetric ($q \neq 0$) perturbations of an initially axisymmetric thin drop of Newtonian fluid either on a rotating substrate or under the influence of a jet of air directed normally towards a stationary substrate. Both non-annular and annular drops were considered. For each problem we examined both the special case of quasi-static motion ($C = 0$) analytically and the general case $C \neq 0$ numerically. In all cases the drop was found to be unconditionally unstable, but the growth rate and wavenumber of the most unstable mode depend on the details of the specific problem considered.

For the case of a non-annular drop we found that for axisymmetric quasi-static motion the conditionally unstable mode of Chapter 2 was recovered. For general quasi-static motion the drop is always unstable via the $q = 1$ mode. When $C \neq 0$ the drop is always unstable and the growth rate and wavenumber of the most unstable mode depend on the values of R_0 and C. In particular, the most unstable wavenumber increases as R_0 increases. The quasi-static results are recovered in the limit $C \to 0$.

A similar analysis was performed for the case of an annular drop. For axisymmetric quasi-static motion the unconditionally unstable results of Chapter 3 were recovered. For general quasi-static motion the drop is always unstable via either the $q = 0$ mode or the $q = 1$ mode depending on the values of R_1^0, R_2^0 and ϕ_0. When $C \neq 0$ the drop is always unstable and, like in the non-annular case, the growth rate and wavenumber of the most unstable mode depend on the values of R_1^0, R_2^0, ϕ_0 and C. For $\phi_0 \leq 1$ the most unstable wavenumber increases as R_1^0 increases, while for $\phi_0 > 1$ the most unstable wavenumber always corresponds to $q = 0$ for large enough R_2^0. Again, the quasi-static results are recovered in the limit $C \to 0$.

7.2 Further Work

The work described in this thesis could be extended in a number of ways.

In Chapters 2 and 3, evolution of non-annular and annular drops is restricted to axisymmetric geometries in the quasi-static limit of zero capillary number.

$C = 0$. The evolution of initially axisymmetric (and non-axisymmetric) non-annular and annular drops for general capillary number $C \neq 0$ would be an interesting extension. This work would also include the evolution of an initally uniform (and non-uniform) ridge for both a jet acting at the centre of the ridge and a jet acting off-centre for general capillary number. Calculating the evolution of these non-linear, differentio-algebraic systems is a demanding numerical task of the kind undertaken by López *et al.* [35] who considered the evolution of axisymmetric holes in a laterally-bounded thin fluid layer for general capillary number.

In Chapters 3, 5 and 6 the analysis is only for the special case of zero gravity, $G = 0$. Repeating the analysis for $G = 1$ (sessile case) and $G = i$ (pendent case) would be worthwhile extensions to the present work and, in principle, not hard to do. However, some preliminary numerical calculations and the results of Chapter 2 indicate that sessile and zero-gravity situations are qualitatively similar so perhaps the only new results would come from the pendent case.

The model for the jet of air that we adopted throughout was a simple parabolic pressure distribution in the air, however it would be of interest to examine the effect of using different models, including a Gaussian-type pressure distribution as used by Buchlin *et al.* [6], Kriegsmann *et al.* [29] and Tuck & Vanden-Broeck [56] and a piecewise-quadratic pressure distribution as used by Tuck [55] and Tuck & Vanden-Broeck [56]. Alternatively, using the approach of King *et al.* [28] and King & Tuck [27], the external pressure gradient could be found as part of the solution. Using thin aerofoil theory, the pressure is expressed in terms of the height of the free surface. This leads to a non-linear integro-differential equation for the height of the free surface which must, in general, be solved numerically.

Throughout this thesis we assumed for simplicity that the shear stress was zero at the free surface. A more realistic model would include a non-zero shear due to the jet of air. This is precisely how Ellen & Tu [11] extended the pioneering air-knife analysis of Thornton & Graff [52]. The analysis of Ellen & Tu [11] assumed a constant (but non-zero) shear stress at the free surface and showed

improved results when compared with experiment. Kataoka & Troian [25, 26] also assumed a constant (but non-zero) shear stress at the free surface in studying the stability of thermally-driven climbing films.

There are, as far as the author is aware, no experimental results for either spin coating or air-jet blowing which are directly relevant with the present work. A comparison between such experiments and the present theoretical results would be of considerable interest.

Finally, the numerical finite-difference code described in Chapter 4 could be used to investigate the stability of various other problems involving the dynamics of thin fluid films as well as problems of the type discussed in the final example of Chapter 4 (Sec. 4.3.5). Indeed, the code is capable of solving any general coupled linear differential eigenvalue problem and could therefore be used in other areas of applied mathematics in which such systems arise.

Bibliography

[1] D. J. Acheson, "The Navier-Stokes equations," Chapter 6 In *Elementary Fluid Dynamics* (Oxford University Press, 1994), pp. 201 – 220.

[2] A. Acrivos, M. J. Shah and E. E. Petersen, "On the flow of a non-Newtonian liquid on a rotating disk," J. Appl. Phys. **31**, 963 – 968 (1960).

[3] A. L. Bertozzi and M. P. Brenner, "Linear stability and transient growth in driven contact lines," Phys. Fluids **9**, 530 – 539 (1997).

[4] D. E. Bornside, C. W. Macosko and L. E. Scriven, "Spin coating : One-dimensional model," J. Appl. Phys. **66**, 5185 – 5193 (1989).

[5] R. J. Braun, B. T. Murray, W. J. Boettinger and G. B. McFadden, "Lubrication theory for reactive spreading of a thin drop," Phys. Fluids **7**, 1797 – 1810 (1995).

[6] J-M. Buchlin, M. Manna, M. Arnalsteen, M. L. Riethmuller and M. Dubois, "Theoretical and experimental investigation of gas-jet wiping," in *First European Coating Symposium on The Mechanics of Thin Film Coatings, Leeds University, UK, 19-22 September 1995*, edited by P. H. Gaskell, M. D. Savage, J. L. Summers, (World Scientific, Singapore, 1996), pp. 168 – 178.

[7] S. L. Burgess and S. D. R. Wilson, "Spin coating of a viscoplastic material," Phys. Fluids **8**, 2291 – 2297 (1996).

[8] B. R. Duffy and S. K. Wilson, "A third-order differential equation arising in thin-film flows and relevant to Tanner's Law," Appl. Math. Lett. **10**, 63 – 68 (1997).

[9] P. Ehrhard, "The spreading of hanging drops," J. Coll. Int. Sci. **168**, 242 – 246 (1994).

[10] P. Ehrhard and S. H. Davis, "Non-isothermal spreading of liquid drops on horizontal plates," J. Fluid Mech. **229**, 365 – 388 (1991).

[11] C. H. Ellen and C. V. Tu, "An analysis of jet stripping of liquid coatings," J. Fluids Eng. **106**, 399 – 404 (1984).

[12] A. G. Emslie, F. T. Bonner and L. G. Peck, "Flow of a viscous liquid on a rotating disk," J. Appl. Phys. **29**, 858 – 862 (1958).

[13] B. Fornberg, "Calculation of weights in finite difference formulas," SIAM Rev. **40**, 685 – 691 (1998).

[14] B. Fornberg and D. M. Sloan, "A review of pseudospectral methods," Acta Numerica, 203 – 267 (1994).

[15] N. Fraysse and G. M. Homsy, "An experimental study of rivulet instabilities in centrifugal spin coating of viscous Newtonian and non-Newtonian fluids," Phys. Fluids **6**, 1491 – 1504 (1994).

[16] H. P. Greenspan, "On the motion of a small viscous droplet that wets a surface," J. Fluid Mech. **84**, 125 – 143 (1978).

[17] B. G. Higgins, "Film flow on a rotating disk," Phys. Fluids **29**, 3522 – 3529 (1986).

[18] L. M. Hocking, "Sliding and spreading of thin two-dimensional drops," Q. Jl Mech. appl. Math. **34**, 37 – 55 (1981).

[19] L. M. Hocking, "The spreading of a thin drop by gravity and capillarity," Q. Jl Mech. appl. Math. **36**, 55 – 69 (1983).

[20] L. M. Hocking, "Spreading and instability of a viscous fluid sheet," J. Fluid Mech. **211**, 373 – 392 (1990).

[21] L. M. Hocking, "Rival contact-angle models and the spreading of drops," J. Fluid Mech. **239**, 671 – 681 (1992).

[22] L. M. Hocking, "The spreading of drops with intermolecular forces," Phys. Fluids **6**, 3224 – 3228 (1994).

[23] L. M. Hocking and M. J. Miksis, "Stability of a ridge of fluid," J. Fluid Mech. **247**, 157 – 177 (1993).

[24] S. A. Jenekhe and S. B. Schuldt, "Flow and film thickness of Bingham plastic liquids on a rotating disk," Chem. Eng. Commun. **33**, 135 – 147 (1985).

[25] D. E. Kataoka and S. M. Troian, "A theoretical study of instabilities at the advancing front of thermally driven coating films," J. Coll. Int. Sci. **192**, 350 – 362 (1997).

[26] D. E. Kataoka and S. M. Troian, "Stabilizing the advancing front of thermally driven climbing films," J. Coll. Int. Sci. **203**, 335 – 344 (1998).

[27] A. C. King and E. O. Tuck, "Thin liquid layers supported by steady air-flow surface traction," J. Fluid Mech. **251**, 709 – 718 (1993).

[28] A. C. King, E. O. Tuck and J. -M. Vanden-Broeck, "Air-blown waves on thin viscous sheets," Phys. Fluids A **5**, 973 – 978 (1993).

[29] J. J. Kriegsmann, M. J. Miksis and J. -M. Vanden-Broeck, "Pressure driven disturbances on a thin viscous film," Phys. Fluids **10**, 1249 – 1255 (1998).

[30] R. G. Larson and T. J. Rehg, "Spin coating," Chapter 14 In *Liquid film coating* edited by S. F. Kistler and P. M. Schweizer, (Chapman Hall, 1997), pp. 709 – 734.

[31] C. J. Lawrence, "The mechanics of spin coating of polymer films," Phys. Fluids **31**, 2786 – 2795 (1988).

[32] C. J. Lawrence and W. Zhou, "Spin coating of non-Newtonian fluids," J. Non-Newtonian Fluid Mech. **39**, 137 – 187 (1991).

[33] P. G. López, S. G. Bankoff and M. J. Miksis, "Non-isothermal spreading of a thin liquid film on an inclined plane," J. Fluid Mech. **324**, 261 – 286 (1996).

[34] P. G. López, M. J. Miksis and S. G. Bankoff, "Inertial effects on contact line instability in the coating of a dry inclined plate," Phys. Fluids **9**, 2177 – 2183 (1997).

[35] P. G. López, M. J. Miksis and S. G. Bankoff, "Stability and evolution of a dry spot," Northwestern University Applied Mathematics Technical Report 9605 (July 1997).

[36] I. S. McKinley and S. K. Wilson, "The linear stability of a ridge of fluid subject to a jet of air," submitted for publication.

[37] I. S. McKinley and S. K. Wilson, "The linear stability of a drop of fluid during spin coating or subject to a jet of air," submitted for publication.

[38] I. S. McKinley, S. K. Wilson and B. R. Duffy, "Spin coating and air-jet blowing of thin viscous drops," Phys. Fluids. **11**, 30 – 47 (1999).

[39] F. Melo, J. F. Joanny and S. Fauve, "Fingering instability of spinning drops," Phys. Rev. Lett. **63**, 1958 – 1961 (1989).

[40] D. Meyerhofer, "Characteristics of resist films produced by spinning," J. Appl. Phys. **49**, 3993 – 3997 (1978).

[41] E. Momoniat and D. P. Mason, "Investigation of the effect of the coriolis force on a thin fluid film on a rotating disk," Int. J. Non-Linear Mech. **33**, 1069 – 1088 (1998).

[42] J. A. Moriarty and L. W. Schwartz, "Dynamic considerations in the closing and opening of holes in thin liquid films," J. Coll. Int. Sci. **161**, 335 – 342 (1993).

[43] J. A. Moriarty, L. W. Schwartz and E. O. Tuck, "Unsteady spreading of thin liquid films with small surface tension," Phys. Fluids A **3**, 733 - 742 (1991).

[44] T. G. Myers, "Thin films with high surface tension," SIAM Rev. **40**, 441 - 462 (1998).

[45] A. Oron, S. H. Davis and S. G. Bankoff, "Long-scale evolution of thin liquid films," Rev. Mod. Phys. **69**, 931 - 980 (1997).

[46] B. Reisfeld, S. G. Bankoff and S. H. Davis, "The dynamics and stability of thin liquid films during spin coating 1. Films with constant rates of evaporation or absorption," J. Appl. Phys. **70**, 5258 - 5266 (1991).

[47] Y. D. Shikhmurzaev, "Moving contact lines in liquid/liquid/solid systems," J. Fluid Mech. **334**, 211 - 249 (1997).

[48] Y. D. Shikhmurzaev, "Spreading of drops on solid surfaces in a quasi-static regime, " Phys. Fluids **9**, 266 - 275 (1997).

[49] M. A. Spaid and G. M. Homsy, "Stability of Newtonian and viscoelastic dynamic contact lines," Phys. Fluids **8**, 460 - 478 (1996).

[50] M. A. Spaid and G. M. Homsy, "Stability of viscoelastic dynamic contact lines: an experimental study," Phys. Fluids **9**, 823 - 832 (1997).

[51] G. I. Taylor and D. H. Michael, "On making holes in a sheet of fluid," J. Fluid Mech. **58**, 625 - 639 (1973).

[52] J. A. Thornton and H. F. Graff, "An analytical description of the jet finishing process for hot-dip metallic coatings on strip." Metallurgical Trans. B **7B**, 607 - 618 (1976).

[53] S. M. Troian, E. Herbolzheimer, S. A. Safran and J. F. Joanny, "Fingering instabilities of driven spreading films," Europhys. Lett. **10**, 25 - 30 (1989).

[54] Y.-O. Tu, "Contact line slippage of fluid flow on a rotating disk," J. Coll. Int. Sci. **116**, 237 – 240 (1987).

[55] E. O. Tuck, "Continuous coating with gravity and jet stripping," Phys. Fluids **26**, 2352 – 2358 (1983).

[56] E. O. Tuck and J. -M. Vanden Broeck, "Influence of surface tension on jet-stripped continuous coating of sheet materials," A. I. Ch. E. Journal **30**, 808 – 811 (1984).

[57] M. Vinokur, "On one-dimensional stretching functions for finite-difference calculations," J. Comp. Phys. **50**, 215 – 234 (1983).

[58] J. H. Wilkinson, "Kronecker's canonical form and the QZ algorithm," Linear Algebra and Appl. **28**, 285 – 303 (1979).

[59] S. K. Wilson and B. R. Duffy, "An asymptotic analysis of small holes in thin fluid layers," J. Eng. Math. **30**, 445 – 457 (1996).

[60] S. K. Wilson and B. R. Duffy, "On the gravity-driven draining of a rivulet of viscous fluid down a slowly varying substrate with variation transverse to the direction of flow," Phys. Fluids **10**, 13 – 22 (1998).

[61] S. K. Wilson, R. Hunt and B. R. Duffy, "The rate of spreading in spin coating," submitted for publication.

[62] S. K. Wilson and E. L. Terrill, "The dynamics of planar and axisymmetric holes in thin fluid layers," in *First European Coating Symposium on the Mechanics of Thin Film Coatings, Leeds University, UK, 19-22 September 1995*, (eds. P. H. Gaskell, M. D. Savage and J. L. Summers), World Scientific, Singapore, 1996. pp. 288 – 297.

[63] M. Yanagisawa, "Slip effect for thin liquid film on a rotating disk," J. Appl. Phys. **61**, 1034 – 1037 (1987).